

11-02-02  
4009

# JOINT INSTITUTE FOR AERONAUTICS AND ACOUSTICS

136 P

National Aeronautics and  
Space Administration  
Ames Research Center

## JIAA TR - 112



Stanford University

## Numerical Study of the Trailing Vortex Of A Wing With Wing-Tip Blowing

N94-29760

Unclas

G3/02 0004059

By

### Hock-Bin Lim

Stanford University  
Department of Aeronautics and Astronautics  
Stanford, CA 94305

(NASA-CR-195803) NUMERICAL STUDY  
OF THE TRAILING VORTEX OF A WING  
WITH WING-TIP BLOWING (Stanford  
Univ.) 136 p

March 1994



**JIAA TR - 112**

**Numerical Study of the Trailing Vortex  
Of A Wing With Wing-Tip Blowing**

**By**

**Hock-Bin Lim**

**Stanford University  
Department of Aeronautics and Astronautics  
Stanford, CA 94305**

**March 1994**



# Abstract

Trailing vortices generated by lifting surfaces such as helicopter rotor blades, ship propellers, fixed wings, and canard control surfaces are known to be the source of noise, vibration, cavitation, degradation of performance, and other hazardous problems. Controlling these vortices is therefore of practical interest. The formation and behavior of the trailing vortices are studied in the present research. In addition, wing-tip blowing concepts employing axial blowing and spanwise blowing are studied to determine their effectiveness in controlling these vortices and their effects on the performance of the wing. The three-dimensional, unsteady, thin-layer compressible Navier-Stokes equations are solved using a time-accurate, implicit, finite difference scheme that employs LU-ADI factorization. The wing-tip blowing is simulated using the actuator plane concept, thereby not requiring resolution of the jet slot geometry. Furthermore, the solution blanking feature of the chimera scheme is used to simplify the parametric study procedure for the wing-tip blowing. Computed results are shown to compare favorably with experimental measurements. It is found that axial wing-tip blowing, although delaying the rolling-up of the trailing vortices and the near-field behavior of the flowfield, does not dissipate the circulation strength of the trailing vortex farther downstream. Spanwise wing-tip blowing



has the effect of displacing the trailing vortices outboard and upward. The increased “wing-span” due to the spanwise wing-tip blowing has the effect of lift augmentation on the wing and the strengthening of the trailing vortices. Secondary trailing vortices are created at high spanwise wing-tip blowing intensities.



# Contents

<b>Abstract</b>	<b>i</b>
<b>List of Figures</b>	<b>vii</b>
<b>List of Principal Symbols</b>	<b>xii</b>
<b>1 Introduction</b>	<b>1</b>
1.1 Motivation.....	1
1.2 Previous Work.....	3
1.2.1 Experimental and Theoretical Work .....	3
1.2.2 Computational Work.....	5
1.3 Current Approach.....	5
1.4 Thesis Outline.....	6
<b>2 Governing Equations and Numerical Method</b>	<b>14</b>
2.1 Governing Equations and Approximations.....	14
2.1.1 The Navier-Stokes Equations.....	14
2.1.2 Coordinate Transformation.....	17



2.1.3	Thin-Layer Approximation.....	20
2.2	Numerical Algorithm.....	22
2.2.1	Beam-Warming Algorithm.....	23
2.2.2	The Diagonally Dominant Factorization.....	25
2.2.3	The LU-ADI Algorithm.....	27
2.3	Turbulence Model.....	29
2.3.1	The Baldwin-Lomax Model.....	30
2.3.2	Turbulence Model for Wall Jet.....	32
2.4	Artificial Dissipation.....	33
<b>3</b>	<b>Grid Generation</b>	<b>35</b>
3.1	General Remarks.....	35
3.2	Elliptic Grid Generation.....	37
3.2.1	Thompson, Thames, and Mastin Method.....	37
3.2.2	Middlecoff-Thomas Algorithm.....	38
3.3	Grid Details.....	41
3.3.1	Geometry of Wing.....	41
3.3.2	Two-Dimensional Grid.....	41
3.3.3	Three-Dimensional Grid.....	44
<b>4</b>	<b>Boundary Conditions</b>	<b>51</b>
4.1	General Remarks.....	51
4.2	Boundary Conditions.....	52
4.3	Wing-Tip Blowing.....	53



4.3.1	Actuator Plane Concept .....	54
4.3.2	Solution Blanking Feature of Chimera Scheme.....	55
<b>5</b>	<b>Results and Discussion</b>	<b>58</b>
5.1	General Remarks .....	58
5.2	No Blowing Cases .....	58
5.2.1	Configuration.....	58
5.2.2	General Flow Features.....	59
5.2.3	Pressure Distribution.....	60
5.2.4	Forces and Moment.....	63
5.2.5	Vortex Strength.....	64
5.3	Axial Wing-Tip Blowing Cases.....	66
5.3.1	Configuration.....	66
5.3.2	General Flow Features.....	67
5.3.3	Vortex Strength.....	68
5.3.4	Forces and Moment.....	69
5.4	Spanwise Wing-Tip Blowing Cases .....	70
5.4.1	Configuration.....	70
5.4.2	General Flow Features.....	71
5.4.3	Forces and Moments.....	71
5.4.4	Vortex Strength.....	73
5.5	Solution Accuracy.....	74
<b>6</b>	<b>Conclusions and Recommendations</b>	<b>109</b>



6.1	Conclusions .....	109
6.2	Recommendations.....	110
	<b>Bibliography</b>	<b>112</b>



# List of Figures

1.1	Trailing vortices of a conventional fixed-wing aircraft (taken from Kuethe and Chow [1986]). .....	7
1.2	Hazardous effects on smaller aircraft flying into the wakes of larger aircraft (taken from Gessow [1976]). .....	8
1.3	Schematic sketch of the wake structure for a single rotor blade in hover (taken from Stepniewski and Keys [1984])......	9
1.4	Blade-vortex interaction of a helicopter during forward and/or descending flights (taken from White [1973])......	10
1.5	Progression of cavitation around propeller blades (taken from Trevena [1987])......	11
1.6	Lanchester's drawing of the vortex roll-up (taken from Hackett and Evans [1971])......	12
1.7	Wing-tip configurations for controlling trailing vortices (taken from White [1973])......	13
3.1	Geometry of the semi-span wing having a NACA 0015 symmetric airfoil section, with no twist, no taper, no sweep, and a rounded wing-tip.....	47
3.2	Two-dimensional grid at the wing center-plane showing the C-grid topology. Fine clustering of grid points at the leading edge, the	



	trailing edge, aft of the trailing edge, and close to the wing surface.....	48
3.3	A y-z plane view (looking upstream) of the three-dimensional grid showing the rounded wing-tip of the wing and the fine clustering of grid points around the wing-tip to capture the wing-tip vortex.....	49
3.4	A cut-away isometric view of the wing and the three-dimensional computational grid.....	50
4.1	A schematic sketch of the actuator plane concept (taken from Craig [1993]).....	57
5.1	Particle traces showing the formation and roll-up of the wing-tip vortex.....	75
5.2	Side and plan views of the trailing vortex.....	76
5.3	Velocity vectors at the quarter-chord showing flow from the lower surface to the upper surface of the wing near the wing-tip. ....	77
5.4	Distribution of the pressure coefficients, $C_p$ , on the wing near the wing-tip region for the case of $\alpha = 4^\circ$ , $M_\infty = 0.17$ and $Re = 2.0 \times 10^6$ .....	78
5.5	Distribution of the pressure coefficients, $C_p$ , on the wing near the wing-tip region for the case of $\alpha = 8^\circ$ , $M_\infty = 0.17$ and $Re = 2.0 \times 10^6$ .....	79
5.6	Distribution of the pressure coefficients, $C_p$ , on the wing near the wing-tip region for the case of $\alpha = 12^\circ$ , $M_\infty = 0.17$ and $Re = 2.0 \times 10^6$ .....	80
5.7	Formation of the tip vortex at $x/c = 0.9$ depicted by the stagnation pressure coefficient contours.....	81



5.8	Velocity vectors showing the highly three-dimensional nature of the tip vortex.....	82
5.9	$C_p$ distributions for the inboard 60% of the wing span showing the two-dimensional nature of the flow at the inboard region.....	83
5.10	Stagnation pressure coefficient contours across the trailing vortex for various axial stations downstream of the trailing edge.....	84
5.11	Variations of the coefficients of lift, drag and pitching moment (about the quarter-chord) for the case of $M_\infty = 0.17$ and $Re = 2.0 \times 10^6$ .....	85
5.12	Streamwise distribution of the normalized total circulation for the case of $\alpha = 12^\circ$ , $M_\infty = 0.17$ and $Re = 2.0 \times 10^6$ .....	86
5.13	Comparison of the calculated normalized downwash distribution downstream of the trailing edge with the theoretical analysis of Spreiter-Sacks for the case of $\alpha = 12^\circ$ , $M_\infty = 0.17$ and $Re = 2.0 \times 10^6$ .....	87
5.14	The jet slot with a jet length of 11.2% chord and a jet width of 1.5% chord is located at the 90%-chord location for the axial wing-tip blowing.....	88
5.15	Velocity vectors at the spanwise station $2y/b = 0.9693$ (zoom-in)...	89
5.16	Velocity vectors at the spanwise station $2y/b = 0.9693$ .....	90
5.17	Variation of the streamwise distribution of the normalized total circulation with blowing momentum coefficient for the case of $\alpha = 8^\circ$ , $M_\infty = 0.17$ and $Re = 2.0 \times 10^6$ .....	91
5.18	Particle traces showing the rolling-up of the trailing vortex with axial wing-tip blowing off and on.....	92



5.19	Downwash distribution at various axial stations downstream of the trailing edge for the case of $\alpha = 8^\circ$ , $M_\infty = 0.17$ , $Re = 2.0 \times 10^6$ and with blowing off.....	93
5.20	Downwash distribution at various axial stations downstream of the trailing edge for the case of $\alpha = 8^\circ$ , $M_\infty = 0.17$ , $Re = 2.0 \times 10^6$ and with axial wing-tip blowing on ( $C_\mu = 0.0047$ ).....	94
5.21	Variations of the coefficients of lift, drag and pitching moment (about the quarter-chord) with blowing momentum coefficient for the case of $\alpha = 8^\circ$ , $M_\infty = 0.17$ and $Re = 2.0 \times 10^6$ .....	95
5.22	Pressure contours at $x/c = 0.95$ near the wing-tip region for cases with axial wing-tip blowing off and on.....	96
5.23	Wind-tunnel model used in the experimental studies with spanwise wing-tip blowing (taken from Tavella et al [1988]).....	97
5.24	Close-up views of the velocity vectors at $x/c = 1.1$ for the case of $\alpha = 8^\circ$ with spanwise wing-tip blowing turned off and on.....	98
5.25	Velocity vectors at $x/c = 0.9$ for the case of $\alpha = 2^\circ$ with increasing spanwise wing-tip blowing intensity.....	99
5.26	Variations of the coefficients of lift, drag, pitching moment (about the wing quarter-chord) and $L/D$ with blowing momentum coefficient for $\alpha = 2^\circ$ , $4^\circ$ , $6^\circ$ and $8^\circ$ .....	101
5.27	Variation of the coefficient of lift with angle-of-attack without spanwise wing-tip blowing.....	103
5.28	Variation of the streamwise distribution of the normalized total circulation with blowing momentum coefficient for the case of $\alpha = 4^\circ$ .....	104



5.29	Stagnation pressure contours showing the streamwise development of the primary and secondary vortices for the case $\alpha = 2^\circ$ and $C_\mu = 0.2067$ .....	105
5.30	Comparison of the computational results using coarse and fine grids with the experimental data for the case of $\alpha = 12^\circ$ .....	108



# List of Principal Symbols

$a$	speed of sound
$a_\infty$	freestream speed of sound
$A$	flux Jacobian matrix in the $\xi$ -direction
$A_{jet}$	jet slot area
$AR$	aspect ratio of the (full-span) wing
$b$	wing span; distance normal to surface where $V = V_{max}/2$ in a wall jet
$B$	flux Jacobian matrix in the $\eta$ -direction
$c$	wing chord
$c_p$	specific heat at constant pressure
$C$	flux Jacobian matrix in the $\zeta$ -direction
$C_L, C_D, C_M$	coefficients of lift, drag, and pitching moment (about the quarter-chord) of wing
$C_p$	pressure coefficient
$C_\mu$	blowing momentum coefficient
$D_E, D_I$	explicit and implicit artificial dissipation terms, respectively
$D_A, D_B, D_c$	diagonal matrices associated with the LU-ADI algorithm
$e$	total energy per unit volume
$e_i$	internal energy per unit mass
$E$	inviscid flux vector in the $x$ -direction
$\hat{E}$	inviscid flux vector in the $\xi$ -direction



$E_v$	viscous flux vector in the $x$ -direction
$\hat{E}_v$	viscous flux vector in the $\xi$ -direction
$F$	inviscid flux vector in the $y$ -direction
$\hat{F}$	inviscid flux vector in the $\eta$ -direction
$F_v$	viscous flux vector in the $y$ -direction
$\hat{F}_v$	viscous flux vector in the $\eta$ -direction
$G$	inviscid flux vector in the $z$ -direction
$\hat{G}$	inviscid flux vector in the $\zeta$ -direction
$G_v$	viscous flux vector in the $z$ -direction
$\hat{G}_v$	viscous flux vector in the $\zeta$ -direction
$h$	time step size
$I$	identity matrix
$J$	transformation Jacobian
$k$	coefficient of thermal conductivity; constant for wall jet turbulence model
$K$	constant for wall jet turbulence model
$K_E, K_I$	user-specified input constants for explicit and implicit artificial dissipation
$l$	turbulent mixing length scale
$L_A, L_B, L_C$	lower bidiagonal matrices associated with the LU-ADI algorithm
$M$	viscous flux Jacobian matrix in the $\zeta$ -direction
$M_\infty$	freestream Mach number
$n$	normal direction coordinate
$p$	pressure
$p_{plenum}$	total jet plenum pressure
$P$	source term of the Poisson equations defined to provide elliptic grid control
$Pr$	Prandtl number



$q_\infty$	freestream dynamic pressure
$Q$	vector of conservative flow variables in Cartesian coordinates; source term of the Poisson equations defined to provide elliptic grid control
$\hat{Q}$	vector of conservative flow variables in transformed coordinates
$R$	radius of curvature; gas constant
$Re$	Reynolds number
$\hat{S}$	viscous flux vector with the thin-layer approximation
$S_{ref}$	wing reference area
$t$	time
$T$	temperature
$T_\xi, T_\eta, T_\zeta$	similarity transformation matrices
$u, v, w$	Cartesian velocity components
$U_A, U_B, U_C$	upper bidiagonal matrices associated with the LU-ADI algorithm
$U, V, W$	contravariant velocity components
$V$	velocity
$V_{jet}$	jet exit velocity
$V_{max}$	maximum magnitude of velocity in wall jet
$x, y, z$	Cartesian coordinates
$\alpha$	angle of attack; geometric stretching factor
$\beta_x, \beta_y, \beta_z$	heat flux vector components
$\gamma$	ratio of specific heats
$\Gamma$	total circulation strength
$\delta_\xi, \delta_\eta, \delta_\zeta$	central difference operators
$\Delta_\xi, \Delta_\eta, \Delta_\zeta$	forward difference operators
$\nabla_\xi, \nabla_\eta, \nabla_\zeta$	backward difference operators
$\varepsilon$	freestream velocity correction factor
$\varepsilon_E, \varepsilon_I$	explicit and implicit artificial dissipation coefficients, respectively



$\lambda$	coefficient of bulk viscosity
$\Lambda_A, \Lambda_B, \Lambda_C$	diagonal matrices of eigenvalues associated with the flux Jacobian matrices $A, B,$ and $C,$ respectively
$\mu$	coefficient of viscosity
$\mu_\infty$	freestream coefficient of viscosity
$\xi, \eta, \zeta$	chordwise, spanwise and normal coordinates in body-conforming system
$\rho$	density
$\rho_{jet}$	jet exit density
$\rho_\infty$	freestream density
$\sigma$	spectral radius of flux Jacobian matrix
$\tau$	time coordinate in computational domain
$\tau_{ij}$	shear stress tensor, $i, j = x, y$ or $z$
$\phi$	Middlecoff-Thomas grid control function
$\Phi$	matrix of flux limiters for artificial dissipation model
$\psi$	Middlecoff-Thomas grid control function
$\omega$	vorticity



# Chapter 1

## Introduction

### 1.1 Motivation

Near the tip of a lifting surface, the pressure differential between the upper and lower surfaces causes the fluid to move around the tip from the higher pressure lower surface towards the lower pressure upper surface. As the fluid undergoes this highly 3-dimensional maneuver at the tip, it realigns the bound vortex (caused by the boundary layer vorticity of the lifting surface) which is parallel to the span of the lifting surface into the downstream direction. This tip vortex is convected downstream and is typically called the trailing vortex.

Trailing vortices of a conventional fixed-wing aircraft are depicted in Figure 1.1. The vortices generated by larger fixed-wing aircraft may cause undesirable and sometimes uncontrollable rolling moment and other hazardous effects on smaller aircraft flying into their wakes. (See Figure 1.2.) These trailing vortices may persist for a considerable distance; and result in a rather long safety distance (thus long interval) required between flights. The problem can be severe especially during take-off and landing at a busy airport. Trailing

vortices from the canards of many modern fighter aircraft can also pose problems on the wings of the aircraft resulting in the degradation of performance.

For helicopter rotor blades, trailing vortices are convected downward in a helical manner (see Figure 1.3) due to the downwash and the rotational motion of the lifting surfaces. Vortices shed from the preceding blades of a helicopter may interact with the following blades (called blade-vortex interaction; see Figure 1.4) during forward and descending flights. This is a major source of noise and vibration for helicopters (see, for example, Schmitz and Yu [1983]). Ship propellers have a very similar problem encountered by helicopter rotor blades. In addition, erosion on propeller blades may occur as the propeller blades strike the low pressure air pockets (called cavitation) created by the trailing vortices (see Figure 1.5).

It is therefore of practical interest to explore the effects of control devices such as axial and spanwise wing-tip blowing on the formation and behavior of tip vortices and on the performance of the wing. Spanwise blowing has been studied also as a means of control to effect a change of vortex position on one wing-tip and thereby produce a rolling moment through asymmetric wing lift (see Tavella et al [1988]).

For several reasons, then, it is desirable to better understand computationally the origin of the tip vortex and the wing it is influenced by blowing - i.e. whether it can be displaced to produce a rolling moment and whether its behavior downstream can be affected to reduce noise and reduce the hazard to following aircraft.

## 1.2 Previous Work

### 1.2.1 Experimental and Theoretical Work

The phenomenon of the trailing vortex from a lifting surface was recognized as early as 1907 by Lanchester [1907] (see Figure 1.6). Some subsequent landmark works include Westwater's calculation of the vortex roll-up and trajectory using the two-dimensional (Trefftz plane) model of a vortex sheet consisting of point, doubly infinite, vortex elements (see Westwater [1935]). Betz [1932] analyzed the movement of the center of gravity of the trailing vortices in the two-dimensional cross-plane. Spreiter and Sacks [1951] studied the inviscid effects of lifting surface parameters such as aspect ratio, lift coefficient and wing chord on the downwash by solving the Laplace equation.

By correlating with experimental data, McCormick et al [1968], Roberts [1975, 1984], Phillips [1981] proposed analytical scaling laws to describe the structure of viscous turbulent trailing vortices with some success. Various experimental studies involving scaled model testing using wind-tunnels and full-scale flight testing were also carried out especially in the 1970s (see, for example, Olsen et al [1971], and Hallock and Eberle [1977]). A more recent and comprehensive experimental study was performed by McAlister and Takahashi [1991].

Concurrently, efforts were being made to minimize the effects of trailing vortices. Most of the efforts employed various wing-tip configurations to spread, relocate, and dissipate the trailing vortices (see Figure 1.7). For example, the configuration with gulled outer panels in Figure 1.7 serves to

divide the total concentrated vorticity into two vortices, each of lesser strength, at two different spanwise locations, (one at the juncture of the gulled tip and main lifting surface and the other at the tip), and also to relocate the tip vortex with respect to a dimension normal to the wing chord plane because of the deflection of the tip of the gulled section (see White [1973]). The configuration with a drag spoiler fixed at the wing-tip is known to increase the aircraft drag (see Corsiglia et al [1971]). These fixed configurations, although they may be optimized for a particular flight condition, suffer degradation in performance for other flight conditions. On the other hand, configurations employing active control devices such as wing-tip blowing allow adjustments to be made as the flight condition changes by changing the blowing intensity. The emphasis of the present research effort is on these active control configurations employing wing-tip blowing.

Some experimental investigations had been carried out to study the effects of axial wing-tip blowing (or mass injection) on the behavior of trailing vortices at low Reynolds number (see, for example, Snedeker [1971], Mason and Marchman [1973], White [1973], and Dunham [1976]). However, it was not conclusive whether this concept of employing axial wing-tip blowing was effective since conflicting observations were reported.

The concept of employing spanwise wing-tip blowing had also been carried out experimentally (see, for example, Ayers and Wilde [1956], Wu et al [1984], Tavella et al [1985], and Lee et al [1989]). It was observed that lift augmentation could be achieved via spanwise wing-tip blowing.

Olsen et al [1971], Hallock and Eberle [1977], and Hallock [1992] provide more details on various research efforts on the trailing vortex problem.

## 1.2.2 Computational Work

A preliminary study on the tip vortex from a low aspect ratio wing was studied by Mansour [1985] using the Computational Fluid Dynamics (CFD) methodology. Srinivasan et al [1988] extended the study to include the effects of wing planform shape and the wing-tip shape on the structure of the trailing vortices. Strawn [1991] applied the unstructured adaptive-grid scheme to study the structure of inviscid trailing vortices by solving the Euler equations. Dacles-Mariani et al [1993] incorporated the experimental data of Chow et al [1993] into the computations to study the near-field structure of the turbulent wing-tip vortex. Childs [1986] did a preliminary study on the lift augmentation due to the spanwise wing-tip blowing. Wong and Kandil [1992] studied the effects of angled wing-tip blowing on the behavior of trailing vortices.

## 1.3 Current Approach

Despite the fact that a tremendous amount of work has been done on the trailing vortex problem, this complex flow phenomenon is still not very well understood, especially when active control devices such as wing-tip blowing are employed.

The present study attempts to apply the CFD methodology to better understand the formation and behavior of trailing vortices and to evaluate the effects of axial and spanwise wing-tip blowing on these vortices for both fixed-wing and rotary-wing aircraft applications. However, no numerical

computations are performed for the rotorcraft configuration because of the enormous amount of computational effort required (see Srinivasan et al [1992]). A geometrically simple and computationally cheaper fixed-wing configuration is used instead. This is motivated by the findings of Tung et al [1983], who had investigated the structure of trailing vortices generated by model rotor blades and observed that the structure of the trailing vortices generated by rotor blades was very similar to that generated by fixed-wing aircraft, and Spivey [1968], who observed that the centrifugal effect due to the rotating rotor blade had very little impact on the path of the trailing vortices.

## 1.4 Thesis Outline

This thesis is divided into six chapters. Following the introduction in this chapter, Chapter 2 describes the equations governing the present research problem, the approximations introduced, the turbulence models used, the numerical algorithm and the artificial dissipation applied to solve these equations. Chapter 3 covers the grid generation method and grid topology used. Chapter 4 discusses the implementation of the boundary conditions required by the Navier-Stokes equations for cases with and without wing-tip blowing. Chapter 5 presents the computed results for the unblown cases, the axial and spanwise blowing cases and compares them with the available experimental data and theoretical analyses. The final chapter, Chapter 6, concludes the findings of this research and outlines possible improvements and future work.

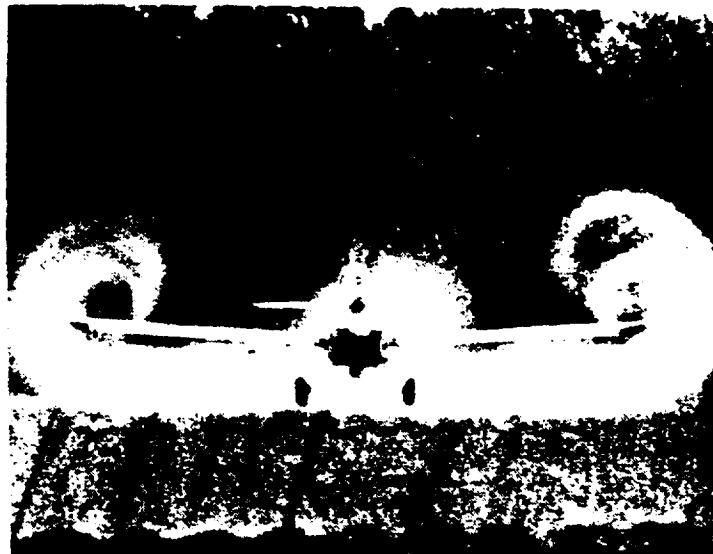
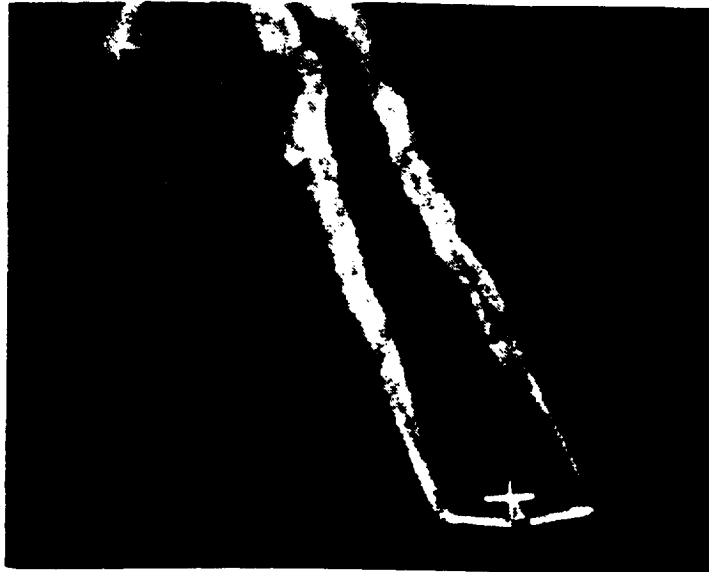


Figure 1.1: Trailing vortices of a conventional fixed-wing aircraft (taken from Kuethe and Chow [1986]).

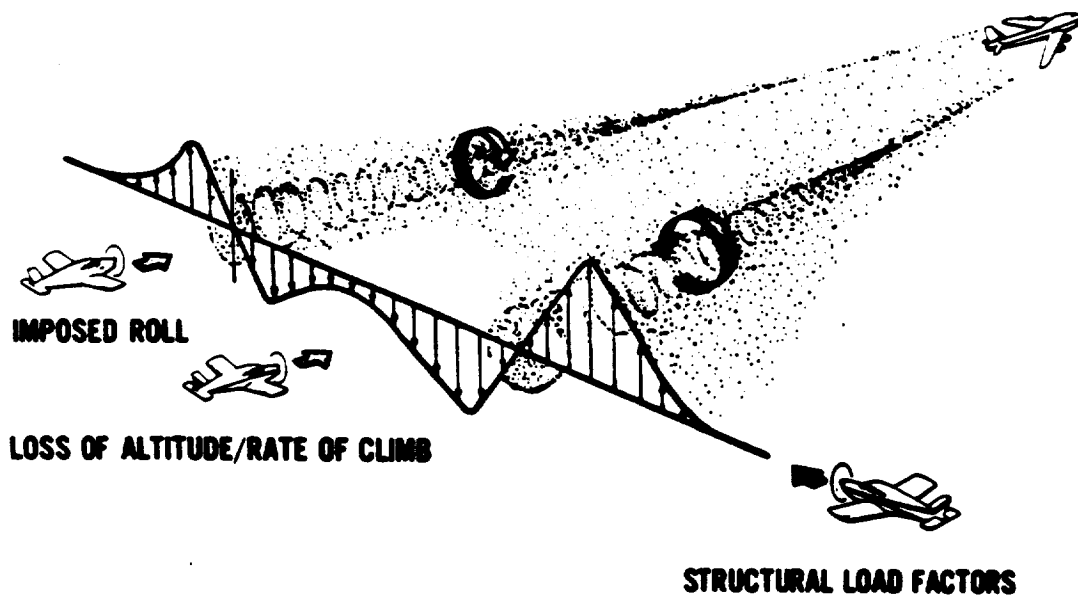


Figure 1.2: Hazardous effects on smaller aircraft flying into the wakes of larger aircraft (taken from Gessow [1976]).

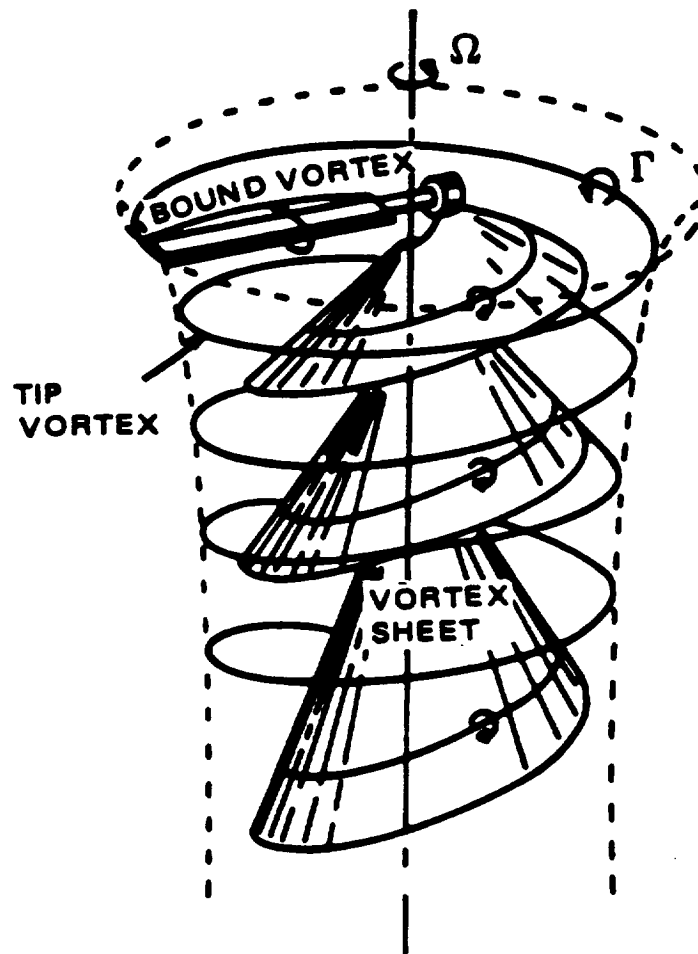


Figure 1.3: Schematic sketch of the wake structure for a single rotor blade in hover (taken from Stepniewski and Keys [1984]).

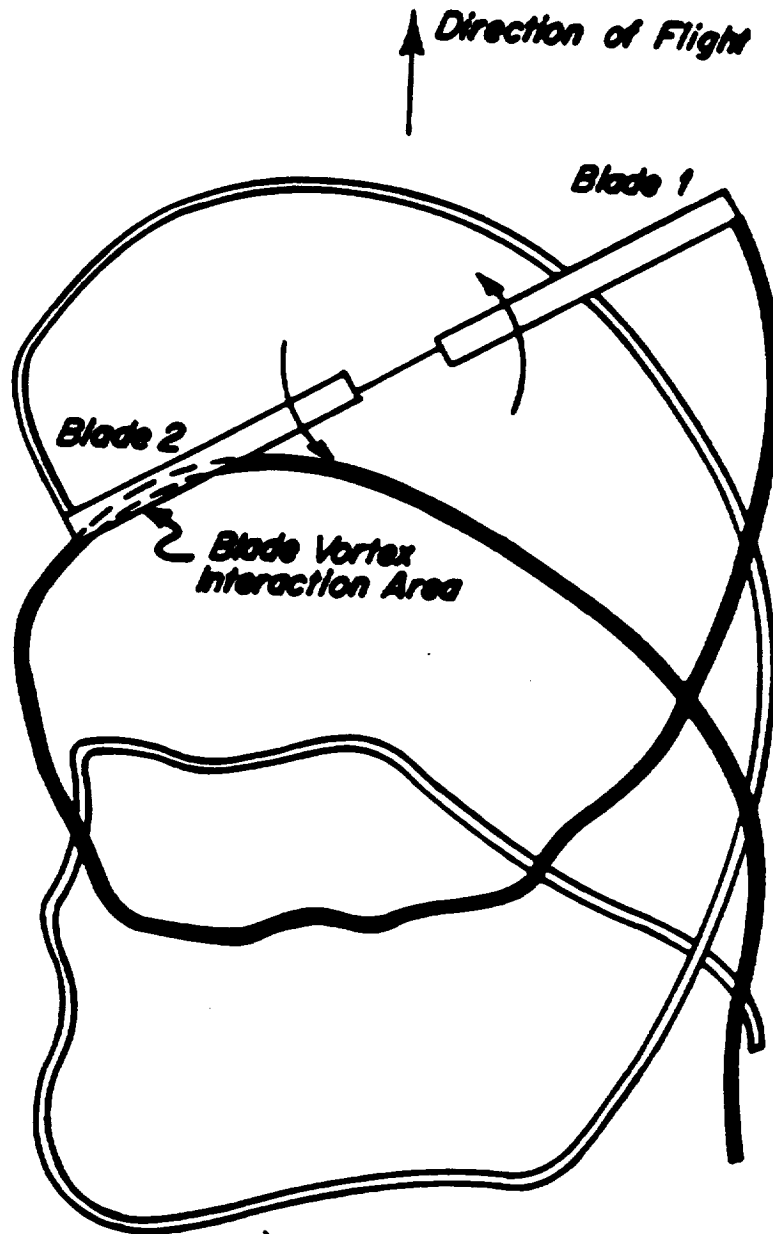


Figure 1.4: Blade-vortex interaction of a helicopter during forward and/or descending flights (taken from White [1973]).



Figure 1.5: Progression of cavitation around propeller blades (taken from Trevena [1987]).

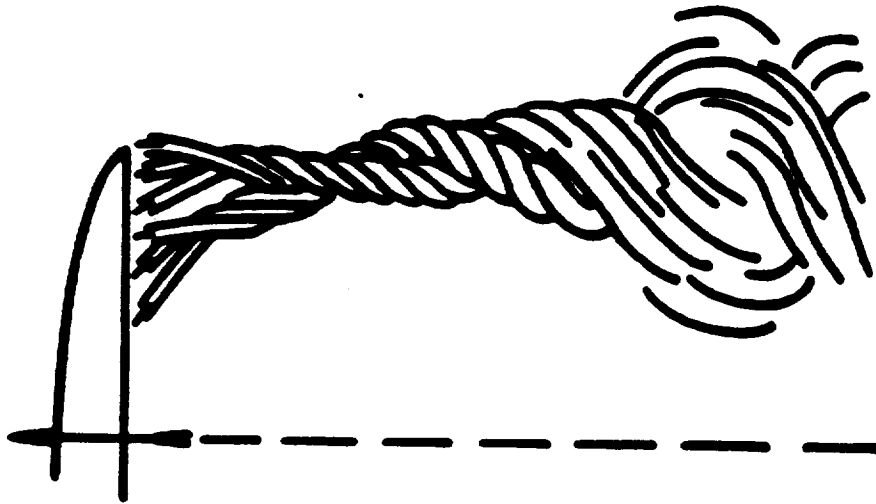


Figure 1.6: Lanchester's drawing of the vortex roll-up (taken from Hackett and Evans [1971]).

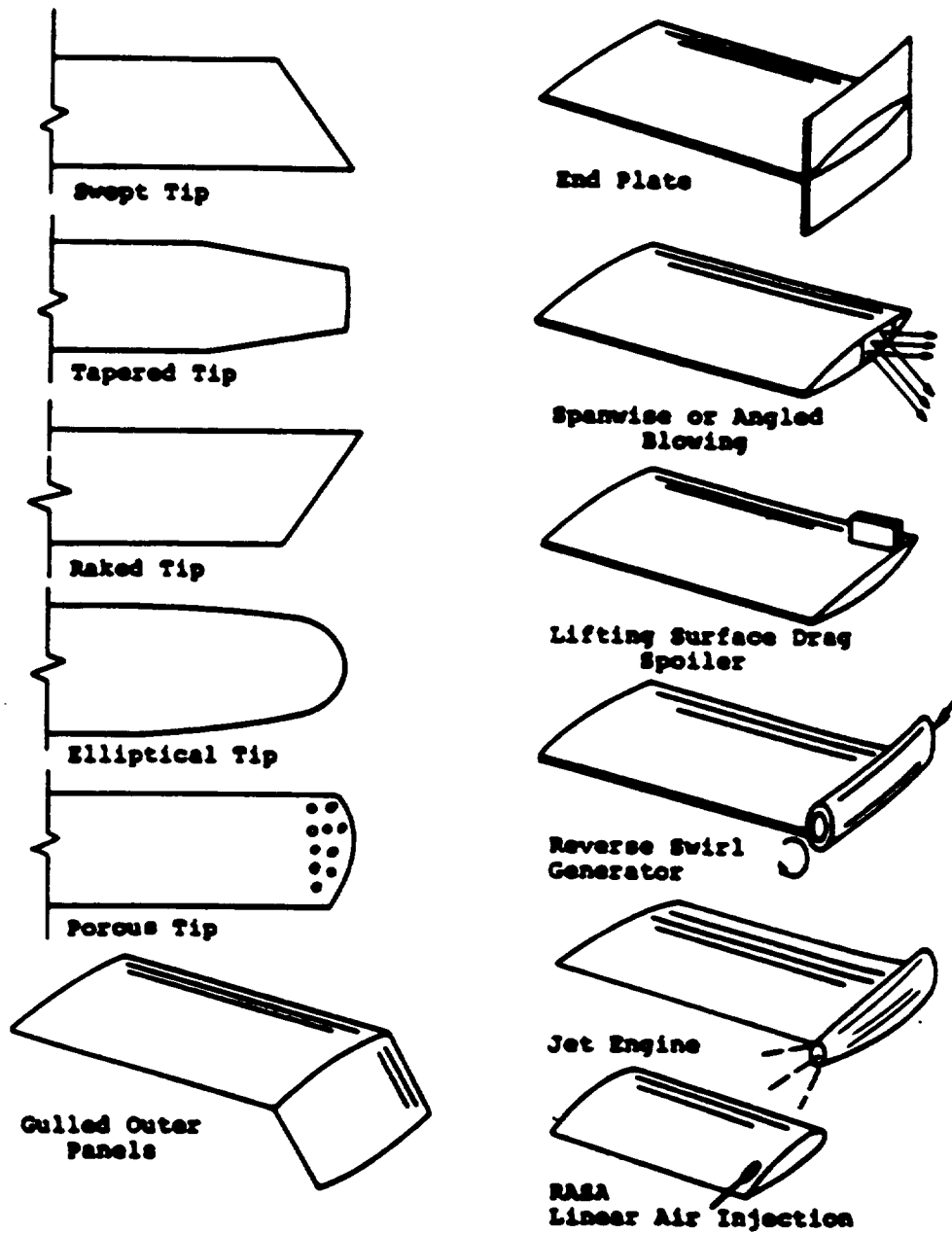


Figure 1.7: Wing-tip configurations for controlling trailing vortices (taken from White [1973]).



# Chapter 2

## Governing Equations and Numerical Method

### 2.1 Governing Equations and Approximations

#### 2.1.1 The Navier-Stokes Equations

The governing equations used in the present trailing vortex study are the three-dimensional Navier-Stokes equations. Under the assumptions of no body forces and no external heat addition, the Navier-Stokes equations can be written in conservation-law form in nondimensional Cartesian coordinates as follows (see, for example, Peyret and Viviand [1975]):

$$\frac{\partial Q}{\partial t} + \frac{\partial E}{\partial x} + \frac{\partial F}{\partial y} + \frac{\partial G}{\partial z} = \frac{\partial E_v}{\partial x} + \frac{\partial F_v}{\partial y} + \frac{\partial G_v}{\partial z} \quad (2.1)$$

where the conservative flow variables vector  $Q$  is defined as

$$Q = \begin{bmatrix} \rho \\ \rho u \\ \rho v \\ \rho w \\ e \end{bmatrix} \quad (2.2)$$

The inviscid or ‘‘Euler’’ flux vectors  $E, F, G$  are given by

$$E = \begin{bmatrix} \rho u \\ \rho u^2 + p \\ \rho uv \\ \rho uw \\ u(e+p) \end{bmatrix}, \quad F = \begin{bmatrix} \rho v \\ \rho v^2 + p \\ \rho vw \\ \rho vw \\ v(e+p) \end{bmatrix}, \quad G = \begin{bmatrix} \rho w \\ \rho w^2 + p \\ \rho vw \\ \rho vw \\ w(e+p) \end{bmatrix} \quad (2.3)$$

and the viscous flux vectors  $E_v, F_v, G_v$  are given by

$$E_v = Re^{-1} \begin{bmatrix} 0 \\ \tau_{xx} \\ \tau_{yx} \\ \tau_{zx} \\ \beta_x \end{bmatrix}, \quad F_v = Re^{-1} \begin{bmatrix} 0 \\ \tau_{xy} \\ \tau_{yy} \\ \tau_{zy} \\ \beta_y \end{bmatrix}, \quad G_v = Re^{-1} \begin{bmatrix} 0 \\ \tau_{xz} \\ \tau_{yz} \\ \tau_{zz} \\ \beta_z \end{bmatrix} \quad (2.4)$$

The components of the viscous stresses are

$$\begin{aligned} \tau_{xx} &= \lambda(u_x + v_y + w_z) + 2\mu u_x \\ \tau_{yy} &= \lambda(u_x + v_y + w_z) + 2\mu v_y \\ \tau_{zz} &= \lambda(u_x + v_y + w_z) + 2\mu w_z \\ \tau_{xy} &= \tau_{yx} = \mu(u_y + v_x) \\ \tau_{xz} &= \tau_{zx} = \mu(u_z + w_x) \\ \tau_{yz} &= \tau_{zy} = \mu(v_z + w_y) \end{aligned} \quad \begin{aligned} \beta_x &= \frac{\gamma\mu}{Pr} \partial_x e_i + u\tau_{xx} + v\tau_{xy} + w\tau_{xz} \\ \beta_y &= \frac{\gamma\mu}{Pr} \partial_y e_i + u\tau_{yx} + v\tau_{yy} + w\tau_{yz} \\ \beta_z &= \frac{\gamma\mu}{Pr} \partial_z e_i + u\tau_{zx} + v\tau_{zy} + w\tau_{zz} \end{aligned} \quad (2.5)$$

where  $u_x = \partial u / \partial x$ ,  $v_y = \partial v / \partial y$ ,  $\partial_x e_i = \partial e_i / \partial x$ , etc.

The density  $\rho$  is nondimensionalized by the freestream density  $\rho_\infty$ , the velocity components  $u$ ,  $v$  and  $w$  by the freestream speed of sound  $a_\infty$ , and the total energy per unit volume  $e$  by  $\rho_\infty a_\infty^2$ . Conforming to the usual convention,  $u$  is in the wing chord ( $x$ ) direction (positive aft),  $v$  is in the wing spanwise ( $y$ ) direction (positive outboard), and  $w$  is in the vertical ( $z$ ) direction (positive upwards). The coefficient of viscosity  $\mu$  is normalized by its freestream value,  $\mu_\infty$ , and the time is normalized by  $c / a_\infty$  where  $c$  is the wing chord. The Reynolds number is defined as  $Re = \rho_\infty a_\infty c / \mu_\infty$ . The Prandtl number  $Pr$  is defined as  $Pr = c_p \mu / k$  where  $c_p$  is the specific heat at constant pressure and  $k$  is the coefficient of thermal conductivity. Also,  $\gamma$  is the ratio of specific heats which for air is equal to 1.4.

The internal energy per unit mass  $e_i$  is related to the total energy  $e$  as follows:

$$e_i = \frac{e}{\rho} - \frac{(u^2 + v^2 + w^2)}{2} \quad (2.6)$$

Pressure is related to the conservative flow variables through the equation of state for a perfect gas

$$p = (\gamma - 1) \left[ e - \frac{\rho}{2} (u^2 + v^2 + w^2) \right] \quad (2.7)$$

The fluid in the present study is also considered to be Newtonian (i.e., viscous stresses are linearly related to the rates of strain), isotropic (i.e., having no preferred direction), and that Stokes' hypothesis, which states that the bulk

viscosity ( $\lambda + \frac{2}{3}\mu$ ) is zero, is satisfied. These assumptions are found to be valid for aerodynamic applications.

### 2.1.2 Coordinate Transformation

Next, the Navier-Stokes equations are transformed from the Cartesian coordinates  $(x, y, z, t)$  to a generalized, body-fitted, curvilinear coordinate system  $(\xi, \eta, \zeta, \tau)$ . This makes the formulation independent of the body geometry thereby easing the specification of the boundary conditions. The transformation from the physical domain to the computational domain also allows standard differencing schemes for equi-spaced grid points to be used for spatial derivatives. In addition, it also allows the thin-layer approximation (to be discussed in Section 2.1.3) to be applied in a straight-forward manner. The coordinate transformation is defined by:

$$\begin{aligned}\xi &= \xi(x, y, z, t) \\ \eta &= \eta(x, y, z, t) \\ \zeta &= \zeta(x, y, z, t) \\ \tau &= t\end{aligned}\tag{2.8}$$

where  $t$  and  $\tau$  are independent variables of time in the physical and transformed coordinates, respectively. The airfoil surface in the chordwise direction is transformed to the  $\xi$ -coordinate, the spanwise direction is transformed to the  $\eta$ -coordinate and the  $\zeta$ -coordinate is normal to the wing surface. Chain rule is applied in the transformation procedure which can be found in Viviand [1974] and Vinokur [1974]. The resulting transformation Jacobian is

$$J = 1 / \det \begin{vmatrix} x_\xi & x_\eta & x_\zeta \\ y_\xi & y_\eta & y_\zeta \\ z_\xi & z_\eta & z_\zeta \end{vmatrix} \quad (2.9)$$

where  $x_\xi = \partial x / \partial \xi$ ,  $x_\eta = \partial x / \partial \eta$ , etc, and the transformation metrics are given by

$$\begin{aligned} \xi_x &= J (y_\eta z_\zeta - y_\zeta z_\eta) & \eta_x &= J (y_\zeta z_\xi - y_\xi z_\zeta) \\ \xi_y &= J (x_\zeta z_\eta - x_\eta z_\zeta) & \eta_y &= J (x_\xi z_\zeta - x_\zeta z_\xi) \\ \xi_z &= J (x_\eta y_\zeta - x_\zeta y_\eta) & \eta_z &= J (x_\zeta y_\xi - x_\xi y_\zeta) \end{aligned} \quad (2.10)$$

$$\begin{aligned} \zeta_x &= J (y_\xi z_\eta - y_\eta z_\xi) & \xi_t &= -x_\tau \xi_x - y_\tau \xi_y - z_\tau \xi_z \\ \zeta_y &= J (x_\eta z_\xi - x_\xi z_\eta) & \eta_t &= -x_\tau \eta_x - y_\tau \eta_y - z_\tau \eta_z \\ \zeta_z &= J (x_\xi y_\eta - x_\eta y_\xi) & \zeta_t &= -x_\tau \zeta_x - y_\tau \zeta_y - z_\tau \zeta_z \end{aligned} \quad (2.11)$$

For the present study, stationary grids (i.e., no body motion) are considered and the metric time derivative terms are zero. The transformation Jacobian and metrics have their geometric interpretations: the transformation Jacobian is the inverse of the local grid cell volume, and the metrics are grid cell area projections. They give good indication on the grid quality, for example, whether the grid is stretched too rapidly.

The transformed Navier-Stokes equations can be written in strong conservation-law form (see, for example, Anderson et al [1984]) in a generalized coordinate system  $(\xi, \eta, \zeta, \tau)$  as follows:

$$\frac{\partial \hat{Q}}{\partial \tau} + \frac{\partial \hat{E}}{\partial \xi} + \frac{\partial \hat{F}}{\partial \eta} + \frac{\partial \hat{G}}{\partial \zeta} = \frac{1}{Re} \left[ \frac{\partial \hat{E}_v}{\partial \xi} + \frac{\partial \hat{F}_v}{\partial \eta} + \frac{\partial \hat{G}_v}{\partial \zeta} \right] \quad (2.12)$$

where the symbol “^” indicates transformed variables. The transformed, conservative flow variables vector and the inviscid flux vectors are

$$\hat{Q} = J^{-1} \begin{bmatrix} \rho \\ \rho u \\ \rho v \\ \rho w \\ e \end{bmatrix}, \quad \hat{E} = J^{-1} \begin{bmatrix} \rho U \\ \rho u U + \xi_x p \\ \rho v U + \xi_y p \\ \rho w U + \xi_z p \\ (e + p)U - \xi_i p \end{bmatrix} \quad (2.13)$$

$$\hat{F} = J^{-1} \begin{bmatrix} \rho V \\ \rho u V + \eta_x p \\ \rho v V + \eta_y p \\ \rho w V + \eta_z p \\ (e + p)V - \eta_i p \end{bmatrix}, \quad \hat{G} = J^{-1} \begin{bmatrix} \rho W \\ \rho u W + \zeta_x p \\ \rho v W + \zeta_y p \\ \rho w W + \zeta_z p \\ (e + p)W - \zeta_i p \end{bmatrix} \quad (2.14)$$

where the variables  $U$ ,  $V$  and  $W$  are the contravariant velocity components. The contravariant velocity  $U$  is the component of velocity parallel to the wing surface and in the direction of the wing chord,  $V$  is the component of velocity in the spanwise direction, and  $W$  is normal to the wing surface. They are related to the velocity components,  $u$ ,  $v$ , and  $w$ , as follows:

$$\begin{aligned} U &= \xi_t + \xi_x u + \xi_y v + \xi_z w \\ V &= \eta_t + \eta_x u + \eta_y v + \eta_z w \\ W &= \zeta_t + \zeta_x u + \zeta_y v + \zeta_z w \end{aligned} \quad (2.15)$$

The transformed viscous flux vectors are

$$\hat{E}_v = J^{-1} \begin{bmatrix} 0 \\ \xi_x \tau_{xx} + \xi_y \tau_{xy} + \xi_z \tau_{xz} \\ \xi_x \tau_{yx} + \xi_y \tau_{yy} + \xi_z \tau_{yz} \\ \xi_x \tau_{zx} + \xi_y \tau_{zy} + \xi_z \tau_{zz} \\ \xi_x \beta_x + \xi_y \beta_y + \xi_z \beta_z \end{bmatrix} \quad (2.16)$$

$$\hat{F}_v = J^{-1} \begin{bmatrix} 0 \\ \eta_x \tau_{xx} + \eta_y \tau_{xy} + \eta_z \tau_{xz} \\ \eta_x \tau_{yx} + \eta_y \tau_{yy} + \eta_z \tau_{yz} \\ \eta_x \tau_{zx} + \eta_y \tau_{zy} + \eta_z \tau_{zz} \\ \eta_x \beta_x + \eta_y \beta_y + \eta_z \beta_z \end{bmatrix} \quad (2.17)$$

$$\hat{G}_v = J^{-1} \begin{bmatrix} 0 \\ \zeta_x \tau_{xx} + \zeta_y \tau_{xy} + \zeta_z \tau_{xz} \\ \zeta_x \tau_{yx} + \zeta_y \tau_{yy} + \zeta_z \tau_{yz} \\ \zeta_x \tau_{zx} + \zeta_y \tau_{zy} + \zeta_z \tau_{zz} \\ \zeta_x \beta_x + \zeta_y \beta_y + \zeta_z \beta_z \end{bmatrix} \quad (2.18)$$

### 2.1.3 Thin-Layer Approximation

Most aerodynamic applications of practical interest, including the trailing vortex problem, involve high Reynolds number flows. For the high Reynolds number flows, the viscous effects are confined to the thin shear layers near the body surface, in the wake and in the trailing vortex core. Due to the limitations in computer memory and computational time it is necessary to concentrate the available grid points in these thin shear layers. To resolve the corresponding derivative components in the viscous terms, fine clustering of grid points has to be made across these thin shear layers. This results in grid spacing that is fine, normal and near to the surface, and that is relatively coarse, tangential to the

surface. With this type of grid, even if the full Navier-Stokes equations were solved, the viscous terms possessing velocity gradients tangential to the body would not be resolved because of insufficient grid density along the surface. For most cases of interest (i.e. high  $Re$  flows), however, these terms are negligible anyway. Therefore, it is justifiable to eliminate from the calculation the viscous fluxes associated with the directions parallel to the surface, i.e., the  $\xi$ - and  $\eta$ -directions. This approximation is easily applied since the equations are already transformed into the body-fitted computational domain.

The thin-layer approximation is motivated by the success of the boundary layer theory. All the assumptions, except one, made in the boundary layer theory are adopted in the thin-layer approximation. In the boundary layer theory, pressure is assumed to be constant across the boundary layer. However, the thin-layer approximation is less restrictive: it retains the normal momentum equation and allows pressure variation across the boundary layer.

Applying the thin-layer approximation (i.e., retaining only the  $\partial/\partial\zeta$  terms and eliminating all the  $\partial/\partial\xi$  and  $\partial/\partial\eta$  terms in the viscous stress components) then, the non-dimensional, three-dimensional, unsteady Navier-Stokes equations in conservation-law form in transformed, body-fitted, curvilinear coordinates become:

$$\frac{\partial \hat{Q}}{\partial \tau} + \frac{\partial \hat{E}}{\partial \xi} + \frac{\partial \hat{F}}{\partial \eta} + \frac{\partial \hat{G}}{\partial \zeta} = \frac{1}{Re} \frac{\partial \hat{S}}{\partial \zeta} \quad (2.19)$$

where

$$\hat{S} = J^{-1} \begin{bmatrix} 0 \\ \mu m_1 u_\zeta + (\mu/3) m_2 \zeta_x \\ \mu m_1 v_\zeta + (\mu/3) m_2 \zeta_y \\ \mu m_1 w_\zeta + (\mu/3) m_2 \zeta_z \\ \mu m_1 m_3 + (\mu/3) m_2 (\eta_x u + \eta_y v + \eta_z w) \end{bmatrix} \quad (2.20)$$

with

$$\begin{aligned} m_1 &= \zeta_x^2 + \zeta_y^2 + \zeta_z^2 \\ m_2 &= \zeta_x u_\zeta + \zeta_y v_\zeta + \zeta_z w_\zeta \\ m_3 &= \frac{1}{2} (u^2 + v^2 + w^2)_\zeta + \frac{\kappa}{Pr(\gamma-1)} (a^2)_\zeta \end{aligned} \quad (2.21)$$

## 2.2 Numerical Algorithm

An implicit, noniterative, time-accurate, finite difference scheme developed by Fujii and Obayashi [1986a, 1986b] is used to solve the three-dimensional compressible thin-layer Navier-Stokes equations. The scheme, which is first-order accurate in time and second-order accurate in space, employs the LU-ADI factorization. The basic structure of the algorithm is based on the Beam-Warming algorithm (see Beam and Warming [1976, 1978]) and incorporates the Steger-Warming flux vector splitting technique (see Steger and Warming [1981]) and diagonally dominant factorization (see Pulliam and Chaussee [1981] and Pulliam and Steger [1985]). The development of the algorithm is outlined below.

### 2.2.1 Beam and Warming Algorithm

The Beam and Warming algorithm (see Beam and Warming [1976, 1978]) employs an implicit, approximately-factored, non-iterative technique. Implicit methods are preferred over explicit methods especially in obtaining the steady-state solution. A large time step can be used in implicit methods to reach the steady-state solution rapidly; whereas explicit methods suffer the disadvantage of having a severe restriction on time step size in order to maintain stability.

A first-order accurate implicit time integration scheme is selected to march the solution of the unsteady Navier-Stokes equations in time. Second- and higher-order time accurate schemes are not used since they require the storage of the solution from previous time levels and result in a significant increase in the computer memory requirements. Discretizing Equation (2.19), using the first-order accurate backward Euler time integration scheme gives

$$\hat{Q}^{n+1} - \hat{Q}^n + h \left[ \frac{\partial \hat{E}^{n+1}}{\partial \xi} + \frac{\partial \hat{F}^{n+1}}{\partial \eta} + \frac{\partial \hat{G}^{n+1}}{\partial \zeta} - \frac{1}{Re} \frac{\partial \hat{S}^{n+1}}{\partial \zeta} \right] = 0 \quad (2.22)$$

where  $h$  is the time step,  $n + 1$  is the time level at which  $\hat{Q}$  is desired,  $n$  is the previous time level at which  $\hat{Q}$  is known everywhere, and  $\hat{Q}^n = \hat{Q}(nh)$ .

To have a non-iterative solution method, the flux vectors are linearized as follows:

$$\begin{aligned}
\hat{E}^{n+1} &= \hat{E}^n + A^n \Delta \hat{Q}^n + O(h^2) \\
\hat{F}^{n+1} &= \hat{F}^n + B^n \Delta \hat{Q}^n + O(h^2) \\
\hat{G}^{n+1} &= \hat{G}^n + C^n \Delta \hat{Q}^n + O(h^2) \\
\hat{S}^{n+1} &= \hat{S}^n + M^n \Delta \hat{Q}^n + O(h^2)
\end{aligned} \tag{2.23}$$

where  $\Delta \hat{Q}^n = \hat{Q}^{n+1} - \hat{Q}^n$  and the flux Jacobian matrices  $A^n$ ,  $B^n$ ,  $C^n$  and  $M^n$  are given by:

$$A^n = \frac{\partial \hat{E}}{\partial \hat{Q}}, \quad B^n = \frac{\partial \hat{F}}{\partial \hat{Q}}, \quad C^n = \frac{\partial \hat{G}}{\partial \hat{Q}}, \quad M^n = \frac{\partial \hat{S}}{\partial \hat{Q}} \tag{2.24}$$

These flux Jacobian matrices are derived analytically in Pulliam and Steger [1980].

The alternating direction implicit (ADI) algorithm was used by Beam and Warming [1976, 1978] to replace the inversion of one huge matrix (which would be prohibitively expensive to compute) with the inversions of three block tridiagonal matrices, one for each direction, using a block tridiagonal solver. By applying the ADI algorithm, Equation (2.22) can be written in the ‘‘delta form’’ as follows:

$$\begin{aligned}
& \left[ I + i_b h \delta_\xi A^n - i_b D_I|_\xi \right] \left[ I + i_b h \delta_\eta B^n - i_b D_I|_\eta \right] \\
& \left[ I + i_b h \delta_\zeta C^n - i_b h R e^{-1} \delta_\zeta J^{-1} M^n J - i_b D_I|_\zeta \right] \Delta \hat{Q}^n \\
& = -i_b h \left[ \delta_\xi \hat{E}^n + \delta_\eta \hat{F}^n + \delta_\zeta \hat{G}^n - R e^{-1} \delta_\zeta \hat{S}^n \right] - i_b \left[ D_E|_\xi + D_E|_\eta + D_E|_\zeta \right] \hat{Q}^n
\end{aligned} \tag{2.25}$$

where  $I$  is the identity matrix.  $D_I$  and  $D_E$  are, respectively, the implicit and explicit artificial dissipation terms required for numerical stability. The ‘‘delta

form" is normally used for solving steady-state problems since the final solutions do not depend on the choice of implicit operators once steady state is reached (i.e.,  $\Delta\hat{Q}^n \rightarrow 0$ ).

Notice that the solution blanking feature of the chimera scheme (see Benek et al [1985]) is incorporated into Equation (2.25) by including an integer  $i_b$  which is assigned a value of zero or one at every grid point. If  $i_b = 0$ ,  $\Delta\hat{Q}^n$  becomes zero and the solution remains unchanged at this grid point. If  $i_b = 1$ , the grid point is not blanked and is solved as part of the implicit solution. The usefulness of this blanking feature in modeling wing-tip blowing is discussed in Chapter 4. Fejtek and Roberts [1992] employed this feature for tilt-rotor computations.

### 2.2.2 The Diagonally Dominant Factorization

By applying the diagonally dominant factorization proposed by Pulliam and Chaussee [1981], the block tridiagonal matrices can be transformed into scalar tridiagonal matrices which are much cheaper computationally to invert. Recognizing that the flux Jacobian matrices  $A$ ,  $B$  and  $C$  each has real eigenvalues and a complete set of eigenvectors, they can be diagonalized by similarity transformations as follows:

$$\Lambda_A = T_\xi^{-1} A T_\xi, \quad \Lambda_B = T_\eta^{-1} B T_\eta, \quad \Lambda_C = T_\zeta^{-1} C T_\zeta \quad (2.26)$$

where  $\Lambda_A$ ,  $\Lambda_B$  and  $\Lambda_C$  are diagonal matrices containing the eigenvalues of matrices  $A$ ,  $B$  and  $C$ , respectively. The elements of the diagonal matrices are the characteristic speeds of the flow. For example,

$$\Lambda_A = \begin{bmatrix} U & 0 & 0 & 0 & 0 \\ 0 & U & 0 & 0 & 0 \\ 0 & 0 & U & 0 & 0 \\ 0 & 0 & 0 & U + a\sqrt{\xi_x^2 + \xi_y^2 + \xi_z^2} & 0 \\ 0 & 0 & 0 & 0 & U - a\sqrt{\xi_x^2 + \xi_y^2 + \xi_z^2} \end{bmatrix} \quad (2.27)$$

Analytical expressions for the similarity transformation matrices  $T_\xi$ ,  $T_\eta$  and  $T_\zeta$ , their inverse matrices, and the other diagonal matrices can be found in Pulliam and Chaussee [1981].

In the  $\xi$ -direction, for example, the Beam-Warming ADI operator can be written in the diagonal form as

$$\begin{aligned} \left[ I + i_b h \delta_\xi A - i_b D_I \Big|_\xi \right] &= T_\xi T_\xi^{-1} + i_b h \delta_\xi \left( T_\xi \Lambda_A T_\xi^{-1} \right) - i_b T_\xi D_I \Big|_\xi T_\xi^{-1} \\ &\approx T_\xi \left[ I + i_b h \delta_\xi \Lambda_A - i_b J^{-1} \varepsilon_I \delta_\xi^2 J \right] T_\xi^{-1} \end{aligned} \quad (2.28)$$

where the implicit smoothing factor  $\varepsilon_I = K_I h \sigma_A$  with  $K_I$  a user-specified constant,  $h$  the time step and  $\sigma_A$  the spectral radius of the matrix  $A$ .

Moving  $T_\xi$  and  $T_\xi^{-1}$  outside of the difference operator  $\delta_\xi$  introduces an error which renders the method (at best) first-order accurate in time (see Pulliam and Chaussee [1981]). For steady-state calculations, the right hand side of Equation (2.25) goes to zero as  $\Delta \hat{Q}^n \rightarrow 0$ , and the converged solution obtained using the diagonal algorithm is identical to that obtained from the original Beam-Warming ADI scheme since the right hand side is the same for both methods.

### 2.2.3 The LU-ADI Algorithm

The scalar tridiagonal matrices of the implicit operators can be further reduced to products of lower and upper bidiagonal matrices (see Obayashi and Kuwahara [1986], and Fujii and Obayashi [1986a, 1986b]). This results in a further reduction in the computational cost.

By decomposing the central differencing in Equation (2.28) into two one-sided differences using the flux vector splitting technique of Steger and Warming [1981], the  $\xi$ -direction operator becomes

$$\left[ I + i_b h \delta_\xi A - i_b D_l \Big|_\xi \right] = T_\xi \left[ I + i_b \nabla_\xi \Lambda_A^+ + i_b \Delta_\xi \Lambda_A^- \right] T_\xi^{-1} \quad (2.29)$$

with

$$\Lambda_A^\pm = \frac{h}{2} (\Lambda_A \pm |\Lambda_A|) \pm \underline{J}^{-1} \varepsilon_r J \quad (2.30)$$

where  $\Lambda_A^+$  contains all the positive eigenvalues and  $\Lambda_A^-$  contains all the negative eigenvalues,  $\varepsilon_r$  is the implicit artificial dissipation term, and  $\underline{J}^{-1}$  is the inverse of the Jacobian evaluated at the central point.

Using first-order upwind differences, Equation (2.29) can be written as

$$\left[ I + i_b h \delta_\xi A - i_b D_l \Big|_\xi \right] = T_\xi \left[ L_A + D_A + U_A \right] T_\xi^{-1} \quad (2.31)$$

where  $L_A$ ,  $D_A$  and  $U_A$  are lower bidiagonal, diagonal and upper bidiagonal matrices, respectively, and are given by

$$\begin{aligned}
L_A &= -i_b \Lambda_{A,j-1}^+ \\
D_A &= I + i_b (\Lambda_{A,j}^+ - \Lambda_{A,j}^-) \\
U_A &= i_b \Lambda_{A,j+1}^-
\end{aligned} \tag{2.32}$$

Applying the diagonally dominant factorization (see Lombard et al [1983]) gives

$$L_A + D_A + U_A = (L_A + D_A) D_A^{-1} (D_A + U_A) + O(h^2) \tag{2.33}$$

where higher order terms are dropped since  $D_A$  is of order 1 and  $L_A$  and  $U_A$  are of order  $h$ .

Substituting Equation (2.33) into Equation (2.31), the LU factorization for the ADI operator in the  $\xi$ -direction becomes

$$\left[ I + i_b h \delta_\xi A - i_b D_l \Big|_\xi \right] = T_\xi \underbrace{\left[ L_A + D_A \right]}_{\text{lower bidiagonal}} \underbrace{\left[ D_A^{-1} (D_A + U_A) \right]}_{\text{upper bidiagonal}} T_\xi^{-1} \tag{2.34}$$

A similar procedure is followed for the  $\eta$ - and  $\zeta$ -directions. The block tridiagonal matrix inversion for each direction has been reduced to a product of a lower and an upper scalar bidiagonal matrix. It is implemented by performing a forward sweep followed by a backward sweep.

To ensure adequate stability of the thin-layer viscous terms while using the diagonally dominant factorization, it is required to add a small amount of additional dissipation to the split diagonal matrices  $\Lambda_c^\pm$  (see Fujii and Obayashi [1986a]) as follows:

$$\Lambda_c^\pm = \frac{h}{2} (\Lambda_c \pm |\Lambda_c|) \pm \underline{J}^{-1} \epsilon_l J \pm \nu I \tag{2.35}$$

where

$$v = \frac{2\mu(\zeta_x^2 + \zeta_y^2 + \zeta_z^2)}{Re\rho\Delta\zeta} \quad (2.36)$$

Finally, the LU-ADI algorithm can be summarized as follows:

$$\begin{aligned} & T_\xi(L_A + D_A)D_A^{-1}(D_A + U_A)T_\xi^{-1}T_\eta(L_B + D_B)D_B^{-1}(D_B + U_B)T_\eta^{-1} \\ & T_\zeta(L_C + D_C)D_C^{-1}(D_C + U_C)T_\zeta^{-1}\Delta\hat{Q}^n \quad (2.37) \\ & = -i_b h \left[ \delta_\xi \hat{E}^n + \delta_\eta \hat{F}^n + \delta_\zeta \hat{G}^n - \frac{1}{Re} \delta_\zeta \hat{S}_v^n \right] - i_b \left[ D_E|_\xi + D_E|_\eta + D_E|_\zeta \right] \hat{Q}^n \end{aligned}$$

Analytical expressions for  $T_\xi^{-1}T_\eta$  and  $T_\eta^{-1}T_\zeta$  and their inverses can be found in Pulliam and Chaussee [1981] to reduce the computational effort. The inversion process in each direction consists of one forward scalar sweep and one backward scalar sweep.

## 2.3 Turbulence Model

For high Reynolds number flows, turbulence closure is required to account for the Reynolds stresses. By relating the Reynolds stresses to the rates of strain using the Bousinesq assumption, the effect of turbulence can be approximated by an eddy viscosity which accounts for the additional mixing caused by the turbulent flow. A two-layer algebraic turbulence model of Baldwin and Lomax [1978] is used in the present study. Since jet flows possess different turbulence characteristics, an eddy viscosity model proposed by Roberts [1987] for turbulent curved wall jet is implemented in the wall jet region for the wing-tip blowing cases.

### 2.3.1 The Baldwin-Lomax Model

The eddy viscosity is evaluated in inner and outer layers,

$$\mu_t = \begin{cases} (\mu_t)_{\text{inner}}, & y \leq y_{\text{crossover}} \\ (\mu_t)_{\text{outer}}, & y > y_{\text{crossover}} \end{cases} \quad (2.38)$$

where  $y$  is the normal distance from the wall and  $y_{\text{crossover}}$  is the smallest value of  $y$  at which the inner and outer values of  $\mu_t$  are equal.

The eddy viscosity in the inner region is estimated using the Prandtl-Van Driest formulation:

$$(\mu_t)_{\text{inner}} = \rho l^2 |\omega| \quad (2.39)$$

where  $|\omega|$  is the magnitude of the vorticity  $(|\nabla \times \vec{V}|)$  and  $l$  is the “mixing” length scale given by

$$l = ky[1 - \exp(-y^+/A^+)] \quad (2.40)$$

where  $k = 0.4$ ,  $y^+ = y\sqrt{\rho_w \tau_w}/\mu_w$  with the subscript  $w$  denotes values at the wall and  $A^+ = 26$ .

The Clauser formulation used in the Cebeci model for the outer layer is replaced by

$$(\mu_t)_{\text{outer}} = KC_{cp} F_{\text{wake}} F_{\text{Kleb}}(y) \quad (2.41)$$

where the Clauser constant  $K = 0.0168$ ,  $C_{cp} = 1.6$  and

$$F_{\text{wake}} = \min(y_{\text{max}}, C_{wk} y_{\text{max}} U_{\text{dif}}^2 / F_{\text{max}}) \quad (2.42)$$

with  $C_{wk} = 0.25$  and  $U_{dif}$  is the difference between the maximum and the minimum total velocity magnitudes in the profile along the  $y$ -direction. The minimum total velocity magnitude is zero except in the wakes. The values of  $y_{max}$  and  $F_{max}$  are determined from the function

$$F(y) = y|\omega|[1 - \exp(-y^+/A^+)] \quad (2.43)$$

The quantity  $F_{max}$  is the maximum value of  $F(y)$  in the profile along the  $y$ -direction, and  $y_{max}$  is the value of  $y$  at which it occurs. The function  $F_{Kleb}(y)$  is the Klebanoff intermittency factor given by

$$F_{Kleb}(y) = [1 + 5.5(C_{Kleb}y/y_{max})^6]^{-1} \quad (2.44)$$

with  $C_{Kleb} = 0.3$ .

The total effective viscosity can then be obtained as the sum of the laminar viscosity ( $\mu_l$ ) and the turbulent viscosity ( $\mu_t$ ):

$$\mu = \mu_l + \mu_t \quad (2.45)$$

The laminar viscosity is determined from Sutherland's formula:

$$\mu_l = \mu_{ref} \left( \frac{T}{T_{ref}} \right)^{3/2} \frac{T_{ref} + 198.6 \text{ } ^\circ R}{T + 198.6 \text{ } ^\circ R} \quad (2.46)$$

where  $T$  is the temperature in degrees Rankine ( $^\circ R$ ).

The total effective coefficient of thermal conductivity can be obtained by

$$k = k_l + k_t = \frac{C_p \mu_l}{Pr_l} + \frac{C_p \mu_t}{Pr_t} \quad (2.47)$$

For the range of temperatures and pressures of interest here, for air, the laminar Prandtl number  $Pr_l = 0.72$  and the turbulent Prandtl number  $Pr_t = 0.90$  (see, for example, Anderson et al [1984]).

### 2.3.2 Turbulence Model for Wall Jet

The algebraic eddy viscosity model developed by Roberts [1987] for turbulent curved wall jets is used in the wall jet region on the wing surface for the axial wing-tip blowing cases. This model has been previously used in the leading edge blowing for delta-wing (see Yeh et al [1989]) and tilt-rotor (see Fejtek and Roberts [1992]) applications.

Assuming self-similar mean velocity profiles, the eddy viscosity of a wall jet is given by

$$\mu_t = \frac{K}{4k^2} b V_{\max} \left( \frac{\zeta}{\zeta_{\max}} \right)^2 \quad (2.48)$$

where  $K = 0.073$ ,  $k = 0.8814$ ,  $V_{\max}$  is the maximum velocity,  $\zeta$  is the distance normal from the wall,  $b$  is the normal distance from the wall where the velocity is  $V_{\max}/2$ , and  $\zeta_{\max}$  is the normal distance from the wall where the velocity is  $V_{\max}$ . By correlating with the experimental results,  $b$  is found to have a value of about  $7\zeta_{\max}$ . For  $\zeta > \zeta_{\max}$ ,  $\zeta/\zeta_{\max}$  is set to one.

By including the effects of the wall curvature, the eddy viscosity is modified as follows:

$$\mu_t = \frac{7K}{4k^2} V_{\max} \zeta_{\max} \left( \frac{\zeta}{\zeta_{\max}} \right)^2 \left( 1 - \frac{V/R}{\partial V/\partial \zeta} \right) \quad (2.49)$$

where  $R$  is the radius of curvature of the wall. This wall jet model is applied from the jet exit slot to the flow separation point.

## 2.4 Artificial Dissipation

The Beam-Warming algorithm, although unconditionally stable for two-dimensional flows, is unconditionally unstable for three-dimensional flows (see Pulliam [1984]). Artificial dissipation is therefore necessary to stabilize the scheme. In addition to the explicit artificial dissipation, implicit artificial dissipation is added to increase the stability bound imposed by the explicit artificial dissipation and to speed up the convergence rate.

The commonly used fourth-order artificial dissipation tends to produce an undesirable oscillatory solution near flow discontinuities such as shock waves. The second-order artificial dissipation, on the other hand, is too dissipative for other part of the flowfield even though it is able to damp out oscillations near flow discontinuities. An artificial dissipation model employing a nonlinear combination of second-order and fourth-order smoothing proposed by Obayashi et al [1988] is used in the present study.

The explicit smoothing term, for the  $\xi$ -direction, is given by

$$D_E|_{\xi} \hat{Q}^n = \nabla_{\xi} \left\{ \left( I - \Phi_{j+\frac{1}{2}} \right) \left( \frac{\epsilon_E}{J} \right)_{j+\frac{1}{2}} \Delta_{\xi} J \hat{Q}^n - \Phi_{j+\frac{1}{2}} \nabla_{\xi} \Delta_{\xi} \left[ \left( \frac{\epsilon_E}{J} \right)_{j+\frac{1}{2}} \Delta_{\xi} J \hat{Q}^n \right] \right\} \quad (2.50)$$

where

$\Phi$  = matrix containing the flux limiter function

$$\varepsilon_E = K_E h \sigma_A$$

$K_E$  = input constant

$\sigma_A$  = spectral radius of flux Jacobian matrix  $A$

$$= |U| + a \sqrt{\xi_x^2 + \xi_y^2 + \xi_z^2}$$

The flux limiter function  $\Phi$  varies from 0 to 1 depending the local flow gradient. For a relatively smooth solution, a value near one is used so that only the fourth-order dissipation is applied. Whereas for large flow gradients, a value near zero is used so that the second-order dissipation terms become dominant. More details on the flux limiter function are discussed in Obayashi et al [1988].



# Chapter 3

## Grid Generation

### 3.1 General Remarks

Grid generation is an essential part of the overall computation of a fluid flow problem. Over the years various grid generation techniques have been developed and they can be broadly categorized into structured and unstructured grid generation methods. The structured grid generation methods can be further sub-divided into three main categories: (1) analytic methods, (2) algebraic methods, and (3) schemes based on partial differential equations. Each of these methods has its strength and weaknesses. These methods are discussed in more details in Anderson et al [1984].

To fully exploit the advantages of the grid generation method to be used, it is important to have a good understanding of the nature of the governing equations, the geometry of the flow field, and the expected flow behavior. For example, schemes based on partial differential equations are very attractive for

generating very smooth grids and allowing good grid spacing and orthogonality control. Their greatest drawback is that they are computationally expensive especially for three-dimensional applications. So far, most of the trailing vortex studies have employed geometrically simple lifting surfaces. Wings of symmetrical airfoil section, no twist, and no taper have been commonly used (see, for example, Spivey [1968], Yip and Shubert [1976], McAlister and Takahashi [1991], and Chow et al [1993]). The simple geometry allows a three-dimensional grid with good grid properties to be generated economically using schemes based on partial differential equations. This is achieved by first generating a two-dimensional grid at one spanwise station using schemes based on partial differential equations. A three-dimensional grid enveloping the complete lifting surface and the desired flow domain is then obtained by “stacking” the two-dimensional grid along the wing span. A grid generation method based on elliptic partial differential equations first proposed by Thompson et al [1974] is employed to generate the two-dimensional grid. Details of the method are presented in Section 3.2.

Grid generation methods based on the unstructured grid philosophy have the advantage of tackling problems with complex geometry and flowfield elegantly. Strawn [1991] applied the unstructured adaptive-grid method to calculate the trailing vortex flowfield by solving the Euler equations. One difficulty encountered by Strawn [1991] was that the aspect ratio of the tetrahedral elements became more and more nonuniform for regions farther downstream. Flow solutions became deteriorated quickly in these regions.

## 3.2 Elliptic Grid Generation Method

### 3.2.1 Thompson, Thames, and Mastin Method

The ability of the elliptic grid generation method to generate very smooth and well behaved grids has made it one of the most widely used grid generation techniques for aerodynamic applications. The method was first proposed by Thompson, Thames, and Mastin [1974]. It was motivated by the smoothness properties associated with elliptic partial differential equation solutions. Successful applications by Thompson et al [1975, 1977a, 1977b] further popularized this method.

In the present application, the elliptic grid generation method is used to generate a smooth, body-fitted, curvilinear two-dimensional grid. Grid points along the inner boundary, which includes the airfoil surface, and the outer boundary are specified. Interior grid points are first obtained by interpolation. They are subsequently smoothed by the elliptic grid generation scheme which is outlined below.

The mapping of the physical domain to the computational domain is defined by the Poisson equations as follows:

$$\begin{aligned}\xi_{xx} + \xi_{zz} &= P(\xi, \zeta) \\ \zeta_{xx} + \zeta_{zz} &= Q(\xi, \zeta)\end{aligned}\tag{3.1}$$

where  $(x, z)$  are the coordinates in the physical domain and  $(\xi, \zeta)$  are those in the computational domain. The source terms,  $P$  and  $Q$ , are used to control the grid properties. Grid points in the computational domain, for the two-

dimensional application, are rectangular and evenly-spaced. Thus, in this way,  $(\xi, \zeta)$  are known. The unknowns are  $(x, z)$  in the physical domains. To determine  $(x, z)$  the dependent and independent variables in Equation (3.1) are interchanged. This results in the following transformed equations:

$$\begin{aligned}\alpha x_{\xi\xi} - 2\beta x_{\xi\zeta} + \gamma x_{\zeta\zeta} &= -J^2(P x_\xi + Q x_\zeta) \\ \alpha z_{\xi\xi} - 2\beta z_{\xi\zeta} + \gamma z_{\zeta\zeta} &= -J^2(P z_\xi + Q z_\zeta)\end{aligned}\tag{3.2}$$

where

$$\begin{aligned}\alpha &= x_\zeta^2 + z_\zeta^2 \\ \beta &= x_\xi x_\zeta + z_\xi z_\zeta \\ \gamma &= x_\xi^2 + z_\xi^2 \\ J &= x_\xi z_\zeta - x_\zeta z_\xi\end{aligned}\tag{3.3}$$

Equation (3.2) can thus be discretized and solved numerically as long as  $P$  and  $Q$  are specified. For the present application, the alternating direction implicit (ADI) algorithm, which uses the approximate factorization to convert the left-hand-side matrix of Equation (3.2) into two tridiagonal matrices to enhance computational efficiency during matrix inversion, is employed. Details of the implementation of the algorithm can be found, for example, in Holst [1983].

### 3.2.2 Middlecoff-Thomas Algorithm

It is noticed in Equation (3.1) that when  $P = Q = 0$  the Poisson equations are reduced to the Laplace equations. This will provide no control over the grid point spacing near a boundary. The grid points tend to be pulled away from the

surface (see, for example, Sorenson and Steger [1980]). The specification of  $P$  and  $Q$  therefore becomes a main concern. The original  $P$  and  $Q$  terms proposed by Thompson et al [1974] require four user-specified coefficients to control the grid properties. The major setback of this proposal is that these user-specified coefficients are rather difficult to obtain in a relatively automatic way.

To overcome this difficulty, Steger and Sorenson [1979], and Middlecoff and Thomas [1979] devised some automatic grid control techniques that significantly reduce the number of free parameters that need to be specified. In the present application, the Middlecoff-Thomas algorithm, which is outlined below, is employed.

The  $P$  and  $Q$  terms are defined by Middlecoff and Thomas [1979] in terms of two other functions  $\phi$  and  $\psi$ , which are given by

$$\begin{aligned} P &= \phi(\xi, \zeta)(\xi_x^2 + \xi_z^2) \\ Q &= \psi(\xi, \zeta)(\zeta_x^2 + \zeta_z^2) \end{aligned} \quad (3.4)$$

Substituting Equation (3.4) into Equation (3.2) gives

$$\begin{aligned} \alpha(x_{\xi\xi} + \phi x_\xi) - 2\beta x_{\xi\zeta} + \gamma(x_{\zeta\zeta} + \psi x_\zeta) &= 0 \\ \alpha(z_{\xi\xi} + \phi z_\xi) - 2\beta z_{\xi\zeta} + \gamma(z_{\zeta\zeta} + \psi z_\zeta) &= 0 \end{aligned} \quad (3.5)$$

The  $\phi(\xi, \zeta)$  and  $\psi(\xi, \zeta)$  terms are established in an automatic way from user-specified boundary conditions on  $x$  and  $z$  as follows:

For  $\xi = \text{constant}$  boundaries,

$$\begin{aligned}
\psi(\xi_{\min}, \zeta) &= -z_{\zeta\zeta}/z_{\zeta}|_{\xi=\xi_{\min}} && \text{for } |z_{\zeta}| > |x_{\zeta}| \\
\psi(\xi_{\min}, \zeta) &= -x_{\zeta\zeta}/x_{\zeta}|_{\xi=\xi_{\min}} && \text{for } |x_{\zeta}| > |z_{\zeta}| \\
\psi(\xi_{\max}, \zeta) &= -z_{\zeta\zeta}/z_{\zeta}|_{\xi=\xi_{\max}} && \text{for } |z_{\zeta}| > |x_{\zeta}| \\
\psi(\xi_{\max}, \zeta) &= -x_{\zeta\zeta}/x_{\zeta}|_{\xi=\xi_{\max}} && \text{for } |x_{\zeta}| > |z_{\zeta}|
\end{aligned} \tag{3.6}$$

For  $\zeta = \text{constant}$  boundaries,

$$\begin{aligned}
\phi(\xi, \zeta_{\min}) &= -x_{\xi\xi}/x_{\xi}|_{\zeta=\zeta_{\min}} && \text{for } |x_{\xi}| > |z_{\xi}| \\
\phi(\xi, \zeta_{\min}) &= -z_{\xi\xi}/z_{\xi}|_{\zeta=\zeta_{\min}} && \text{for } |z_{\xi}| > |x_{\xi}| \\
\phi(\xi, \zeta_{\max}) &= -x_{\xi\xi}/x_{\xi}|_{\zeta=\zeta_{\max}} && \text{for } |x_{\xi}| > |z_{\xi}| \\
\phi(\xi, \zeta_{\max}) &= -z_{\xi\xi}/z_{\xi}|_{\zeta=\zeta_{\max}} && \text{for } |z_{\xi}| > |x_{\xi}|
\end{aligned} \tag{3.7}$$

All derivatives are discretized using central differences. Interior values of  $\phi$  and  $\psi$  are obtained using linear interpolation.

The Middlecoff-Thomas algorithm has been proven to be simple and effective in grid control. Furthermore, interior grid point distribution tends to approximately mimic the boundary distribution of grid points. Grid points that are clustered in one direction on the boundary will tend to remain clustered in that same fashion in the grid interior. This allows the user a better control in clustering grid points to capture regions of high flow gradient.

## 3.3 Grid Details

### 3.3.1 Geometry of Wing

To illustrate the grid generation used in the present trailing vortex study, a semi-span rectangular wing with a constant and untwisted NACA 0015 symmetric airfoil profile along the entire span and a rounded wing-tip shape is used. The wing has a full-span aspect ratio of 6.75. The same geometry was used in the fixed-wing trailing vortex experiment of McAlister and Takahashi [1991], which was conducted in the NASA Ames 7- by 10-Foot Subsonic Wind Tunnel No. 2. A perspective view of the semi-span wing is shown in Figure 3.1.

### 3.3.2 Two-Dimensional Grid

Due to the simplicity of the geometry, a two-dimensional grid is first generated using the elliptic grid generation method (discussed in Section 3.2). Symmetry of the airfoil section also enables only the upper half of the grid to be generated (see Figure 3.2). This further reduces the cost in grid generation.

As discussed in Section 2.1, the application of the thin-layer approximation to the governing Navier-Stokes equations has limited the computer memory and computational time requirements to a manageable level. To resolve the viscous fluxes normal to the lifting surface, which are the dominant contribution to the overall viscous fluxes, very fine grid points must be clustered near the lifting surface so as to capture the high velocity gradient in the boundary layer. In addition, very fine grid points must be clustered aft of the trailing edge in order to capture the wake, the lifting vortex sheet, and the

trailing vortex effects. The C-grid topology, as opposed to the O- and H-grid topologies, is selected because grid points can be clustered more efficiently to capture these flow features. Furthermore, the O-grid topology has a mapping singularity at the trailing edge of all sharp-trailing-edge airfoils; and the H-grid topology places a singularity at the leading edge of all blunt-leading-edge airfoils. The C-grid topology, on the other hand, is free from these singularity mapping problems.

Fine grid clustering in the streamwise direction is also required at the leading edge of the airfoil section to capture the high velocity gradient and the high leading edge suction peak. The trailing vortex problem also demands fine grid clustering at the trailing edge in the streamwise direction, especially near the wing-tip region. It was observed (see, for example, Spivey [1968], Yip and Shubert [1976], McAlister and Takahashi [1991], and Chow et al [1993]) that high suction peak (or peaks) occurred on the upper surface of the wing-tip region due to the presence of the rolled-up tip vortex (or vortices depending on the geometry of the wing-tip). To capture this effect, fine grid has to be clustered there.

Aft of the trailing edge near the wing tip region, the trailing vortex continues to develop and roll up. The distance required for the trailing vortex to completely roll up depends on the aspect ratio, lift distribution, etc, of the wing (see Spreiter and Sacks [1951]). Fine grids must therefore be clustered aft of the trailing edge near the wing tip region for some downstream distance to capture the formation of the trailing vortex.

To ensure fine and smooth grid clustering in the streamwise direction near the leading and trailing edges of the airfoil section, a cosine stretching function is employed. Stretching is also employed aft of the trailing edge in the downstream direction to ensure fine clustering near the trailing edge and smooth stretching of grid farther downstream. It is found to be difficult to use the cosine stretching for grid points aft of the trailing edge. Smooth grid transition near the trailing edge cannot be obtained with the present amount of grid points available because the downstream distance is much greater as compared to the chord length. A geometric stretching is used instead to cluster grid points aft of the trailing edge.

The geometric stretching is probably the simplest stretching method. To distribute  $N$  number of points along a curve of length  $S$ , with the arc length between the first two points of  $\Delta S$ , the total length can be written as

$$\Delta S + \alpha \Delta S + \alpha^2 \Delta S + \dots + \alpha^{N-2} \Delta S + \alpha^{N-1} \Delta S = S \quad (3.8)$$

where  $\alpha$  is the stretching factor.

The Newton-Raphson iterative root finding method can be used to determine  $\alpha$  such that Equation (3.8) is satisfied. It is implemented by multiplying Equation (3.8) by  $\alpha$  and then subtract this new equation from Equation (3.8). This results in the following equation:

$$(\alpha - 1)S - (\alpha^N - 1)\Delta S = 0 = f \quad (3.9)$$

Notice that a function  $f$  is defined in the iterative procedure. The objective of the iteration is to determine a value  $\alpha$  such that  $f = 0$  is satisfied within a desired tolerance.  $\alpha$  is determined iteratively via

$$\alpha_{n+1} = \alpha_n - \frac{f}{f'} \quad (3.10)$$

where  $n$  is the iterative time step and

$$f' = S - N \alpha^{N-1} \Delta S \quad (3.11)$$

This method does not provide any control on the size of the last grid spacing. A more sophisticated method developed by Vinokur [1983] allows control on the last grid spacing. However, for external flow aerodynamic applications, the control of the size of the last grid spacing is not critical. Geometric stretching is also used to generate grid points normal to the wing surface.

### 3.3.3 Three-Dimensional Grid

To generate a three-dimensional grid, the two-dimensional grid, illustrated in Figure 3.2, is “stacked” along the wing span starting from the upper surface of the wing center-plane. The two-dimensional grid is then wrapped around the wing-tip to form a rounded wing-tip. “Stacking” of the two-dimensional grid continues until the lower surface of the wing center-plane is reached. Orthogonality of the two-dimensional planes with the wing surface is ensured during the “stacking” process. A cut-away-view in the  $y$ - $z$  plane of the grid generated is shown in Figure 3.3. (The standard right-hand aeronautical convention is used for the  $x$ - $y$ - $z$  body-axis coordinate system: the origin of the body-axis coordinate system is at the intersection of the wing center-plane and the wing leading edge,  $x$  is positive from the leading edge to the trailing edge,  $y$  is positive toward the tip of the pilot’s right wing, and  $z$  is positive upward.)

Similar to the experimental setup, only the semi-span of the wing is considered due to the symmetry of the flow configuration. Implicit in the use of a plane of symmetry is the assumption that the flowfields on either side of the center-plane are a mirror image of each other. To facilitate the specification of the boundary condition at the center-plane, the two-dimensional grid actually extends one grid plane inboard of the plane of symmetry; and the distances of these two planes from the plane of symmetry are equal. Flow conditions at this plane are forced to be those at the first plane from the center-plane on the pilot's right wing to preserve symmetry of the flow. This arrangement is deemed to simulate the actual flow more closely as compared with the experimental setup whereby boundary layer growth from the wall at which the wing is mounted may interfere with the actual flow.

Cosine stretching is used to cluster grid points in the spanwise direction. This allows fine clustering of grid points around the wing tip so as to capture the trailing vortex better. A cut-away isometric view of the wing and the three-dimensional computational grid is shown in Figure 3.4.

Most of the results presented are based on computations using 83x69x61 (i.e., 349,347) grid points. There are 83 points in the  $\xi$ -direction with 48 points defining half of the airfoil section and 35 points downstream of the trailing edge. The grid extends 8 wing chords from the trailing edge to the outflow boundary. 69 two-dimensional grid planes are "stacked" in the spanwise  $\eta$ -direction with 25 planes defining the rounded wing tip. There are 60 grid points stretch from the wing surface to the outer boundary in the  $\zeta$ -direction. The grid extends to 6

wing chords normal to the wing surface and 6 wing chords ahead of the wing leading edge.

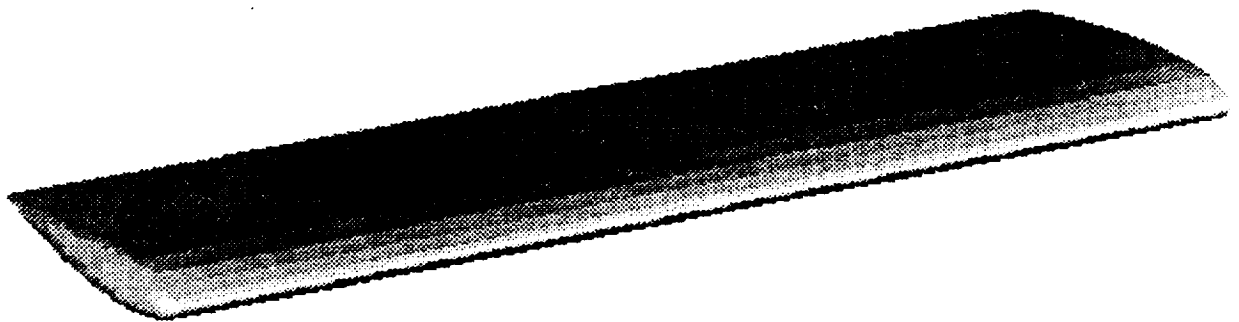


Figure 3.1: Geometry of the semi-span wing having a NACA 0015 symmetric airfoil section, with no twist, no taper, no sweep, and a rounded wing-tip.

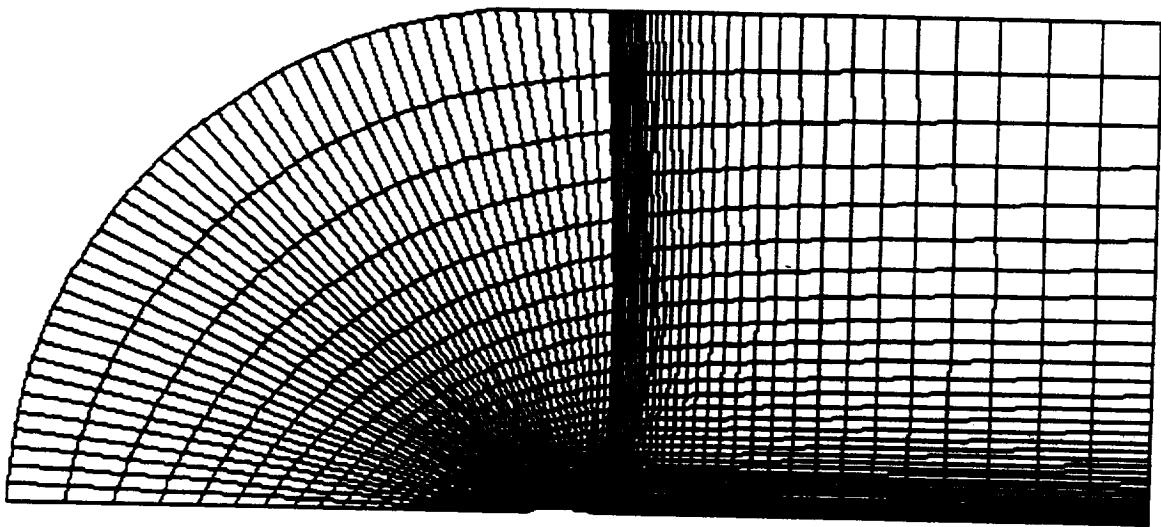


Figure 3.2: Two-dimensional grid at the wing center-plane showing the C-grid topology. Fine clustering of grid points at the leading edge, the trailing edge, aft of the trailing edge, and close to the wing surface.

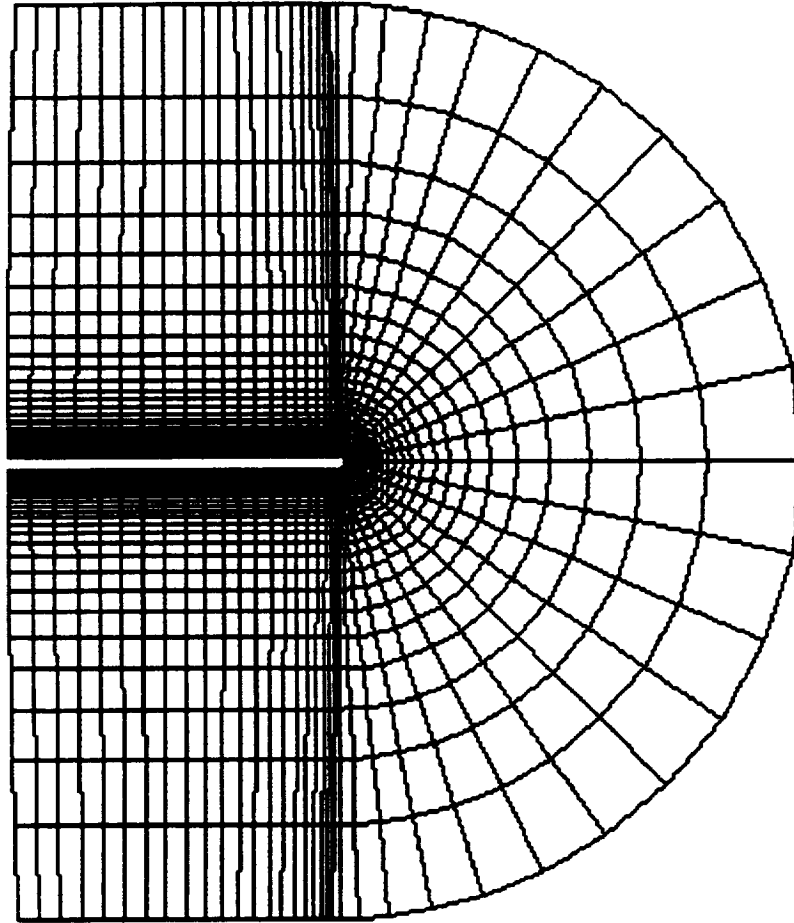


Figure 3.3: A  $y$ - $z$  plane view (looking upstream) of the three-dimensional grid showing the rounded wing-tip of the wing and the fine clustering of grid points around the wing-tip to capture the wing-tip vortex.

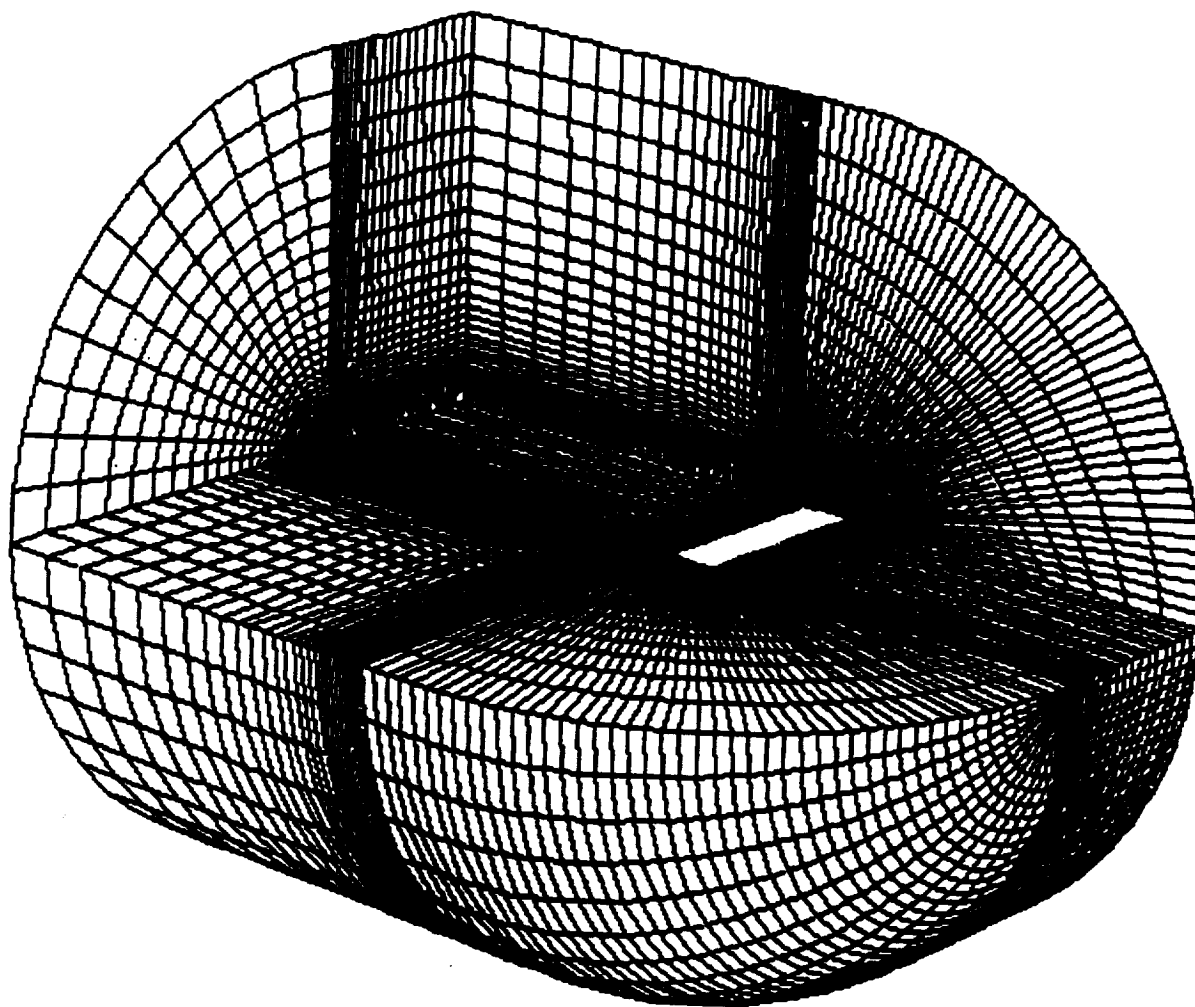


Figure 3.4: A cut-away isometric view of the wing and the three-dimensional computational grid.

# **Chapter 4**

## **Boundary Conditions**

### **4.1 General Remarks**

Boundary conditions at the flowfield domain boundaries are the driving force in determining the overall flowfield solution. In the implementation of the numerical algorithm, the boundary conditions can be specified either implicitly or explicitly. When specified implicitly, the boundary conditions are coupled and coded into the numerical algorithm. Explicit specification of the boundary conditions, on the other hand, requires that flow variables at the boundaries to be evaluated using the most recent solution. Due to the fact that explicit treatment of the boundaries leads to a far more simple and flexible scheme, where boundary conditions become a modular element that can be put in or pulled out of a computer program without disturbing the implicit algorithm (see Pulliam and Steger [1980]), it is implemented in the present study. The flexibility of the explicitly specified boundary conditions also allows wing-tip blowing (to be discussed in section 4.3) to be incorporated into the numerical study easily.

## 4.2 Boundary Conditions

On the surface of the wing, no-slip boundary condition is imposed, that is, all components of velocity are set to zero ( $u = v = w = 0$ ) for viscous (Navier-Stokes) computations.

The pressure on the wing surface is obtained by solving the normal momentum equation (see Steger [1977] and Pulliam and Steger [1980]):

$$\begin{aligned}
 & p_\xi (\xi_x \zeta_x + \xi_y \zeta_y + \xi_z \zeta_z) + p_\eta (\eta_x \zeta_x + \eta_y \zeta_y + \eta_z \zeta_z) + p_\zeta (\zeta_x^2 + \zeta_y^2 + \zeta_z^2) \\
 &= -\rho U (\zeta_x u_\xi + \zeta_y v_\xi + \zeta_z w_\xi) - \rho V (\zeta_x u_\eta + \zeta_y v_\eta + \zeta_z w_\eta) \\
 &= p_n \sqrt{\zeta_x^2 + \zeta_y^2 + \zeta_z^2} \\
 &= 0
 \end{aligned} \tag{4.1}$$

Notice that  $p_n = \partial p / \partial n = 0$  at the body surface and  $n$  is the direction normal to the body surface.

By setting  $U$  and  $V$  to zero at the body surface for viscous computations and discretizing the derivatives using second-order central differences in the  $\xi$ - and  $\eta$ -directions and second-order one-sided differences in the  $\zeta$ -direction,  $p$  at the body surface can be calculated by solving the implicit equations using the approximate factorization technique.

Once the pressure at the body surface is determined, the total energy per unit volume,  $e$ , can be calculated using Equation (2.7). By assuming adiabatic wall conditions (i.e., no heat flux across the wall or  $\partial T / \partial n = 0$ ), and using the relation  $\partial p / \partial n = 0$  at the wall, it is necessary that  $\partial \rho / \partial n = 0$  at the body surface as well from the ideal gas equation ( $p = \rho RT$ ). The density at the body surface is

then calculated using the zero-order extrapolation from the nearest point normal to the surface.

Due to the symmetry of the flowfield only half of the wing span is modeled to reduce the computational cost. The symmetric boundary conditions at  $k = 1$  and  $k = 3$  (which are next to the plane of symmetry or mid-span:  $k = 2$ ) are imposed as follows:

$$\begin{aligned}
 \rho_1 &= \rho_3 \\
 (\rho u)_1 &= (\rho u)_3 \\
 (\rho v)_1 &= -(\rho v)_3 \\
 (\rho w)_1 &= (\rho w)_3 \\
 e_1 &= e_3
 \end{aligned} \tag{4.2}$$

For the outer boundaries, freestream conditions are imposed on the inflow boundary whereas characteristics-based formulation is applied at the outflow boundary. For example, the present trailing vortex problem involves subsonic flow in three dimensions. In this case, only one state variable is to be specified at the outflow boundary and the remaining four variables must be obtained from the characteristic relations because four of the characteristic velocities are positive and the fifth one is negative. Zero-order extrapolation is used in obtaining the four variables at the outflow boundary from the interior solution.

### 4.3 Wing-Tip Blowing

The blowing intensity is quantified by the blowing momentum coefficient,  $C_\mu$ , which is defined as

$$C_{\mu} = \frac{\iint_{A_{jet}} \rho_{jet} V_{jet} \vec{V}_{jet} \cdot d\vec{A}_{jet}}{q_{\infty} S_{ref}} \quad (4.3)$$

where  $\rho_{jet}$  is the jet exit density,  $V_{jet}$  is the jet exit velocity,  $A_{jet}$  is the jet slot area,  $q_{\infty}$  is the freestream dynamic pressure, and  $S_{ref}$  is the wing reference area, which is simply the full-span wing planform area.

### 4.3.1 Actuator Plane Concept

For the case of axial wing-tip blowing, a step in the wing surface is formed by the blowing slot. To simplify the grid generation required in this study, the jet slot is not resolved and an actuator plane concept is employed to model the wall jet. A schematic sketch of the actuator plane concept is presented in Figure 4.1. The actuator plane is, in effect, a discontinuity imposed at the jet slot location whereby the flow variables undergo a discontinuous change and the jet is modeled as a one-sided source of mass, momentum and energy. This concept has been successfully applied to the F-18 forebody (see Tavella et al [1990]), an ogive cylinder (see Font and Tavella [1991]), a tilt-rotor (see Fejtek and Roberts [1992]) and a delta-wing (see Craig [1993]). Tavella et al [1990] compared the results obtained by using the actuator plane concept with those obtained by Yeh et al [1989] who resolved the jet slot and found that the differences were not significant.

For the case of spanwise wing-tip blowing, no step on the wing surface is formed by the jet slot. The jet can therefore be modeled at the wing surface in a straight-forward manner.

### 4.3.2 Solution Blanking Feature of Chimera Scheme

In modeling the wall jet for the axial wing-tip blowing case,  $L_{jet}$  number of grid points normal to the wing surface at the jet slot location are used to define the jet slot thickness. In order to avoid the flowfield solution being solved at the jet slot location, Craig [1993] used the multi-zonal approach and defined the jet slot location at the inter-zonal boundary. This approach is not very practical because when one changes the jet slot location, for example for parametric study, one has to change the entire computational grid and re-calculate the entire flowfield. The approach of employing the solution blanking feature of the chimera scheme adopted by Fejtek and Roberts [1992] is instead used in the present study. By blanking off the implicit solution at the jet slot location and updating the solution explicitly with the “interior boundary conditions” defined by the jet, the jet slot can be located anywhere in the flowfield. This allows great flexibility in locating the jet slot without confining it to the inter-zonal boundary.

The static pressure at the jet slot exit is assumed to be the local static pressure just outside the jet width and constant across it for the axial wing-tip blowing case. For the spanwise wing-tip blowing case, the static pressure at the jet slot exit is also assumed to be the local static pressure; but it is allowed to vary across the jet width. Wing-tip blowing is applied by changing the total jet plenum supply pressure which is normalized by the freestream ambient pressure, i.e.,  $P_{plenum}/P_{\infty}$ .

The temperature at the jet slot exit is assumed to be freestream ambient. The jet exit density,  $\rho_{jet}$ , is calculated using the ideal gas equation. By assuming

isentropic expansion of the compressed air from the plenum pressure,  $p_{plenum}$ , to the local static pressure,  $p$ , the jet exit velocity is obtained by

$$V_{jet} = \sqrt{\left[ \left( \frac{p}{p_{plenum}} \right)^{-\frac{\gamma-1}{\gamma}} - 1 \right] \frac{2\gamma}{\gamma-1} \frac{p}{\rho}} \quad (4.4)$$

The total energy per unit volume at the jet slot exit is determined by Equation (2.7).

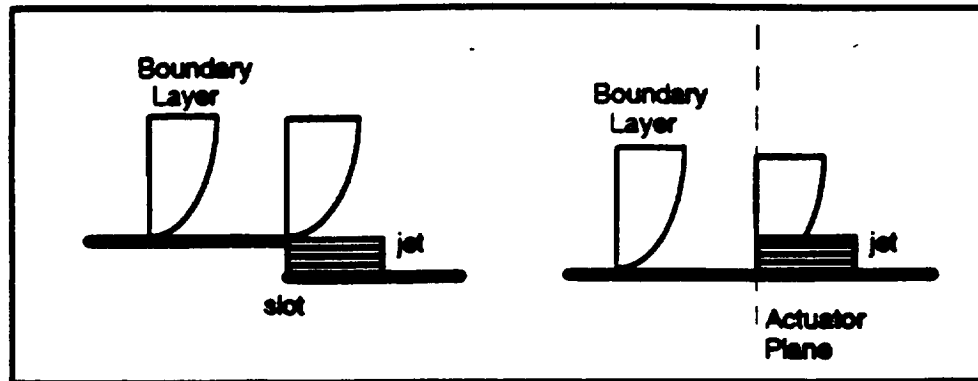


Figure 4.1: A schematic sketch of the actuator plane concept (taken from Craig [1993]).



# **Chapter 5**

## **Results and Discussion**

### **5.1 General Remarks**

Results obtained in this study are presented and discussed in this chapter. The chapter is divided into no blowing cases, axial wing-tip blowing cases and spanwise wing-tip blowing cases. Computational results are compared with experimental data and theoretical analyses. The effects of axial and spanwise wing-tip blowing on the performance of the wing and the behavior of the trailing vortices are also discussed.

### **5.2 No Blowing Cases**

#### **5.2.1 Configuration**

The configuration used in the present study for no blowing and axial wing-tip blowing cases is the fixed-wing trailing vortex experiment of McAlister and Takahashi [1991]. The experiment was conducted in the NASA Ames 7- by 10-Foot Subsonic Wind Tunnel No. 2. Semi-span configurations were considered in

the study and all the wings were rectangular and had a constant and untwisted NACA 0015 symmetric airfoil profile along the entire span. The lateral edge of each wing-tip was machined to a flat or square face, but could be made round by the addition of an end cap. For the present study, the rounded wing-tip configuration is considered. A perspective view of the semi-span wing is shown in Figure 3.1. With the rounded wing-tip end cap, the aspect ratio of the wing is 6.75. Three different chord lengths of 12.0, 16.2 and 20.4 inches were used in the experimental study. However, the aspect ratio remained fixed by changing the length of the wing span.

Computations were performed for angle-of-attack  $\alpha = 4^\circ$ ,  $8^\circ$ , and  $12^\circ$ , freestream Mach number  $M_\infty = 0.17$ , and freestream Reynolds number based on the wing chord  $Re = 2.0 \times 10^6$ .

### 5.2.2 General Flow Features

The rolling-up of the tip vortex and its subsequent convection downstream is depicted by the particle traces in Figure 5.1. It is observed that farther inboard, the flow remains very much two-dimensional.

Figure 5.2 (a) shows the side view of the trailing vortex. It is noticed that the tip vortex starts to roll up even before it reaches the trailing edge of the wing and that it eventually rolls up into the freestream direction and is convected downstream. This is also observed in the experiments (see, for example, McAlister and Takahashi [1991] and Chow et al [1993]). Figure 5.2 (b) shows the plan view of the trailing vortex. It is observed that as the trailing vortex moves downstream, it moves inboard asymptotically as well. For the present

rectangular wing, the trailing vortices move about 5% inboard at stations far downstream of the wing. Spreiter and Sacks [1951] showed that the trailing vortices could move inboard by as much as about 25% at stations several chord lengths behind the wing for an elliptically loaded wing. For elliptically loaded wings, the asymptotic spacing between the trailing vortices is independent of the angle of attack; whereas, for non-elliptically loaded wings, the asymptotic spacing is a function of the angle of attack (see Spreiter and Sacks [1951]).

Figure 5.3 shows the velocity vectors at the quarter-chord location. Notice that the flow accelerates from the higher pressure lower surface towards the lower pressure upper surface by going around the wing-tip. No-slip boundary conditions at the wall are observed for the Navier-Stokes computations.

### 5.2.3 Pressure Distribution

The computational results for pressure (in terms of the coefficient of pressure,  $C_p$ ) on the wing surface for the outer 25% of the wing span and for cases of  $\alpha = 4^\circ$ ,  $8^\circ$ , and  $12^\circ$  are given in Figures 5.4, 5.5, and 5.6, respectively. The corresponding experimental results obtained by McAlister and Takahashi [1991] are also included in the figures for comparison purposes. The freestream flow conditions are:  $M_\infty = 0.17$  and  $Re = 2.0 \times 10^6$ .

As discussed in Section 5.2.1, the experiment was conducted in the NASA Ames 7- by 10-Foot Subsonic Wind Tunnel No. 2. Due to the presence of the wind tunnel walls, pressure measurements are altered from their free-air values because of blockage and distortion of the streamlines. In a closed test section,

blockage has the effect of producing a more dense flow and a higher velocity in the region where the wing is located (see McAlister and Takahashi [1991]). The nondimensional pressure coefficients are based on the “freestream” static and dynamic pressures that are obtained from a pitot-static probe placed upstream in the test section. By taking into account the blockage effects, the corrected pressure coefficient is given as

$$C_p = \frac{p - (p_{\infty u} + \Delta p_{\infty})}{q_{\infty u} + \Delta q_{\infty}} \quad (5.1)$$

where the subscript  $u$  denotes an uncorrected value and the symbol  $\Delta$  stands for the difference between corrected and uncorrected values. The corrected freestream velocity, which is more representative of the constricted flow in the test section where the wing is actually positioned, is given by

$$V_{\infty} = (1 + \varepsilon)V_{\infty u} \quad (5.2)$$

where  $V_{\infty u}$  is the “freestream” velocity at an upstream location that is not influenced by the wing (measured with an upstream pitot-static probe) and  $\varepsilon$  represents the increase of velocity due to blockage effects.

By assuming constant density of flow due to the low Mach number and using the approximation  $(1 + \varepsilon)^{-2} \approx (1 - 2\varepsilon)$ , Equation (5.1) can be simplified as

$$C_p = C_{p u}(1 - 2\varepsilon) + 2\varepsilon \quad (5.3)$$

where  $C_{p u}$  is the pressure coefficient that would be formed using upstream reference values ( $p_{\infty u}$  and  $q_{\infty u}$ ), without regard for blockage effects.

Since computations were carried out based on “free-air” formulations, the wall correction procedures proposed by McAlister and Takahashi as described above are applied to the experimental data for consistent comparisons. It is observed in Figures 5.4, 5.5, and 5.6 that the computational results compare very well with the experimental data except at the region near the leading edge and at the trailing edge region near the wing-tip. The computations did not capture the sharp leading edge suction peak and the vortex induced low pressure peak near the trailing edge at the wing-tip region too well, especially for the higher angle-of-attack case, due to the computer memory constraint. Results can be improved by clustering more grid points in these regions.

It is also noticed that near the wing-tip, tip vortex is formed on the upper surface of the wing. This tip vortex, which is reported by McAlister and Takahashi [1991] as well as Spivey [1968], Yip and Shubert [1976], and Chow et al [1993], are captured quite well in the computations. A single vortex induced low pressure peak is observed near the trailing edge of the upper surface for the rounded wing-tip configuration. Multiple pressure peaks have been reported for squared wing-tip configurations (see, for example, Spivey [1968], and McAlister and Takahashi [1991]). The formation of the tip vortex is clearly shown in Figure 5.7 in terms of the pressure contours and Figure 5.8 in terms of the velocity vectors. Low pressure is observed at the vortex core due to the high rotational velocity. Figure 5.8 also shows the highly three dimensional nature of the flow near the wing-tip.

Further inboard of the wing span, the flow remains very much two-dimensional for most of the wing span. As illustrated in Figure 5.9, the  $C_p$

distributions for the inboard 60% of the wing span are very similar. This is also observed by McAlister and Takahashi [1991] though no experimental data are available for comparison.

Figure 5.10 shows the stagnation pressure coefficient contours across the trailing vortex for various axial stations downstream of the trailing edge. Notice that the trailing edge is at  $x/c = 1$ . The low stagnation pressure vortex core is clearly seen in the figure. It is observed that as the trailing vortex moves downstream, the vortex core size increases.

#### 5.2.4 Forces and Moment

The computed coefficients of lift, drag and pitching moment (about the wing quarter-chord) for  $\alpha = 4^\circ$ ,  $8^\circ$ , and  $12^\circ$ ,  $M_\infty = 0.17$  and  $Re = 2.0 \times 10^6$  are compared with the experimental data of McAlister and Takahashi [1991] in Figure 5.11.

As discussed in Section 5.2.3 and in McAlister and Takahashi [1991], the presence of the wind-tunnel walls changes the flowfield around the wing. A change in streamline curvature (caused by the airfoil images due to the presence of the wind-tunnel walls) has the effect of imparting greater “apparent” camber to the airfoil and inducing a higher angle of attack (or an increase in the effective airfoil incidence). In order to have consistent comparisons with the computed results, the lift coefficients obtained in the experiments were corrected for wall effects as recommended by McAlister and Takahashi [1991]. For the present experimental setup, a  $0.51^\circ$  correction in the angle of attack is required for the

case of  $\alpha = 12^\circ$ . Effects of the wall on the coefficients of drag and pitching moments are deemed to be small; thus, no wall corrections are made.

Overall, the computed coefficients of lift and pitching moment compare favorably with the experimental results. Drag coefficients, however, are over predicted by the computations.

### 5.2.5 Vortex Strength

Figure 5.12 shows the streamwise distribution of the normalized total circulation for the case of  $\alpha = 12^\circ$ ,  $M_\infty = 0.17$  and  $Re = 2.0 \times 10^6$ . The vortex strength or the total circulation is defined as

$$\Gamma = \oint_s \vec{V} \cdot d\vec{s} \quad (5.4)$$

where  $\vec{V}$  is the velocity vector,  $d\vec{s}$  is the vector element of length along the path of integration, and  $s$  is the path along which the line integral is taken. Notice that  $\Gamma$  is normalized by  $cV_\infty/2$ , where  $c$  is the wing chord and  $V_\infty$  is the freestream velocity, so that direct comparison with the section lift coefficient at the mid-span of the wing can be made.

According to the inviscid analysis, the strength (at either subsonic or supersonic speeds) of one of the trailing rolled-up vortices at stations far behind the wing is equal to the sum of the strengths of all the vortices shed from one-half of the wing, and, hence, it is equal to the magnitude of the circulation around the wing in the plane of symmetry (see Spreiter and Sacks [1951]). Thus, the normalized total circulation at stations far behind the wing is equal to the section lift coefficient in the plane of symmetry.

For stations immediately downstream of the trailing edge of the wing, the trailing vortices are not fully rolled-up and much of the vortex strength of the vortex system resides in the vortex sheet. As the vortex system moves farther downstream, the vortex sheet finally rolls up completely into the trailing vortices (see Spreiter and Sacks [1951]).

The computed normalized total circulation is compared with the result of the inviscid analysis in Figure 5.12. Notice that the path of integration for the circulation calculation was chosen to enclose the trailing vortex but exclude the vortex sheet as much as possible so that the rolling-up process of the vortex sheet can be captured. It is observed in Figure 5.12 that the normalized total circulation reaches a peak value at some station aft of the trailing edge (at which the vortex sheet has completely rolled-up) and then reduces its strength slightly until an asymptotic value is reached farther downstream. This asymptotic value is found to be about 85% of the theoretical value predicted in the inviscid analysis. The reduction in the circulation strength could be due to viscous dissipation as was also observed in the experimental studies of Higuchi et al [1986].

The comparison of the computed normalized downwash distribution downstream of the trailing edge with the theoretical analysis of Spreiter and Sacks [1951] for the case of  $\alpha = 12^\circ$ ,  $M_\infty = 0.17$  and  $Re = 2.0 \times 10^6$  is shown in Figure 5.13. Notice that the downwash  $w$  is normalized by  $V_\infty C_L b / \pi AR b'$  (where  $C_L$  is the lift coefficient of the wing,  $b$  is the full-span of the wing,  $AR$  is the aspect ratio of the wing, and  $b'$  is the distance between the trailing vortices) as used by Spreiter and Sacks [1951]. Since the distance between the trailing

vortices decreases as they move downstream, the spanwise distance,  $y$ , from the plane of symmetry of the wing at various downstream stations is normalized by  $b'/2$ .

The inviscid analysis of Spreiter and Sacks [1951] assumed that the core size of the trailing vortices remained unchanged (i.e., the vortex core did not grow in size) and that the circulation strength remained constant; hence, a universal curve for the normalized downwash distribution for stations far downstream from the wing was obtained. In the present viscous computations, it is observed that although the circulation strength remains constant at various streamwise stations farther downstream from the wing, the maximum magnitude of the downwash (or upwash depending on whether it is inboard or outboard of the trailing vortices) decreases as the trailing vortices travel downstream because the size of the vortex core increases due to the entrainment of the surrounding fluid into the viscous vortex core.

## 5.3 Axial Wing-Tip Blowing Cases

### 5.3.1 Configuration

The same configuration described in Section 5.2.1 for the no blowing cases is used for the axial wing-tip blowing cases. In addition, a jet slot is created as shown in Figure 5.14. The jet slot has a length of 11.2% of the wing chord and a width of 1.5% of the wing chord. Due to the presence of the jet slot, a small step of height 1.5% of the wing chord is created on the wing surface. As discussed in Section 4.3 the actuator plane concept is employed in the

computations to model this jet slot. The intensity of the axial wing-tip blowing is controlled by changing the jet plenum supply pressure.

Results presented here are for  $\alpha = 8^\circ$ ,  $M_\infty = 0.17$  and  $Re = 2 \times 10^6$ . The blowing intensity varies from  $C_\mu = 0.0000$  to  $0.0047$ . The highest blowing intensity gives a jet exit velocity closed to sonic condition. Results presented are also for jet slot located at the 90%-chord of the wing. Computations were performed for jet slot located farther upstream as well; however, it was observed that less penetration into the flowfield was achieved as the wall jet had to overcome additional wing surface area. They are therefore not presented.

### 5.3.2 General Flow Features

Figure 5.15 shows the closed-up views of the velocity vectors in the wing-tip region for cases with the axial wing-tip blowing off and on. Without blowing, a typical turbulent boundary layer velocity profile is observed in Figure 5.15 (a). By turning the blowing on, the presence of the jet transforms the boundary layer profile into a wall jet profile (see Figure 5.15 (b)). It is observed that consistent with experimental observations the velocity profiles upstream of the jet slot are not affected by the presence of the jet. This consistency is possible since the actuator plane concept models the jet as a one-sided source of mass, momentum and energy.

Figure 5.16 shows the effect of axial wing-tip blowing on the flowfield downstream of the trailing edge of the wing. As shown in Figure 5.16 (b), the high velocity jet penetrates into the vortex core of the trailing vortex for some downstream distance before the effect of the blowing diminishes. It is also

observed that due to the rolling-up process of the vortex sheet, the jet re-aligns itself into the freestream direction together with the trailing vortex.

### 5.3.3 Vortex Strength

Figure 5.17 shows the variation of the streamwise distribution of the normalized total circulation with the blowing momentum coefficient. As discussed in Section 5.2.5 for the case with blowing off, the normalized total circulation reaches a peak value at some station aft of the trailing edge (at which the vortex sheet has completely rolled-up) and then reduces its strength slightly until an asymptotic value is reached farther downstream. With blowing on, the same phenomenon is observed except that now it takes longer for the circulation to reach a peak value, i.e., it takes longer for the vortex sheet to roll up completely. As the blowing intensity increases, the rolling-up process is delayed further. The delay in the rolling-up process due to blowing can be seen more clearly by the particle traces in Figure 5.18. It is shown in Figure 5.18 (a) that without blowing the tip vortex starts to roll up even before it reaches the trailing edge of the wing. With blowing turned on in Figure 5.18 (b), the momentum of the jet delays the rolling-up of the vortex sheet.

It is also observed in Figure 5.17 that the total circulation strength of the trailing vortex increases slightly for stations farther downstream of the wing as the blowing intensity increases. This is due to the fact that the axial wing-tip blowing increases the lift on the wing slightly (to be discussed in Section 5.3.4); and that the higher the wing lift, the stronger the circulation of the trailing vortex.

Figures 5.19 and 5.20 show the downwash distribution at various axial stations downstream of the trailing edge for cases with blowing off and on, respectively. For stations immediately downstream of the trailing edge, the downwash differs slightly for cases with blowing off and on. However, the downwash distribution for the case with blowing on is quite similar to that with blowing off for stations farther downstream of the wing except that the former has a slightly higher value due to the stronger circulation strength discussed earlier.

Since the circulation strength of the trailing vortex is an overall feature of the wing loading, the axial wing-tip blowing, although possibly able to change the behavior of the local flowfield, is unable to alter the flowfield features farther downstream. It was also observed in the experimental study of Snedeker [1972] that the axial wing-tip blowing, although it altered the near-field velocity distribution, did not reduce the rolling moment imposed on an object farther downstream. Dunham [1976] classified the axial wing-tip blowing as an unsuccessful concept for aircraft wake vortex minimization.

#### **5.3.4 Forces and Moment**

Figure 5.21 shows the effects of axial wing-tip blowing on the overall performance of the wing in terms of lift, drag and pitching moment (about the wing quarter-chord). It is observed that as the blowing intensity increases the lift on the wing increases. This is due to the fact that the high velocity jet entrains the surrounding fluid on the upper surface of the wing. This creates a low pressure region in the vicinity of the jet (see Figure 5.22) and increases the lift on the wing.

Since the jet slot is located near the trailing edge of the wing, this low pressure region also increases the pressure drag on the wing and results in higher overall drag. Similarly, the low pressure region also creates a pitching down moment on the wing. Thus, the overall pitching moment (taken as positive for pitching up moment) decreases as the blowing intensity increases.

## 5.4 Spanwise Wing-Tip Blowing Cases

### 5.4.1 Configuration

The configuration used in the experiments of Tavella et al [1985, 1988] and Lee et al [1989] (see Figure 5.23) is used in the present computational study with spanwise wing-tip blowing. The experiments were conducted in the Stanford low-speed wind-tunnel which had a 45.7 cm x 45.7 cm test section and a freestream velocity of 40 m/s, giving a chord-based Reynolds number of  $4 \times 10^5$ . A semi-span rectangular wing with a constant and untwisted NACA 0018 symmetric airfoil profile along the entire span was used. The wing-tip is rounded and the (full-span) aspect ratio of the wing is 3.28.

A jet slot with a thickness of 0.16 cm was positioned in the plane of symmetry of the wing-tip, extended over 73.3% of the chord and oriented such that the jet exited in the spanwise direction. The jet blowing intensity was controlled by the jet supply plenum pressure and varied from  $C_\mu = 0.0000$  to 0.2236.

### 5.4.2 General Flow Features

Figure 5.24 shows the close-up views of the velocity vectors at 10% chord downstream of the wing trailing edge for cases with spanwise wing-tip blowing off and on, and  $\alpha = 8^\circ$ . Figure 5.24 (a) shows clearly the formation of the trailing vortex at the wing-tip region. With moderately low blowing intensity, Figure 5.24 (b) shows that the trailing vortex is displaced not just outwards but also upwards. This is also observed in the experiment of Lee et al [1989].

Figure 5.25 shows a sequence of velocity vectors at the 90%-chord for  $\alpha = 2^\circ$  with increasing blowing intensity. It is observed, especially in Figures 5.25 (c) and (d), that in addition to the primary vortex, a secondary vortex rotating in the opposite direction of the primary vortex is formed at higher blowing intensities. The jet blowing becomes dominant and a typically free jet velocity profile is seen. This is also observed in the experiment of Lee et al [1989].

### 5.4.3 Forces and Moment

Figure 5.26 shows the variations of the coefficients of lift, drag, pitching moment (about the wing quarter-chord) and  $L/D$  with the blowing momentum coefficient for  $\alpha = 2^\circ, 4^\circ, 6^\circ$  and  $8^\circ$ . It is observed in Figure 5.26 (a) that as the spanwise wing-tip blowing intensity increases, lift on the wing increases. The nonlinearity of the lift coefficient with the blowing momentum coefficient was also observed in the experiments (see Tavella et al [1985, 1988] and Lee et al [1989]). It is noticed that the computations predict the experimental results very well for cases of  $\alpha = 2^\circ$  and  $4^\circ$ ; whereas, over-predictions by the computations

are observed for cases of  $\alpha = 6^\circ$  and  $8^\circ$ . Figure 5.27 shows the comparison of the computational results with the experimental data for the lift coefficient for various angles-of-attack without spanwise wing-tip blowing. Notice that no wall corrections to the experimental data were made. For low angle-of-attack cases, wall blockage is small and the computational and experimental results compare favorably. However, effects of the wall blockage become prominent at higher angle-of-attack and resulting in greater discrepancies between the computational and experimental results.

Figure 5.26 (b) shows the computational results for the variation of the drag coefficient with blowing momentum coefficient. It is noticed that at moderately low blowing intensities, the drag increases. However, by increasing the blowing intensity further, the drag decreases. The drag coefficient may be lower than that without spanwise wing-tip blowing for high enough blowing intensity and lower angle-of-attack cases. It is also observed that for a particular blowing intensity, the drag increase is higher for higher angle-of-attack cases. This is clearly illustrated in Figure 5.26 (d) in which the variation of the  $L/D$  ratio with the blowing intensity is presented. It is noticed that returns on  $L/D$  via spanwise wing-tip blowing are more attractive for lower angle-of-attack cases than for higher angle-of-attack cases.

Figure 5.26 (c) shows the variation of the pitching moment (about the wing quarter-chord) with blowing intensity. It is observed that as the blowing intensity increases, the pitching-up moment on the wing decreases marginally. Since spanwise wing-tip blowing is applied on almost the entire chord, the impact

of blowing on the pitching moment on the wing tends to even out and results in marginal changes in the pitching moment.

#### 5.4.4 Vortex Strength

Figure 5.28 shows the variation of the streamwise distribution of the normalized total circulation with blowing momentum coefficient for the case of  $\alpha = 4^\circ$ . For streamwise stations immediately downstream of the wing trailing edge, the circulation integration loop basically encloses the tip vortex (or primary vortex) and excludes the secondary vortex. Since spanwise wing-tip blowing has the effect of increasing the circulation strength of the primary and secondary vortices, a rather high normalized total circulation strength immediately downstream of the trailing edge is observed in Figure 5.28. However, as the vortices move downstream, the circulation integration loop starts to enclose part of the secondary vortex which rotates in the opposite direction to that of the primary vortex. This results in a reduced circulation strength. For stations far downstream, the circulation integration loops eventually enclose both the primary and secondary vortices and an asymptotic value is reached for the vortex system. It is observed that the asymptotic circulation strength increases as the blowing intensity increases. This is intuitive since the overall lift on the wing increases as a result of spanwise wing-tip blowing, the total circulation strength for the vortex system far downstream must increase.

Figure 5.29 shows the streamwise development of the primary and secondary vortices. The formation of the primary and secondary vortices at high blowing intensity is clearly seen in Figure 5.29 (a). At the 90%-chord station, these vortices are distinctively apart.

## 5.5 Solution Accuracy

Due to the constraints of the available computer speed and computer memory, computations were performed using  $83 \times 69 \times 61$  (i.e., 349,347) grid points. These constraints prevent a grid refinement study, which uses more grid points, to be carried out. However, the computational results obtained by using  $51 \times 51 \times 41$  (i.e., 106,641) grid points are compared with the present results and the experimental data to study the effect of grid refinement on solution accuracy.

Figure 5.30 shows the comparison in terms of  $C_p$  distribution. It is observed that the leading edge suction peak can be better captured by the fine grid case as compared with the coarse grid case. The vortex induced low pressure peak near the trailing edge at the wing-tip region (see Figure 5.30 (b)) is also better captured by the fine grid case. Overall, the computational results obtained by the fine grid case have a better agreement with the experimental data as compared with those obtained by the coarse grid case.

By comparing results obtained from the coarse and fine grid cases, a simple error analysis yields an error  $\varepsilon(h) \approx [\phi(h) - \phi(\alpha h)] / (1 - \alpha^2)$ , where  $\phi$  denotes the solution and  $\alpha$  denotes the grid refinement factor. Based on the lift coefficients obtained from the coarse and fine grid cases, the fine grid case gives an error of 2.5%.

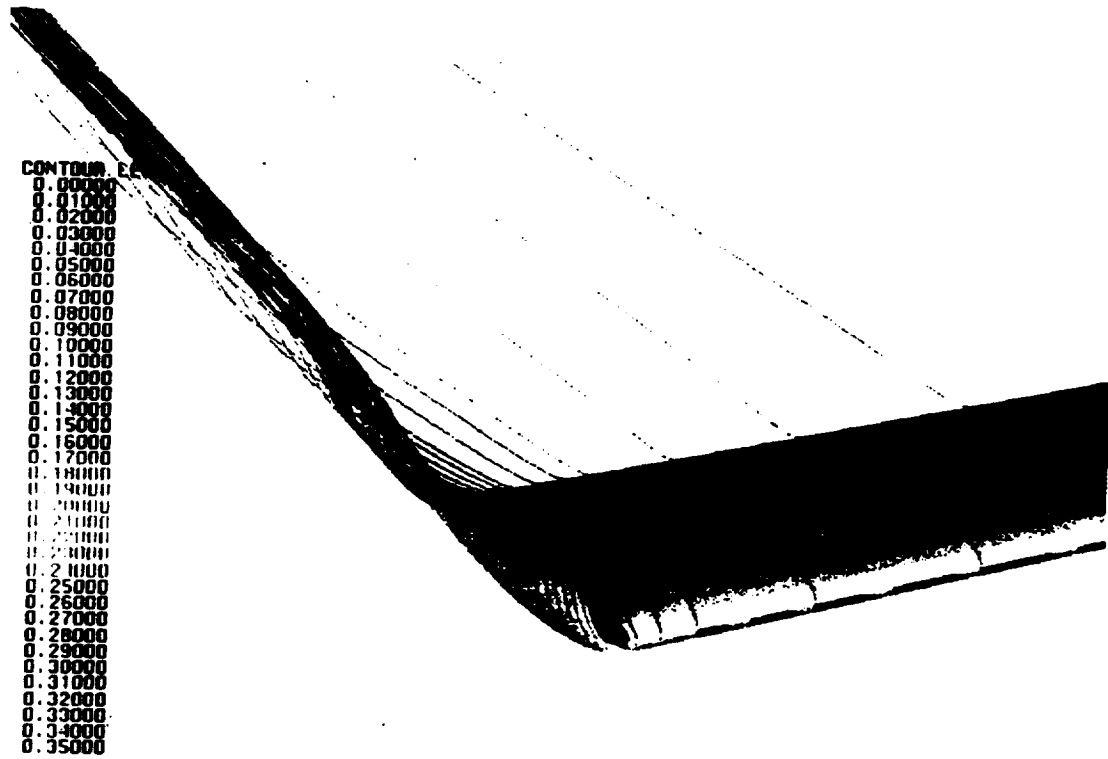
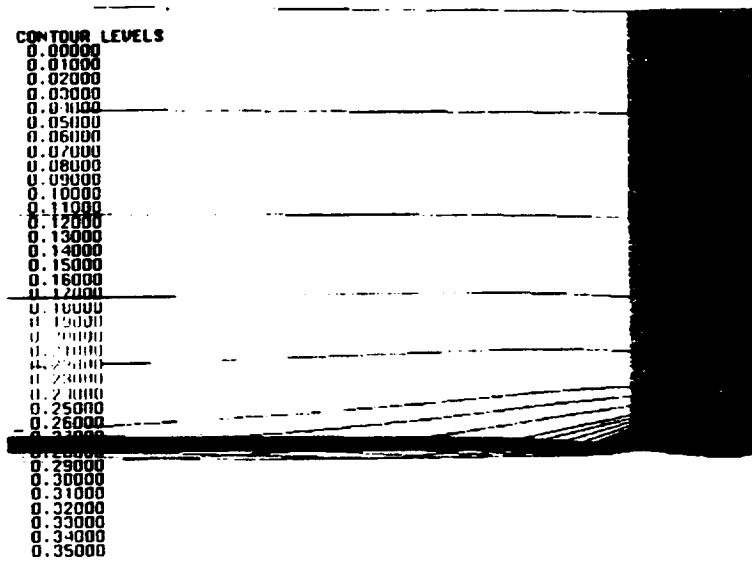


Figure 5.1: Particle traces showing the formation and roll-up of the wing-tip vortex.



(a) Side view.



(b) Plan view.

Figure 5.2: Side and plan views of the trailing vortex.

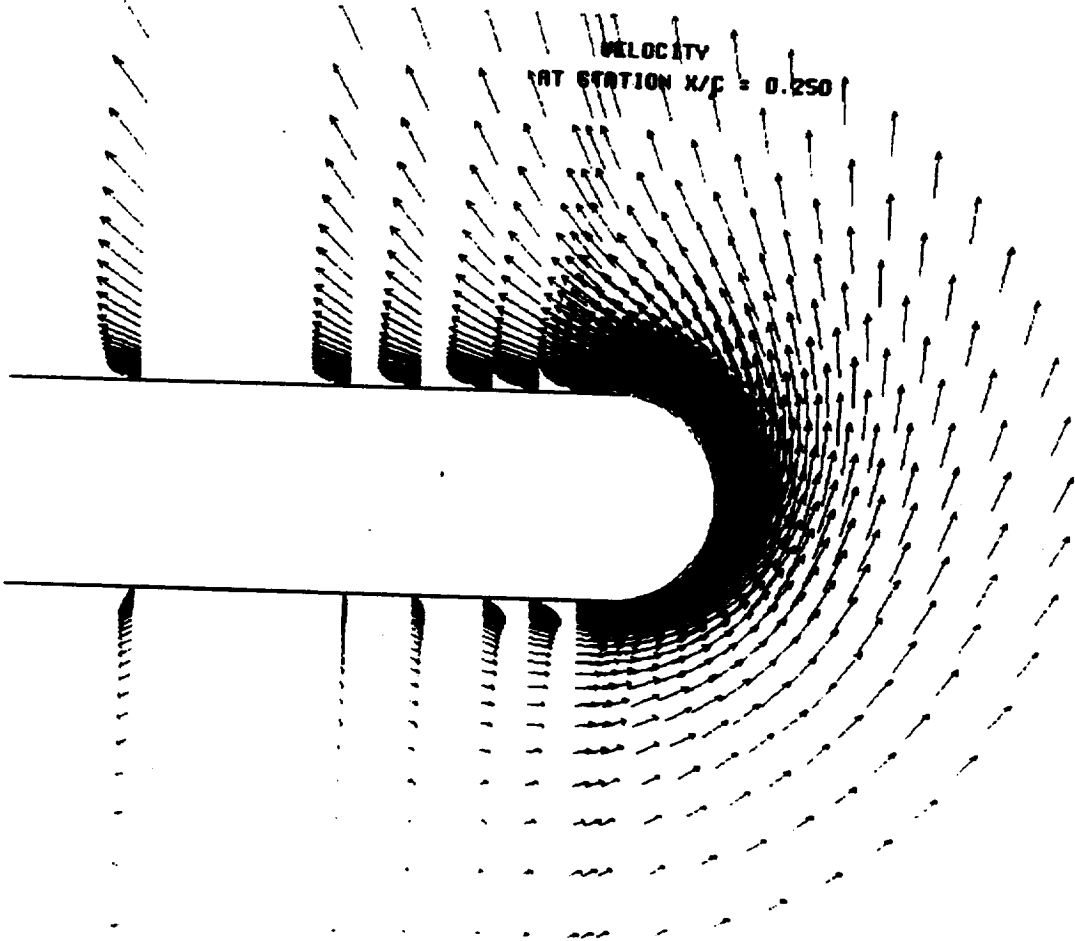


Figure 5.3: Velocity vectors at the quarter-chord showing flow from the lower surface to the upper surface of the wing near the wing-tip.

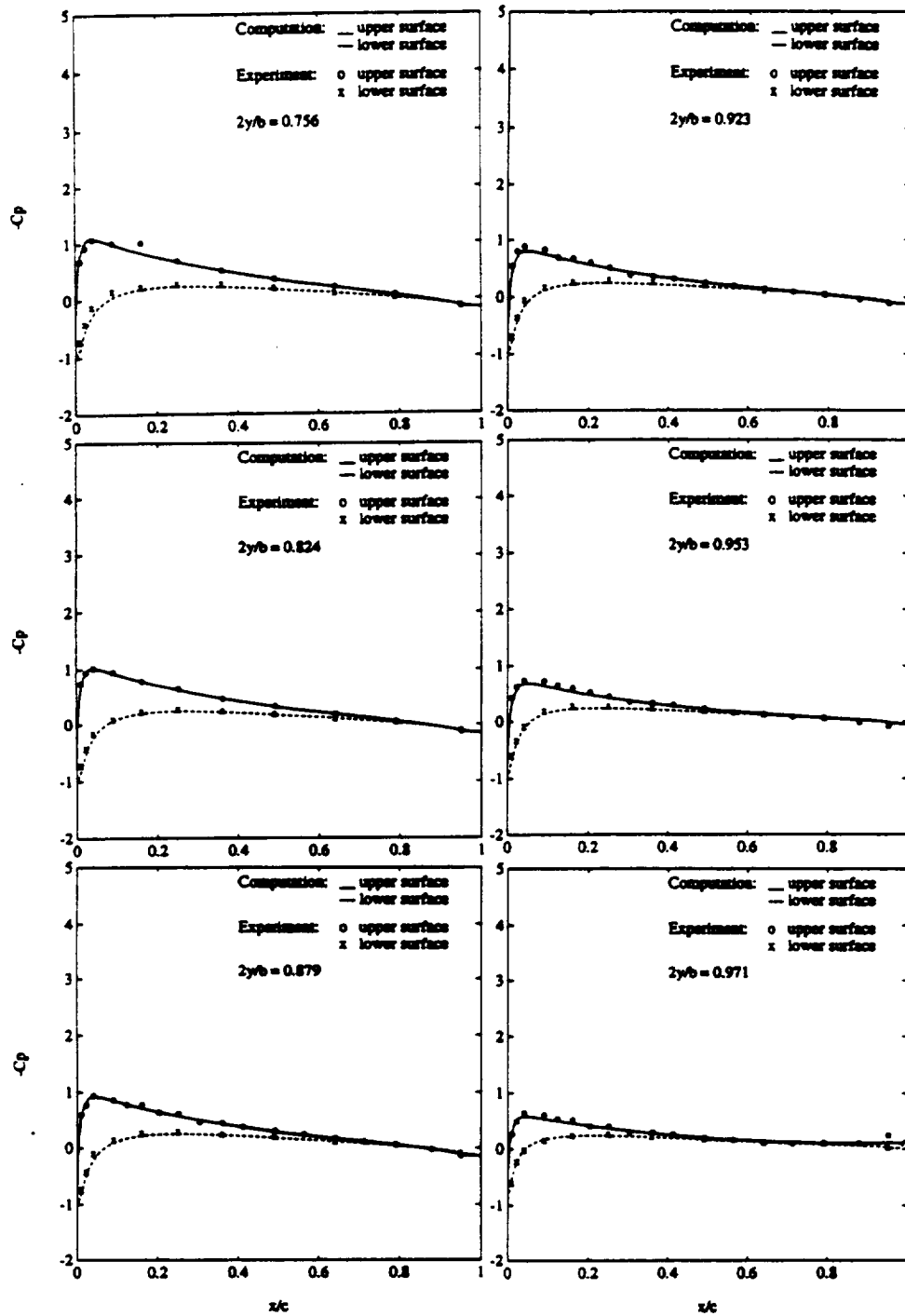


Figure 5.4: Distribution of the pressure coefficients,  $C_p$ , on the wing near the wing-tip region for the case of  $\alpha = 4^\circ$ ,  $M_\infty = 0.17$  and  $Re = 2.0 \times 10^6$ .

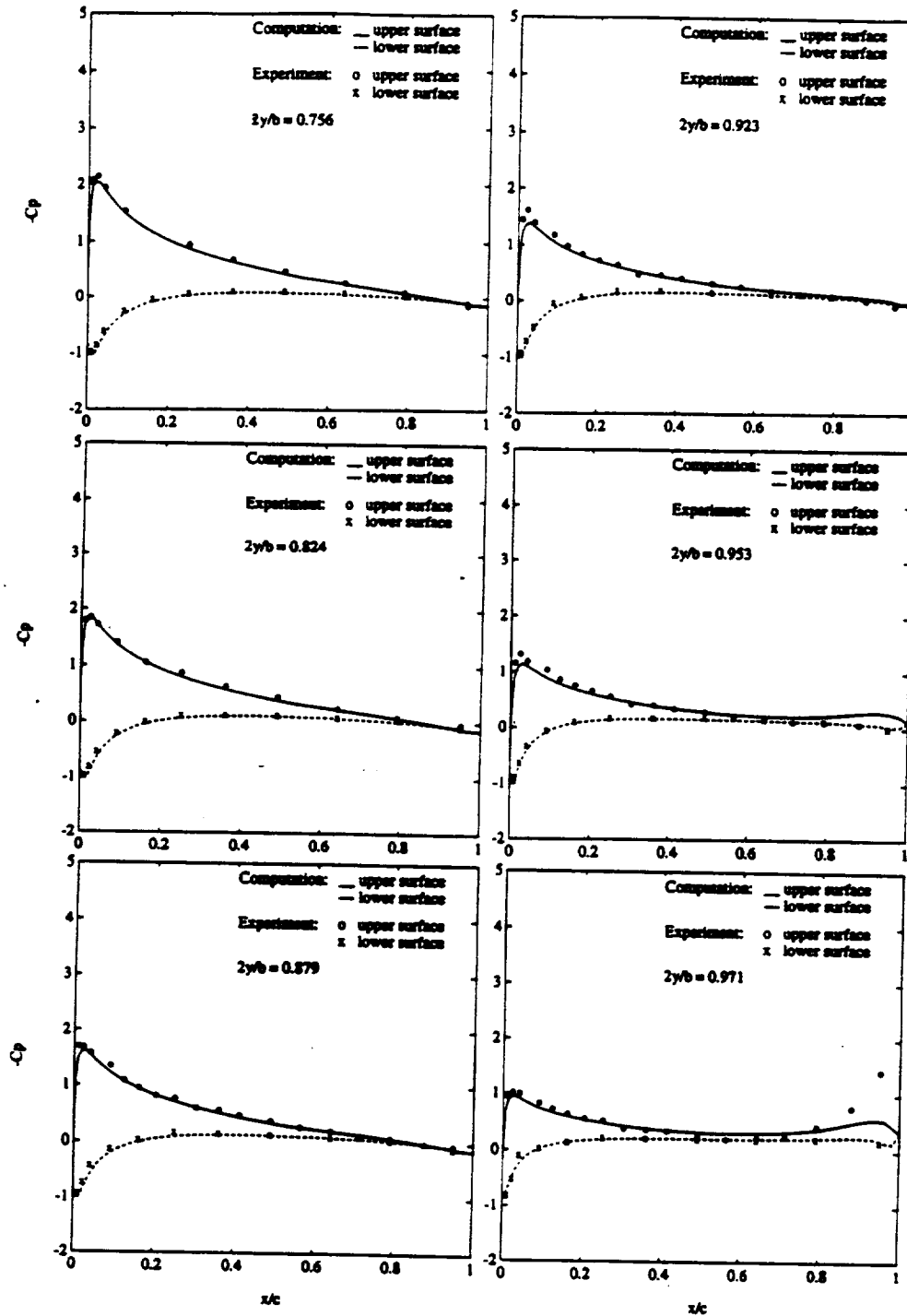


Figure 5.5: Distribution of the pressure coefficients,  $C_p$ , on the wing near the wing-tip region for the case of  $\alpha = 8^\circ$ ,  $M_\infty = 0.17$  and  $Re = 2.0 \times 10^6$ .

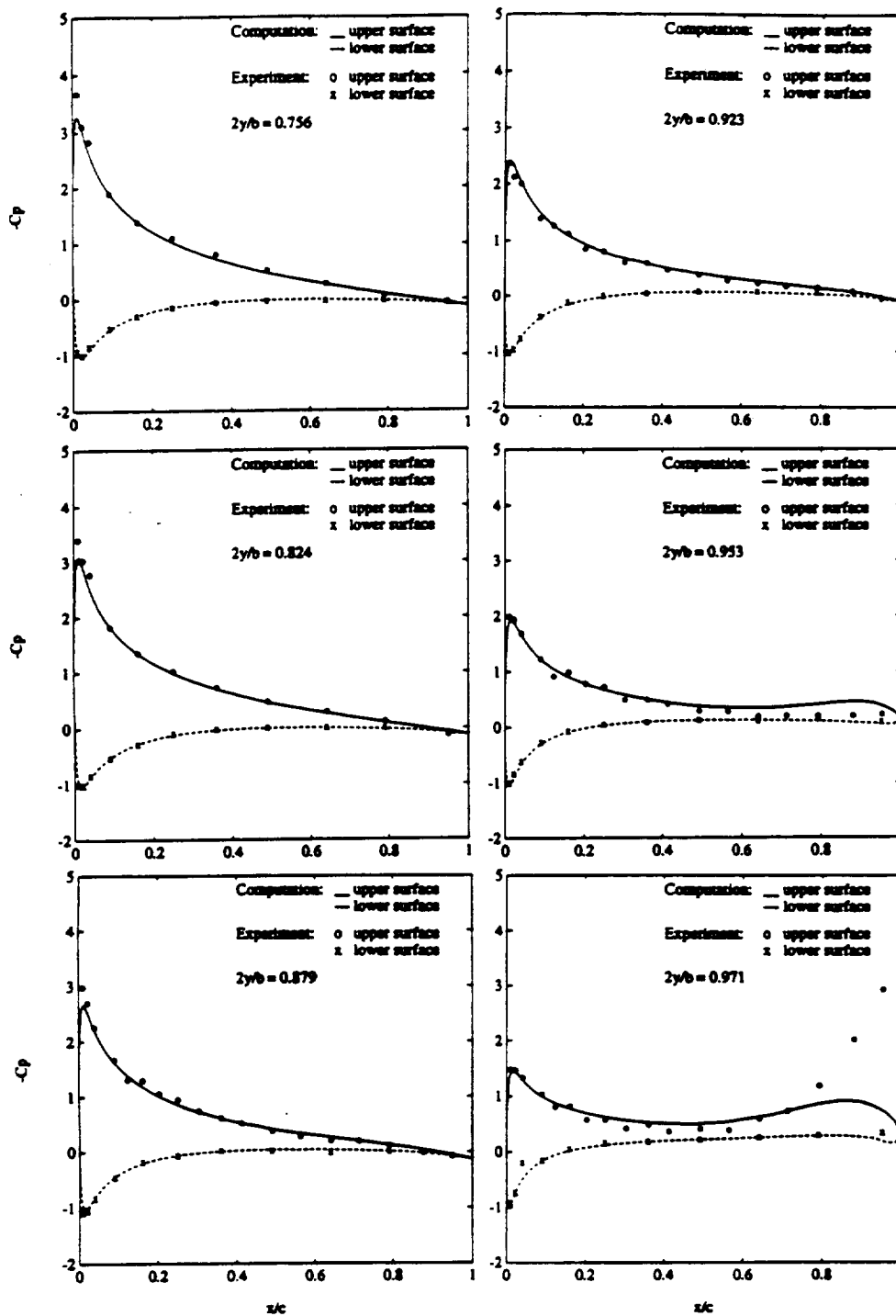


Figure 5.6: Distribution of the pressure coefficients,  $C_p$ , on the wing near the wing-tip region for the case of  $\alpha = 12^\circ$ ,  $M_\infty = 0.17$  and  $Re = 2.0 \times 10^6$ .

C-2-

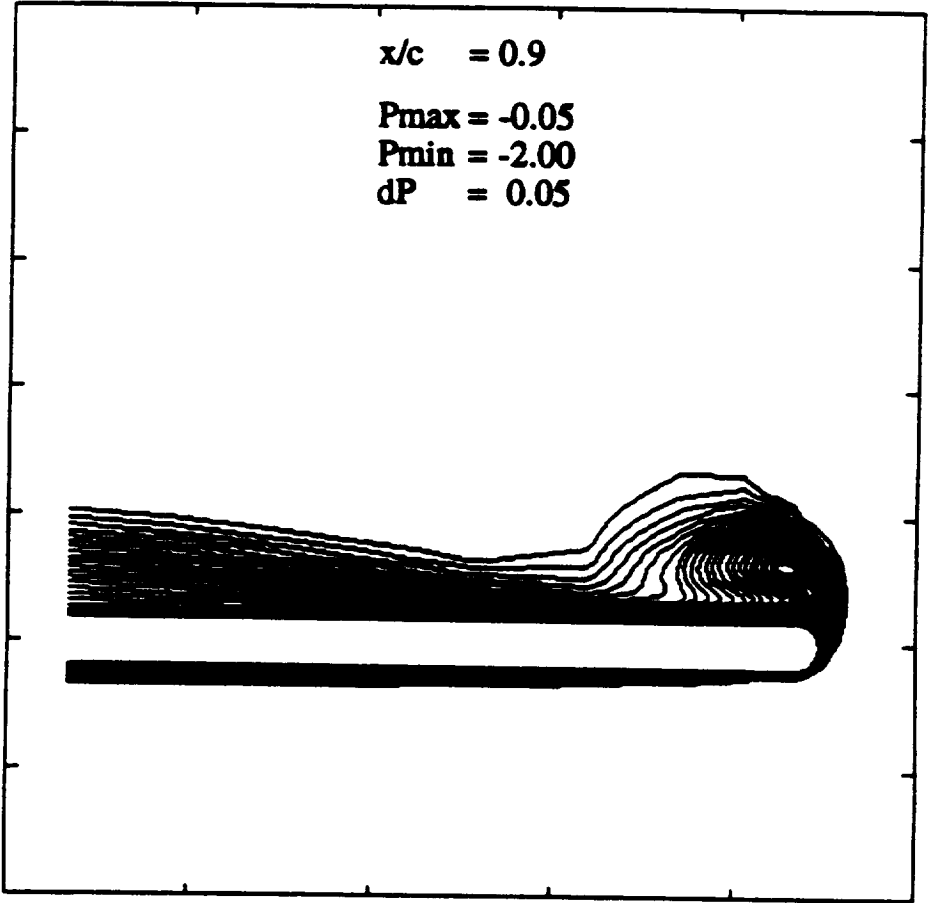


Figure 5.7: Formation of the tip vortex at  $x/c = 0.9$  depicted by the stagnation pressure coefficient contours.

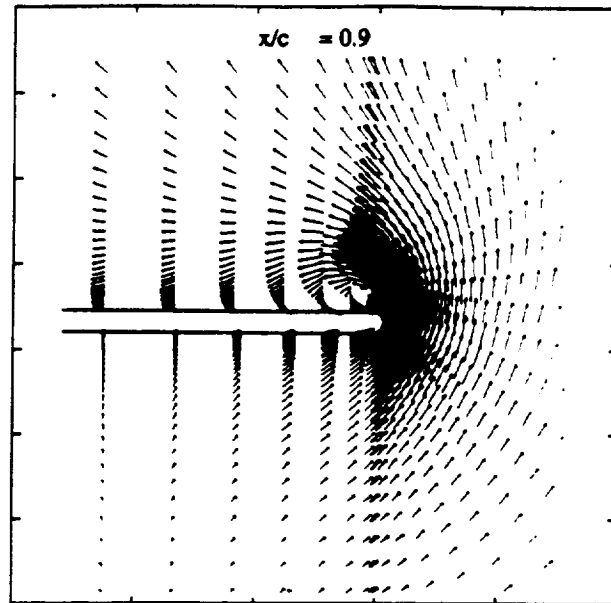
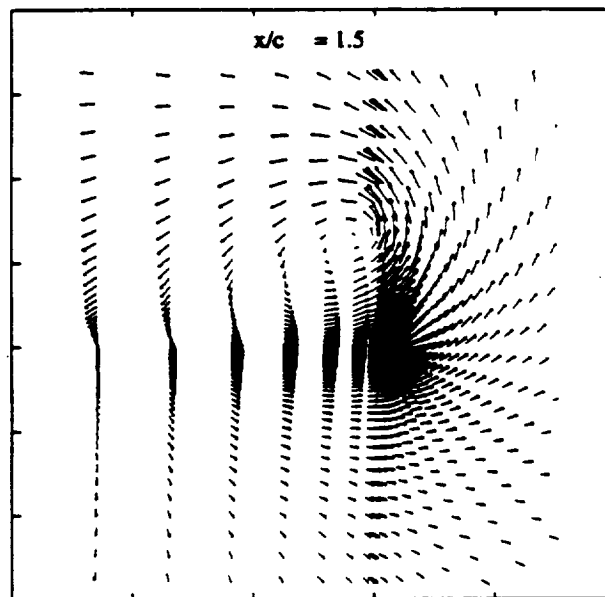
(a) At  $x/c = 0.9$ .(b) At  $x/c = 1.5$ .

Figure 5.8: Velocity vectors showing the highly three-dimensional nature of the tip vortex.

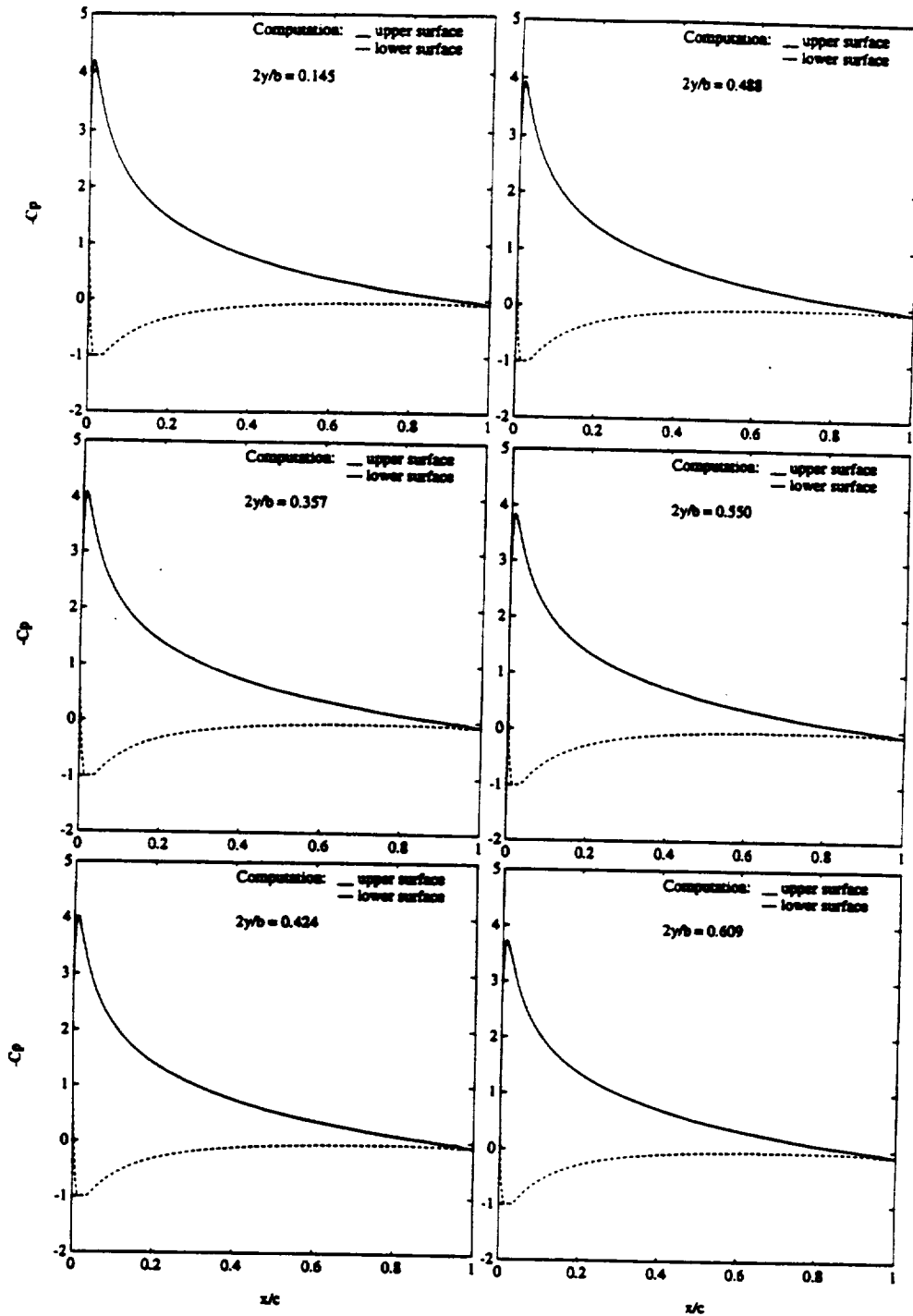


Figure 5.9:  $C_p$  distributions for the inboard 60% of the wing span showing the two-dimensional nature of the flow at the inboard region.

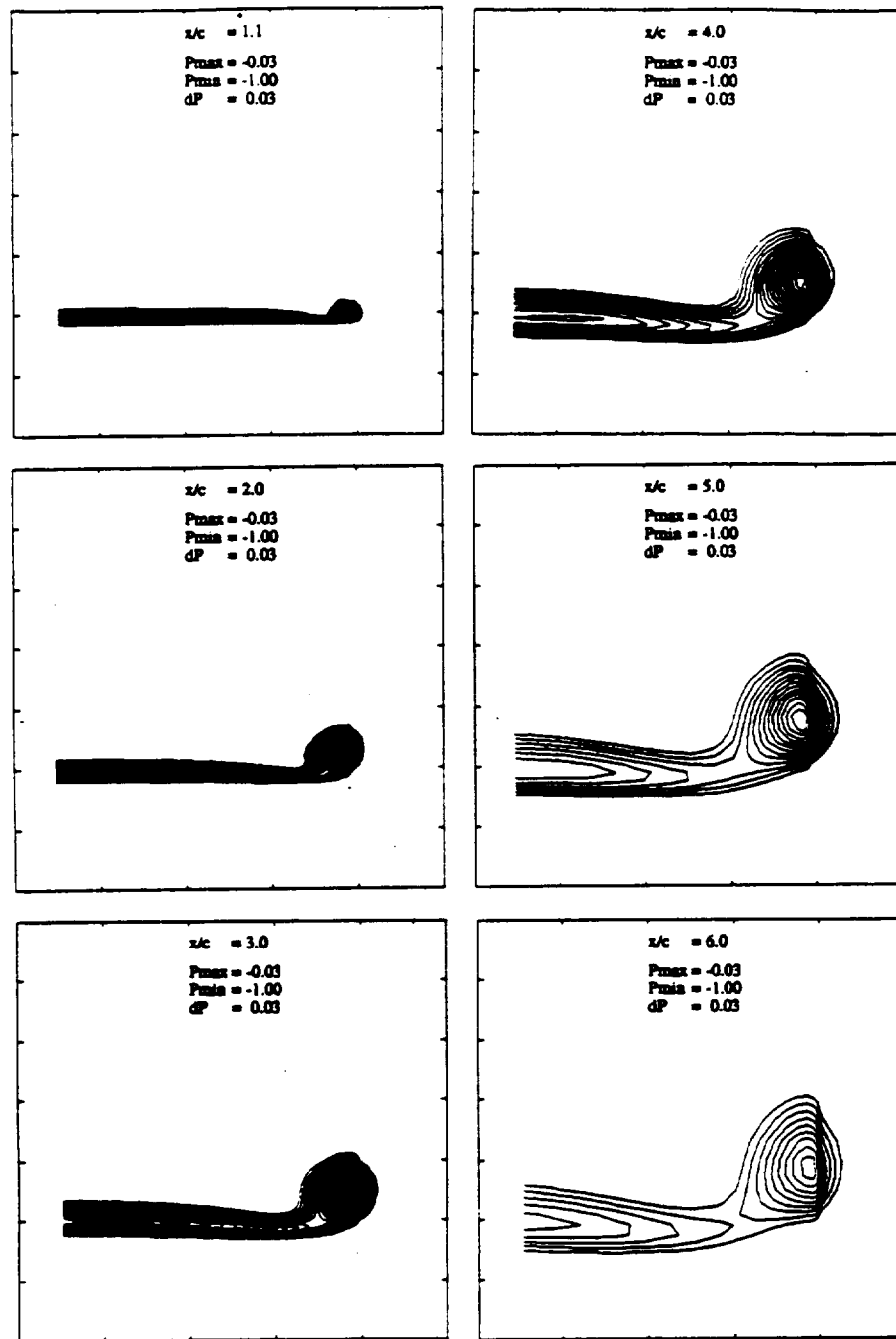


Figure 5.10: Stagnation pressure coefficient contours across the trailing vortex for various axial stations downstream of the trailing edge.

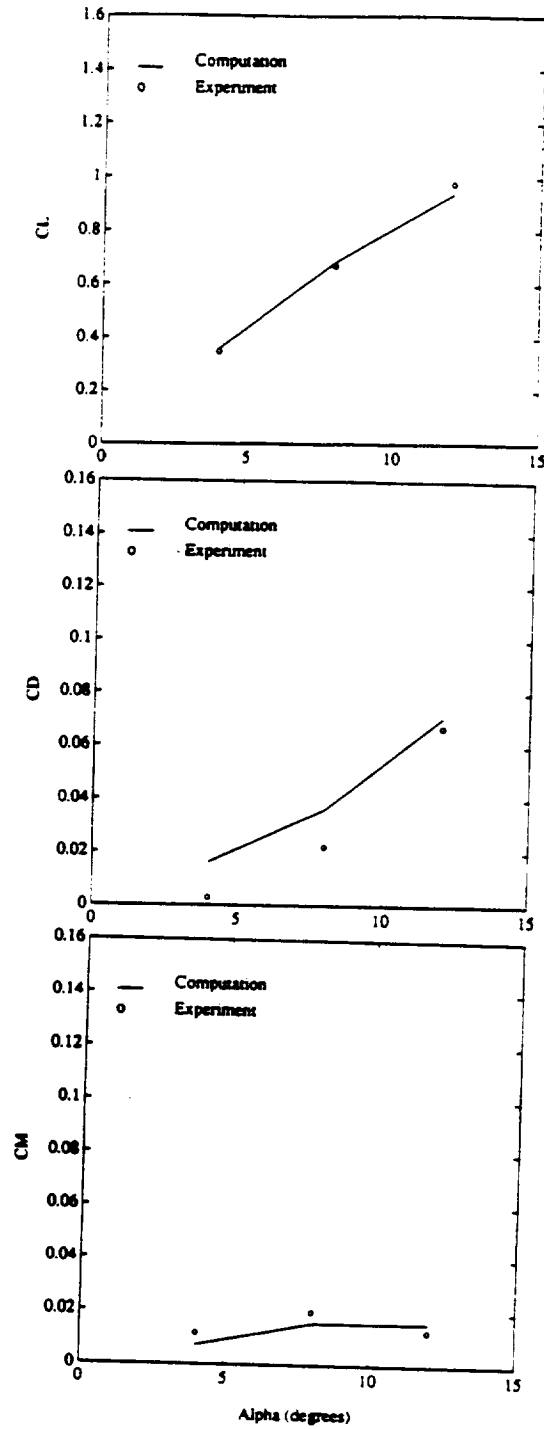


Figure 5.11: Variations of the coefficients of lift, drag and pitching moment (about the quarter-chord) for the case of  $M_\infty = 0.17$  and  $Re = 2.0 \times 10^6$ .

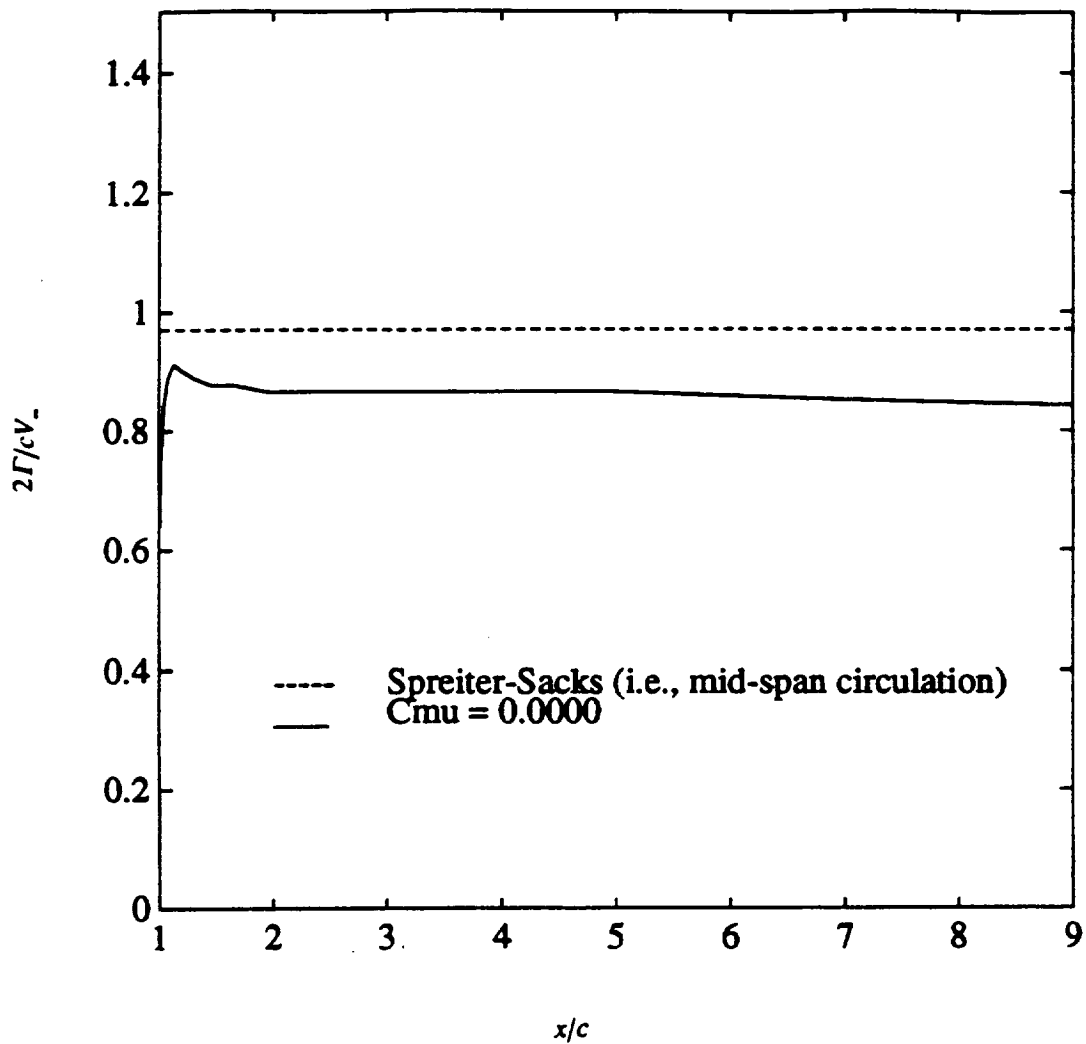


Figure 5.12: Streamwise distribution of the normalized total circulation for the case of  $\alpha = 12^\circ$ ,  $M_\infty = 0.17$  and  $Re = 2.0 \times 10^6$ .

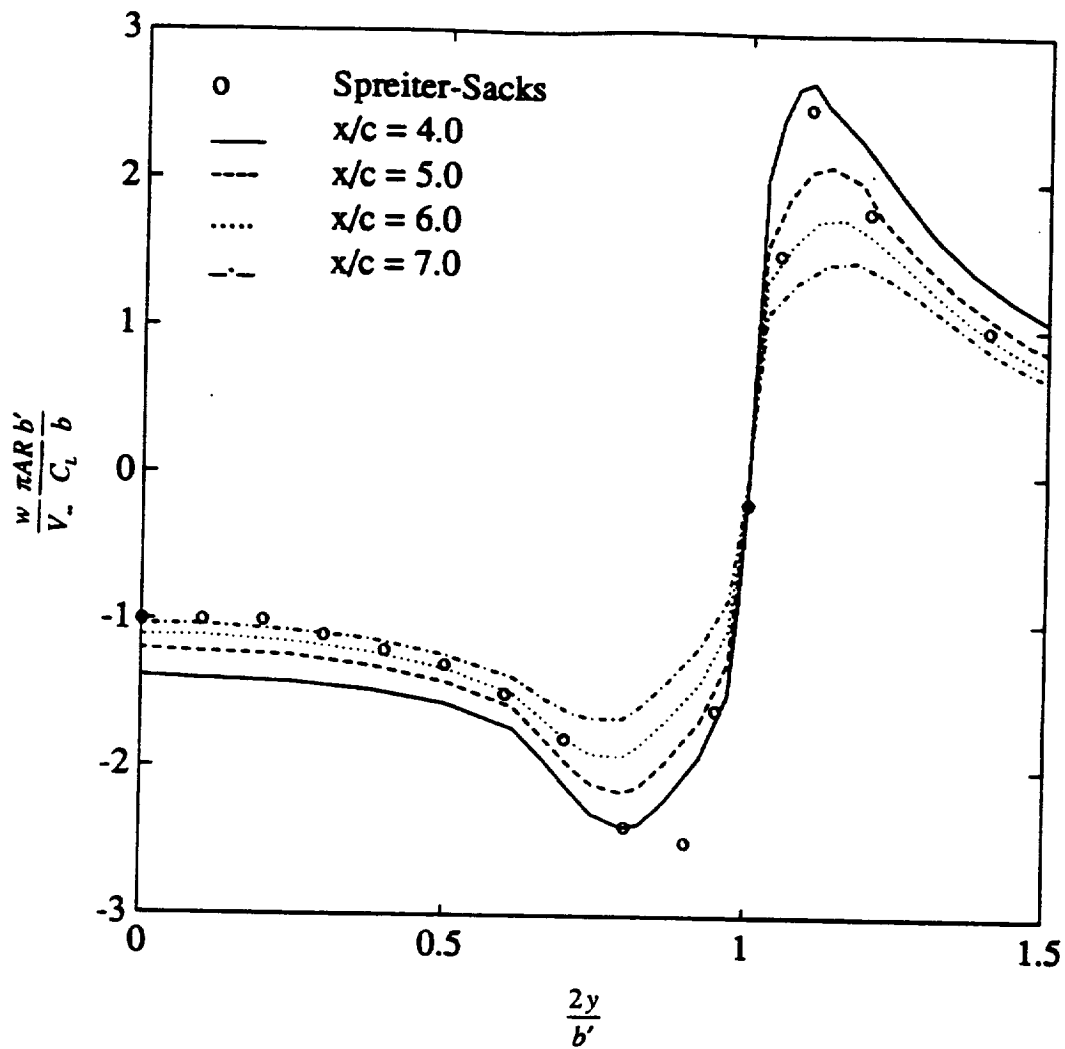


Figure 5.13: Comparison of the calculated normalized downwash distribution downstream of the trailing edge with the theoretical analysis of Spreiter-Sacks for the case of  $\alpha = 12^\circ$ ,  $M_\infty = 0.17$  and  $Re = 2.0 \times 10^6$ .

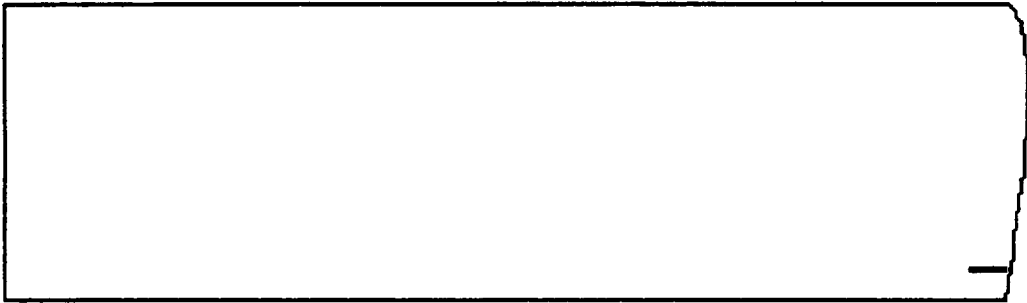
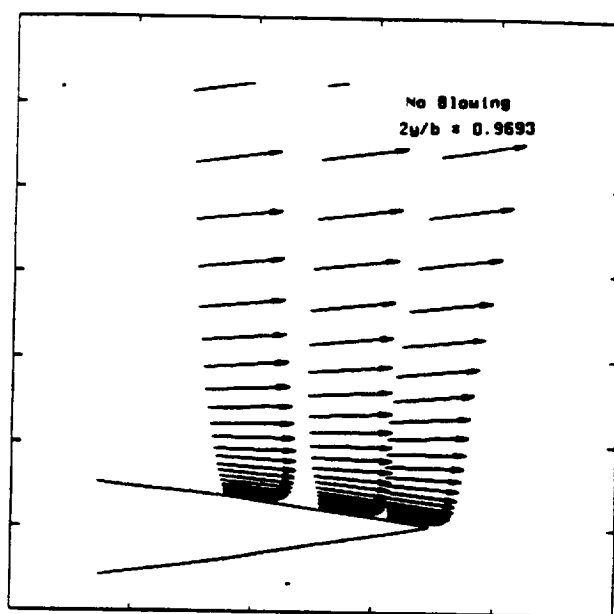
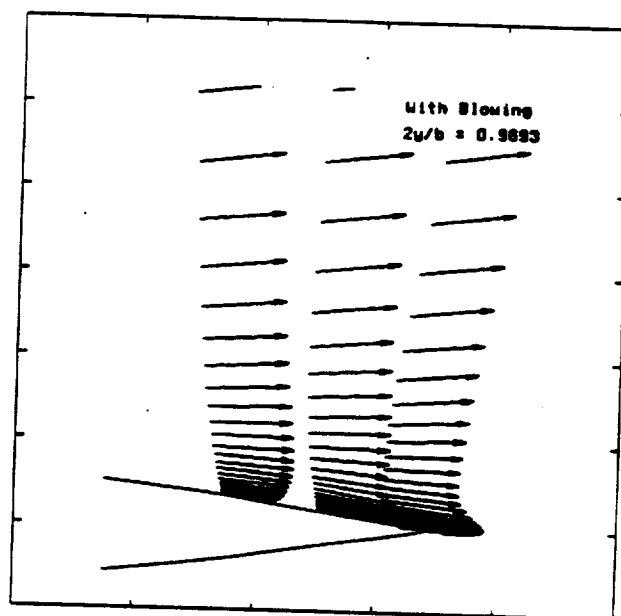


Figure 5.14: The jet slot with a jet length of 11.2% chord and a jet width of 1.5% chord is located at the 90%-chord location for the axial wing-tip blowing.

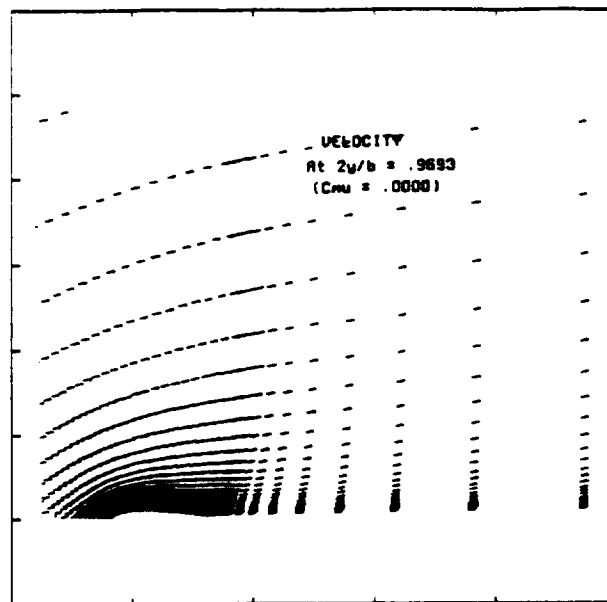


(a) Without blowing.

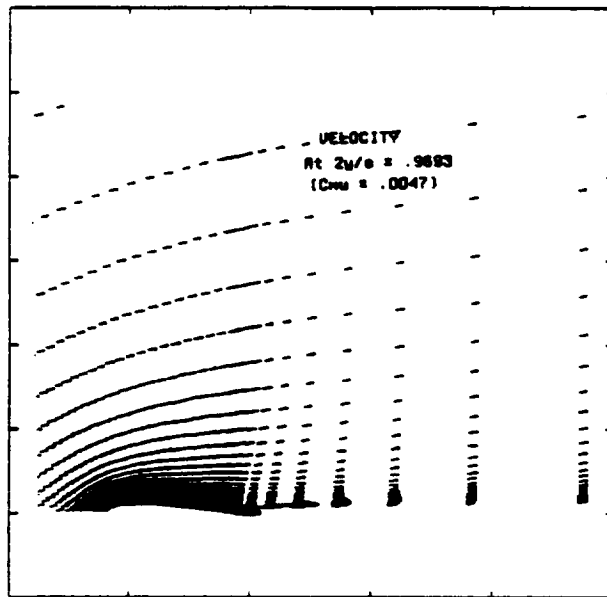


(b) With blowing.

Figure 5.15: Velocity vectors at the spanwise station  $2y/b = 0.9693$  (zoom-in).



(a) Without blowing.



(b) With blowing.

Figure 5.16: Velocity vectors at the spanwise station  $2y/b = 0.9693$ .

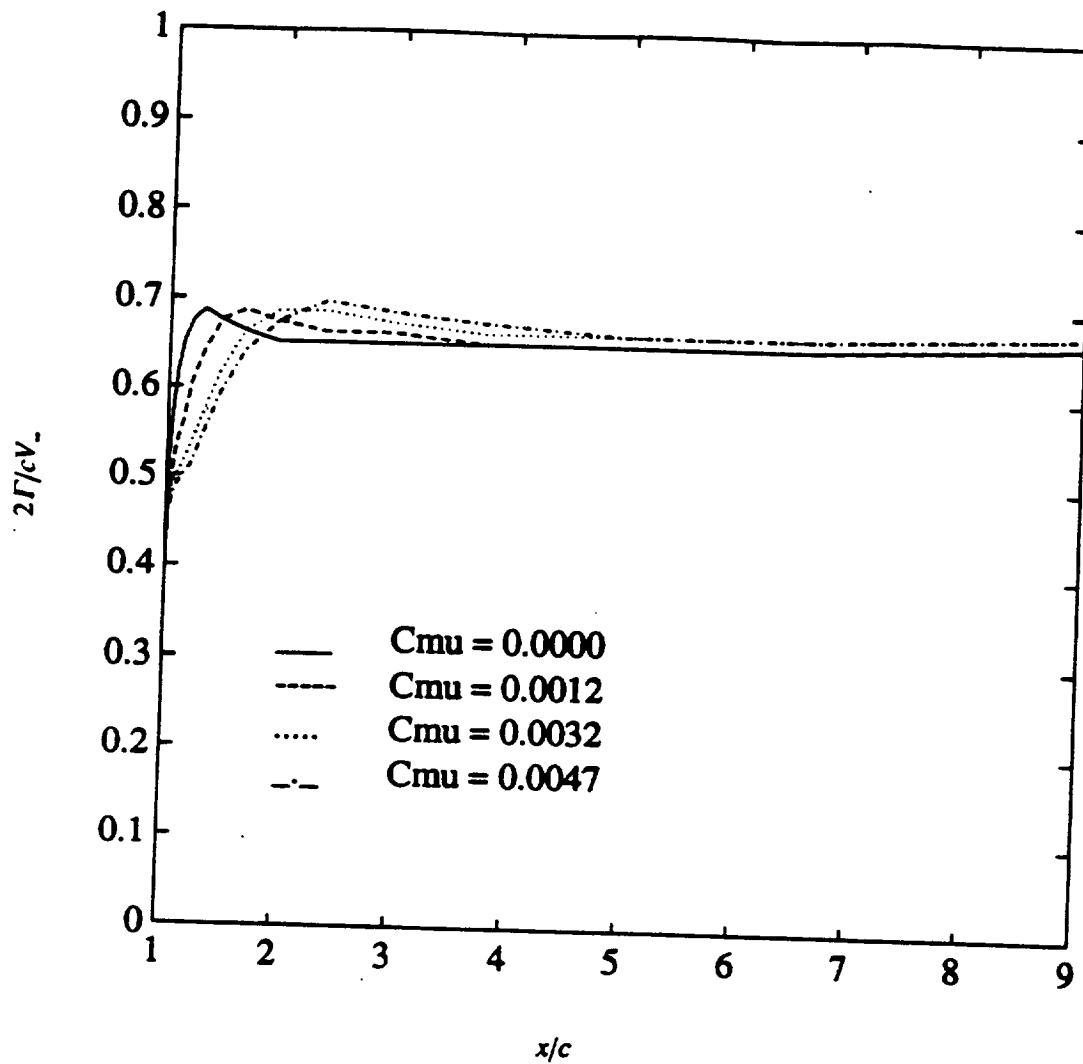
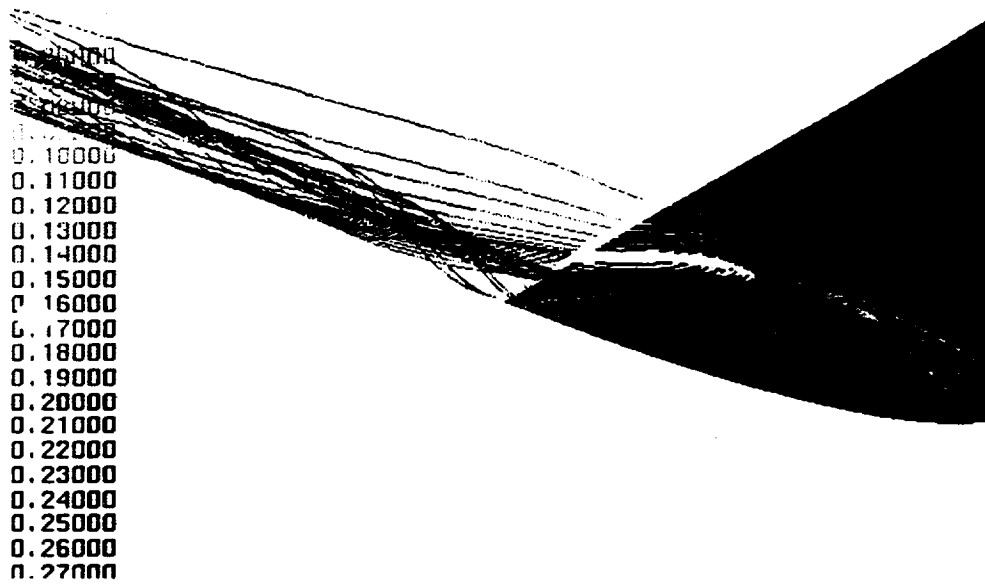
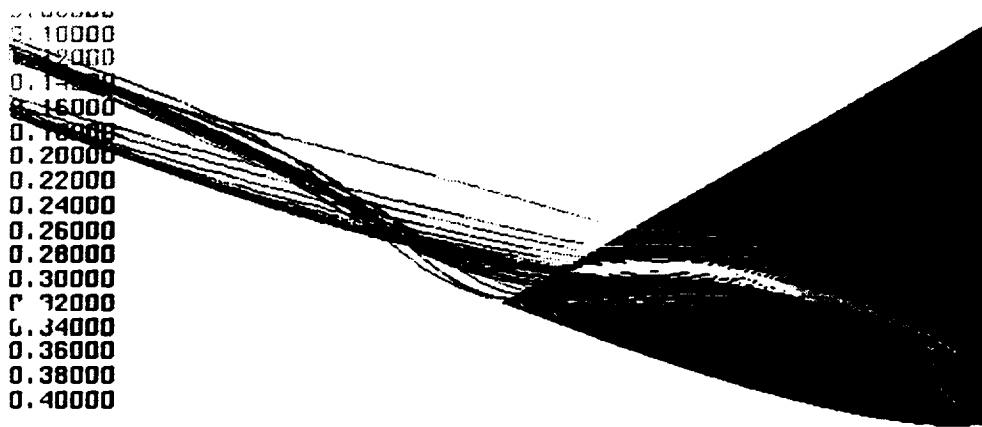


Figure 5.17: Variation of the streamwise distribution of the normalized total circulation with blowing momentum coefficient for the case of  $\alpha = 8^\circ$ ,  $M_\infty = 0.17$  and  $Re = 2.0 \times 10^6$ .



(a) Without blowing.



(b) With blowing.

Figure 5.18: Particle traces showing the rolling-up of the trailing vortex with axial wing-tip blowing off and on.

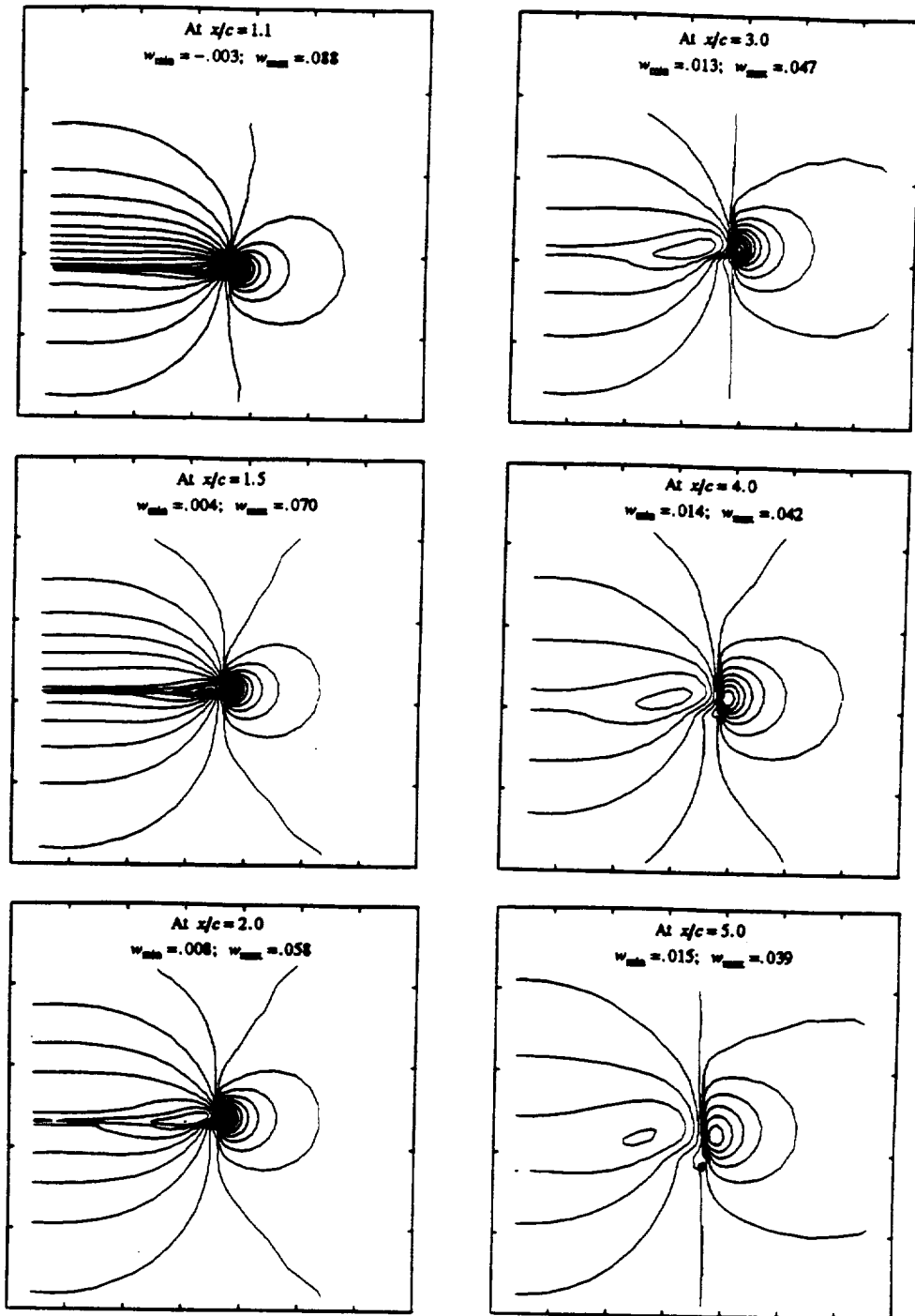


Figure 5.19: Downwash distribution at various axial stations downstream of the trailing edge for the case of  $\alpha = 8^\circ$ ,  $M_\infty = 0.17$ ,  $Re = 2.0 \times 10^6$  and with blowing off.

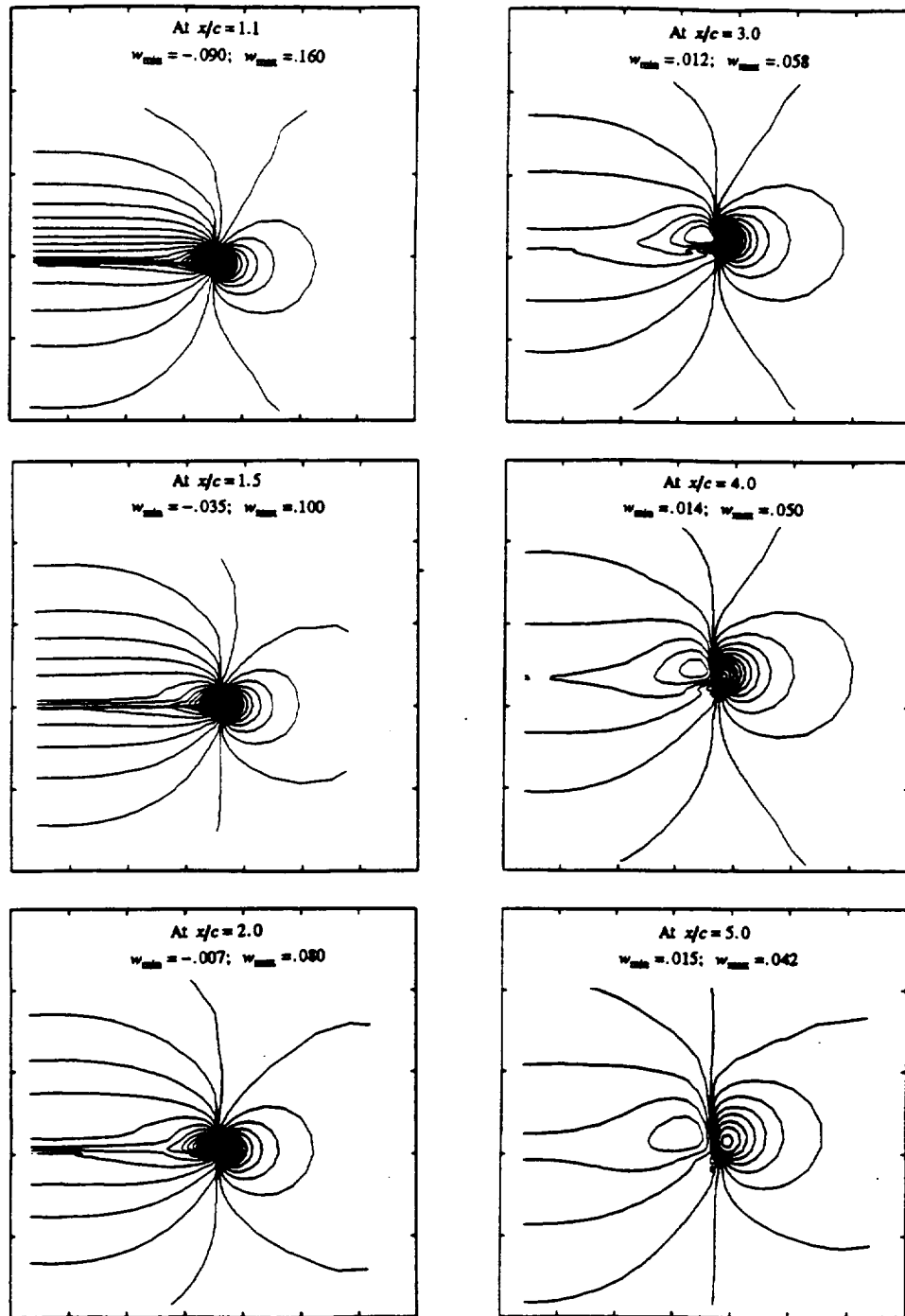


Figure 5.20: Downwash distribution at various axial stations downstream of the trailing edge for the case of  $\alpha = 8^\circ$ ,  $M_\infty = 0.17$ ,  $Re = 2.0 \times 10^6$  and with axial wing-tip blowing on ( $C_\mu = 0.0047$ ).

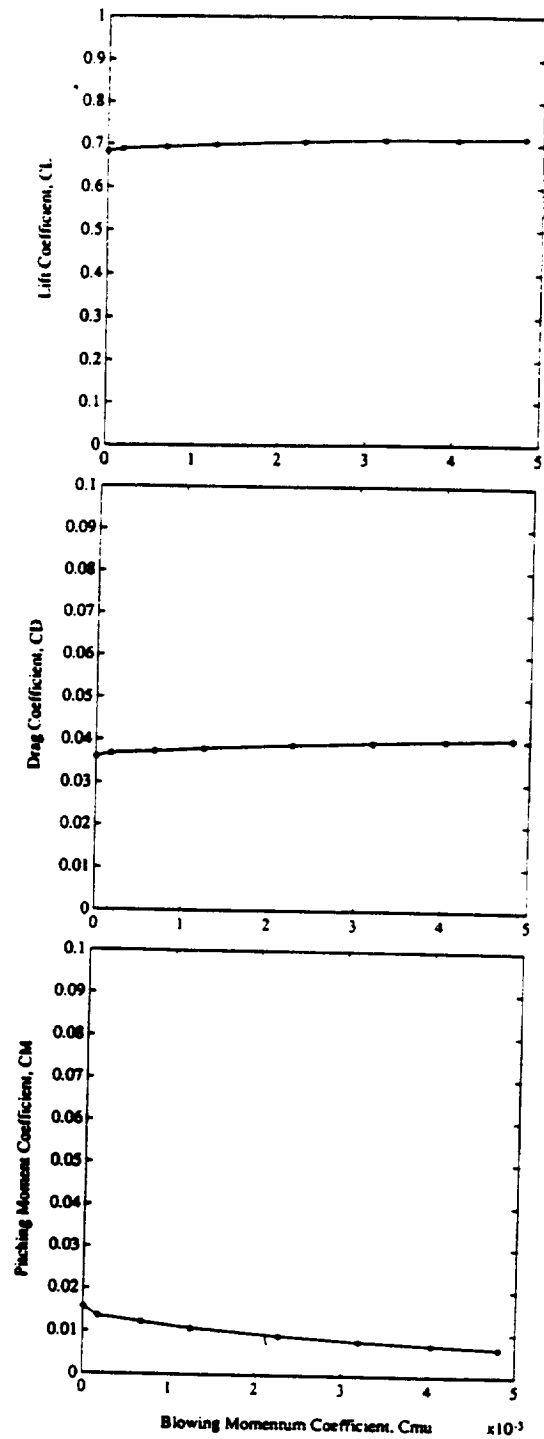
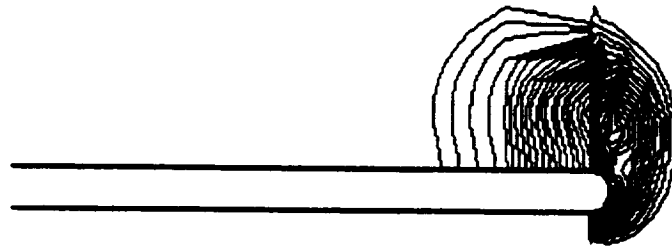
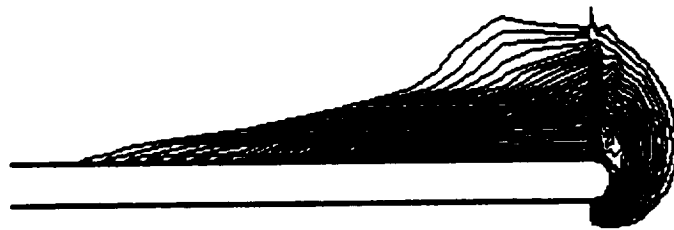


Figure 5.21: Variations of the coefficients of lift, drag and pitching moment (about the quarter-chord) with blowing momentum coefficient for the case of  $\alpha = 8^\circ$ ,  $M_\infty = 0.17$  and  $Re = 2.0 \times 10^6$ .



(a) Blowing off.



(b) Blowing on ( $C_{\mu} = 0.0047$ ).

Figure 5.22: Pressure contours at  $x/c = 0.95$  near the wing-tip region for cases with axial wing-tip blowing off and on.

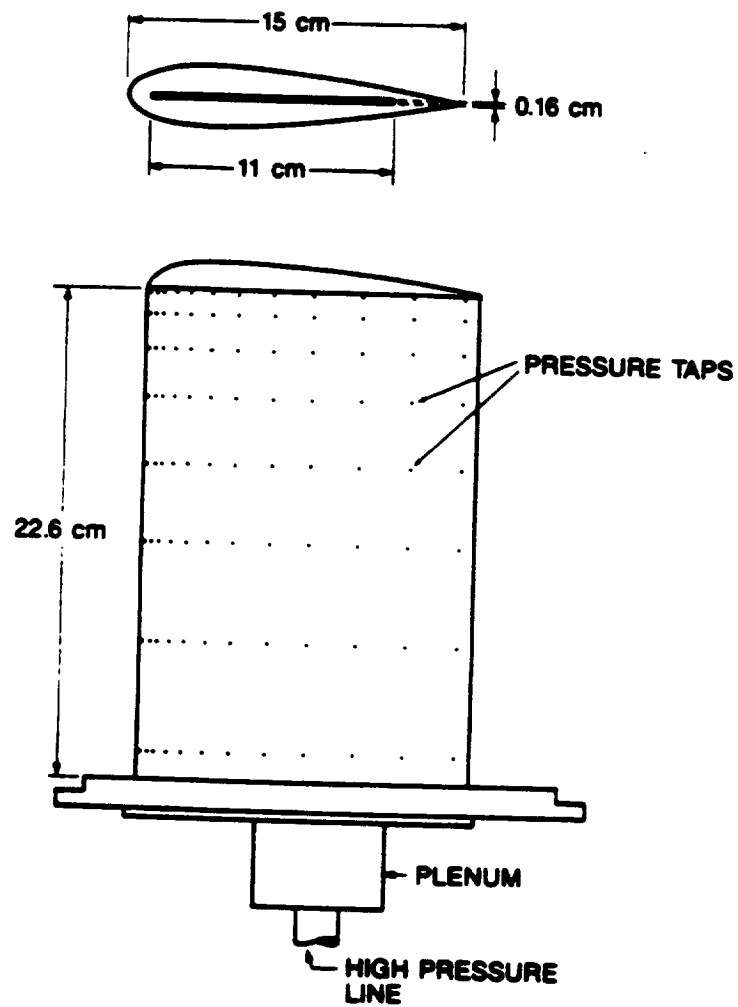
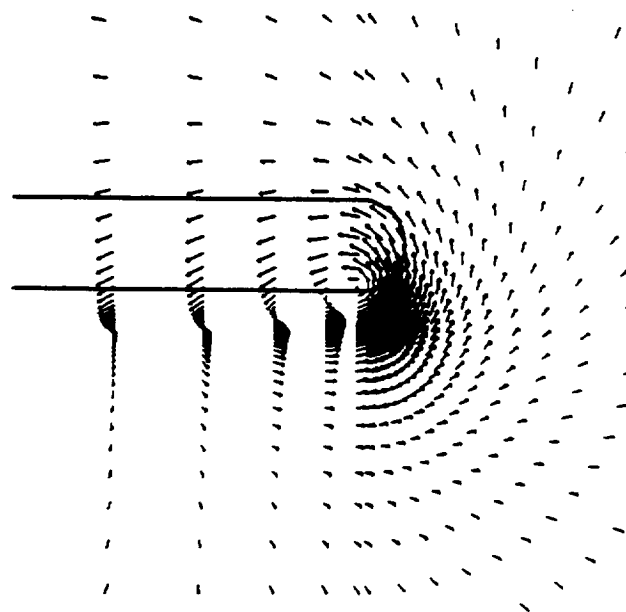
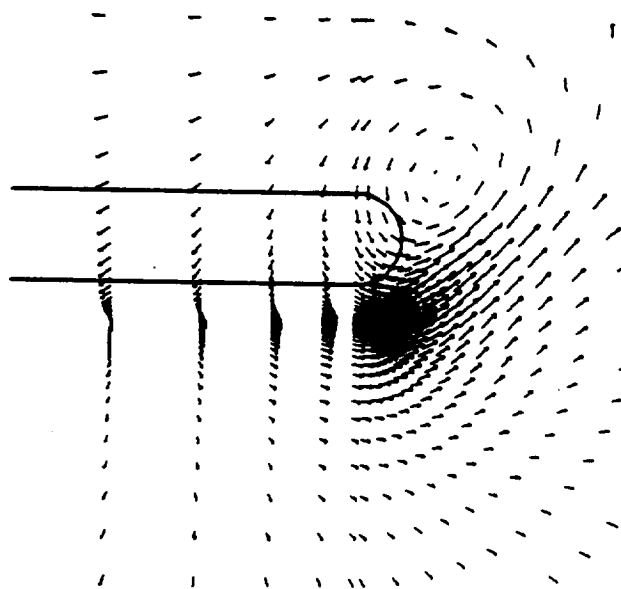


Figure 5.23: Wind-tunnel model used in the experimental studies with spanwise wing-tip blowing (taken from Tavella et al [1988]).



(a) Blowing off.



(b) Blowing on ( $C_{\mu} = 0.0169$ ).

Figure 5.24: Close-up views of the velocity vectors at  $x/c = 1.1$  for the case of  $\alpha = 8^\circ$  with spanwise wing-tip blowing turned off and on.

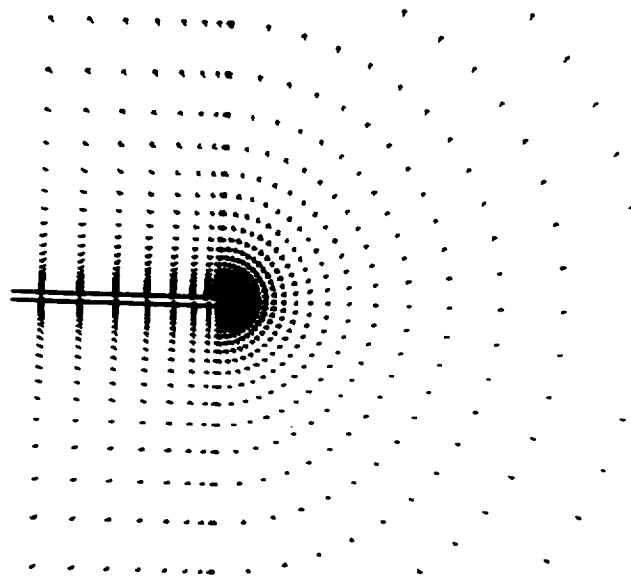
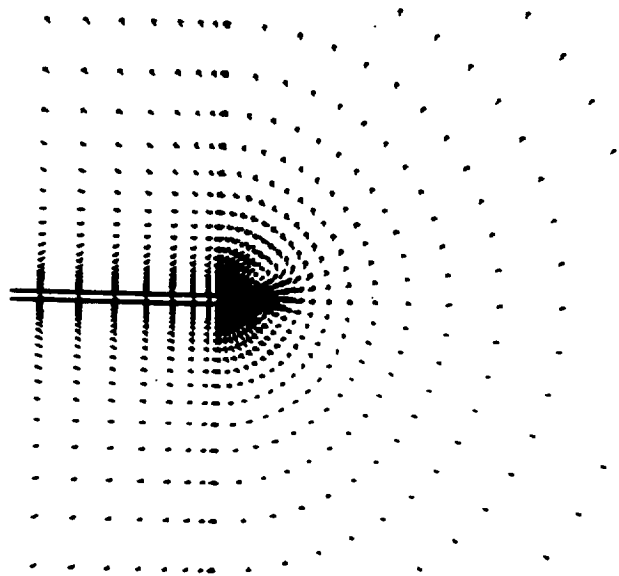
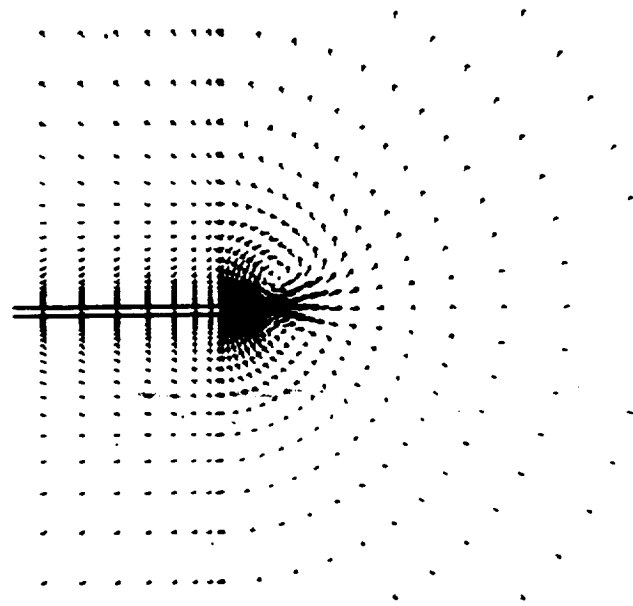
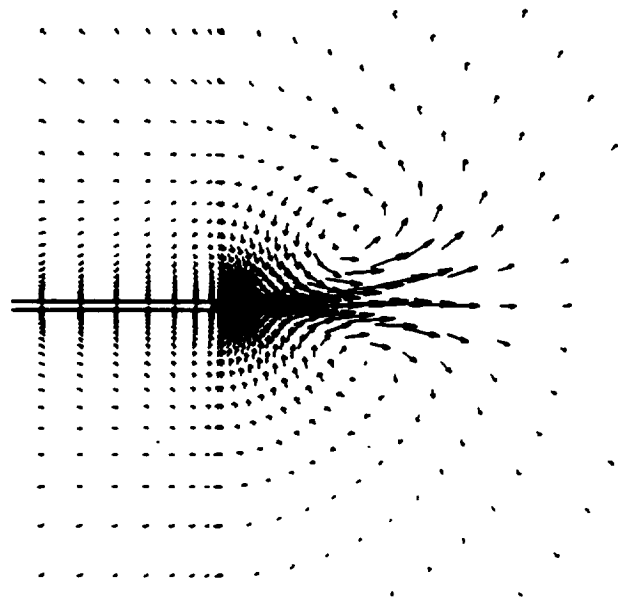
(a)  $C_\mu = 0.0000$ .(b)  $C_\mu = 0.0168$ .

Figure 5.25: Velocity vectors at  $x/c = 0.9$  for the case of  $\alpha = 2^\circ$  with increasing spanwise wing-tip blowing intensity.

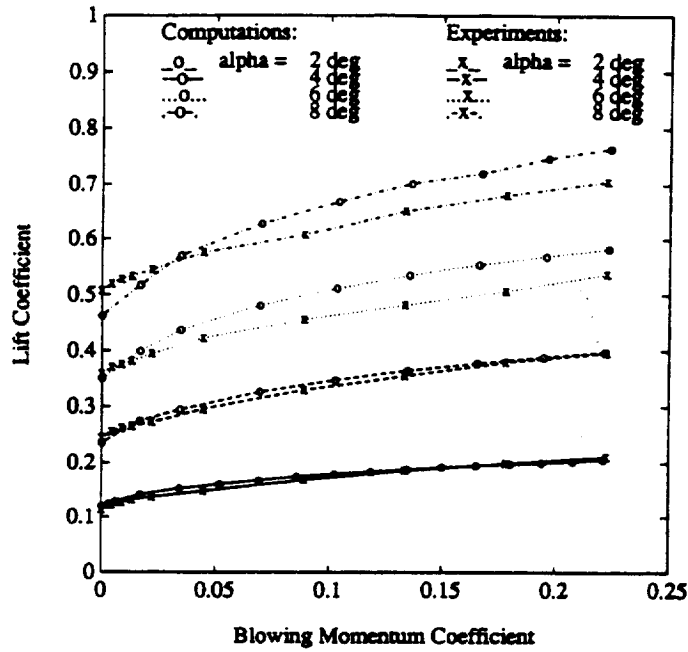


(c)  $C_\mu = 0.0342$ .

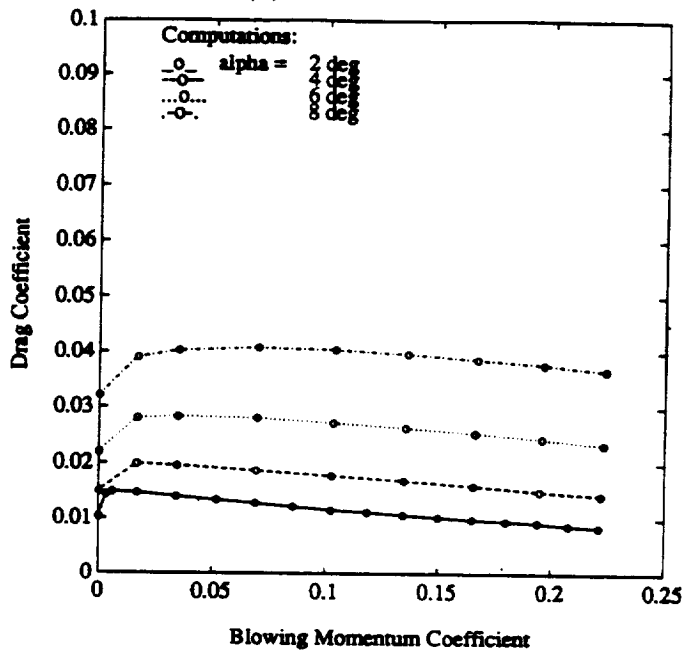


(d)  $C_\mu = 0.2076$ .

Figure 5.25: Concluded.

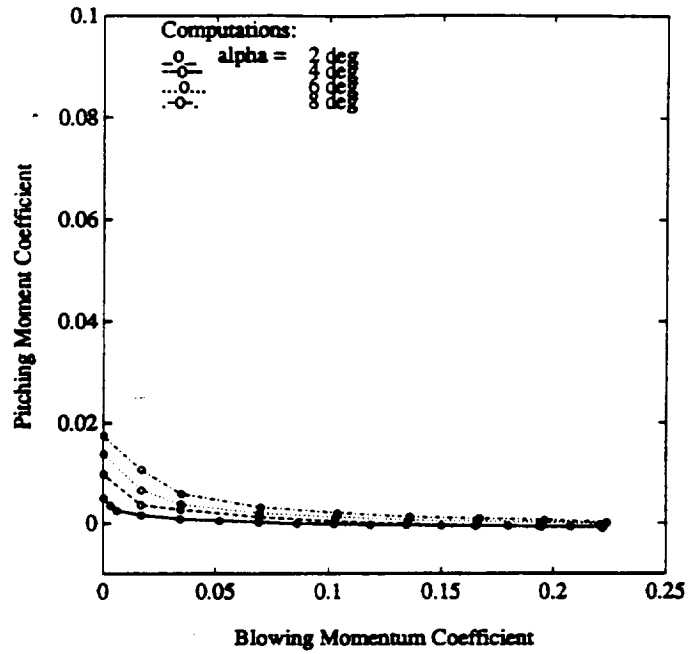


(a) Lift coefficient.

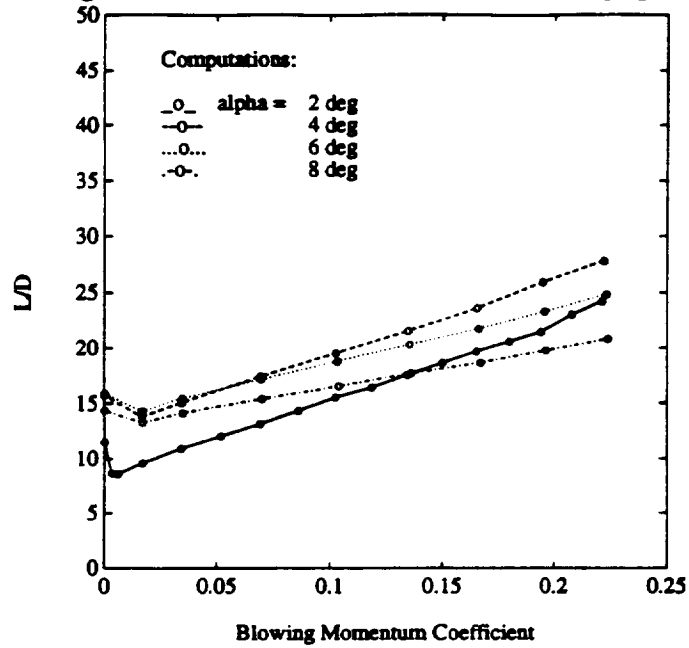


(b) Drag coefficient.

Figure 5.26: Variations of the coefficients of lift, drag, pitching moment (about the wing quarter-chord) and  $L/D$  with blowing momentum coefficient for  $\alpha = 2^\circ, 4^\circ, 6^\circ$  and  $8^\circ$ .



(c) Pitching moment coefficient (about the wing quarter-chord).



(d) *L/D*.

Figure 5.26: Concluded.

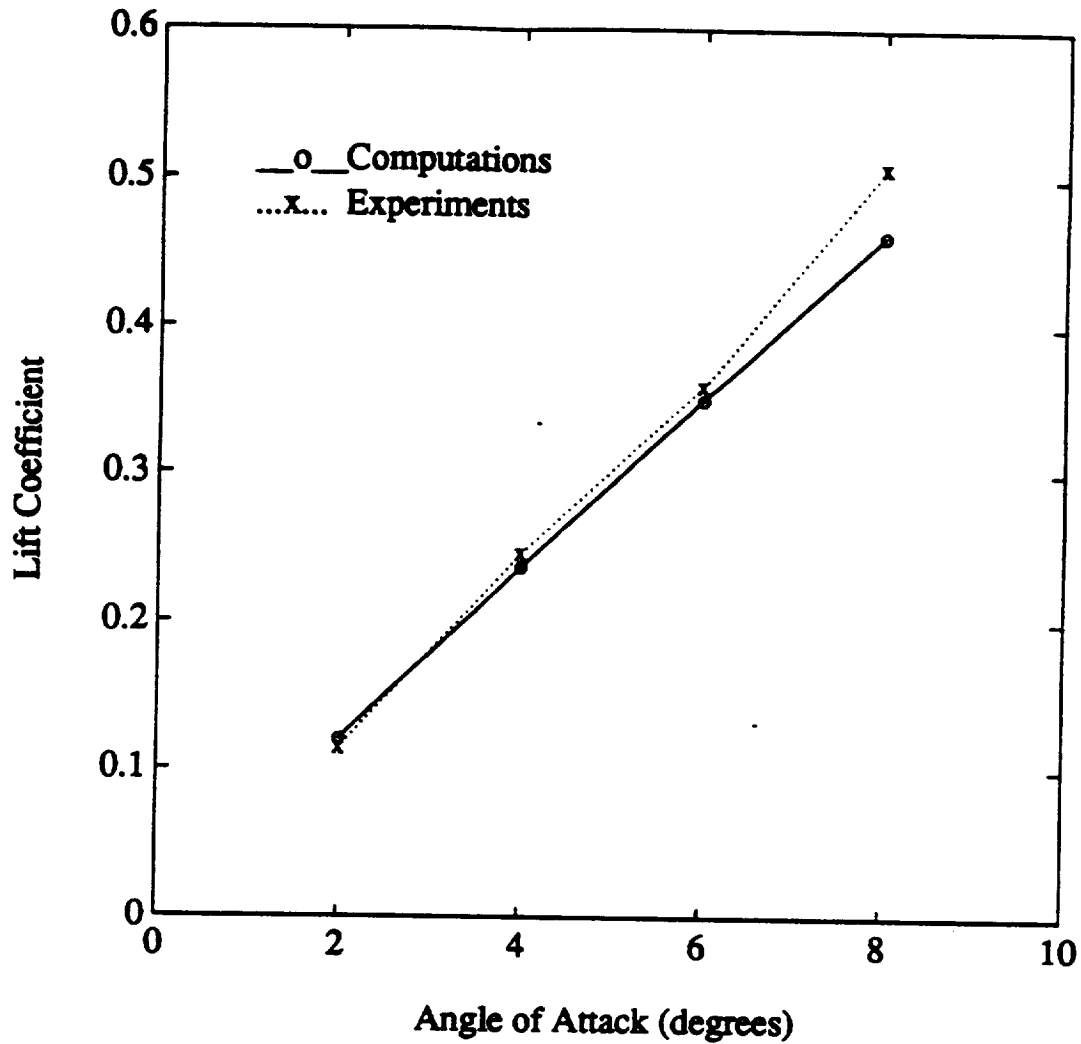


Figure 5.27: Variation of the coefficient of lift with angle-of-attack without spanwise wing-tip blowing.

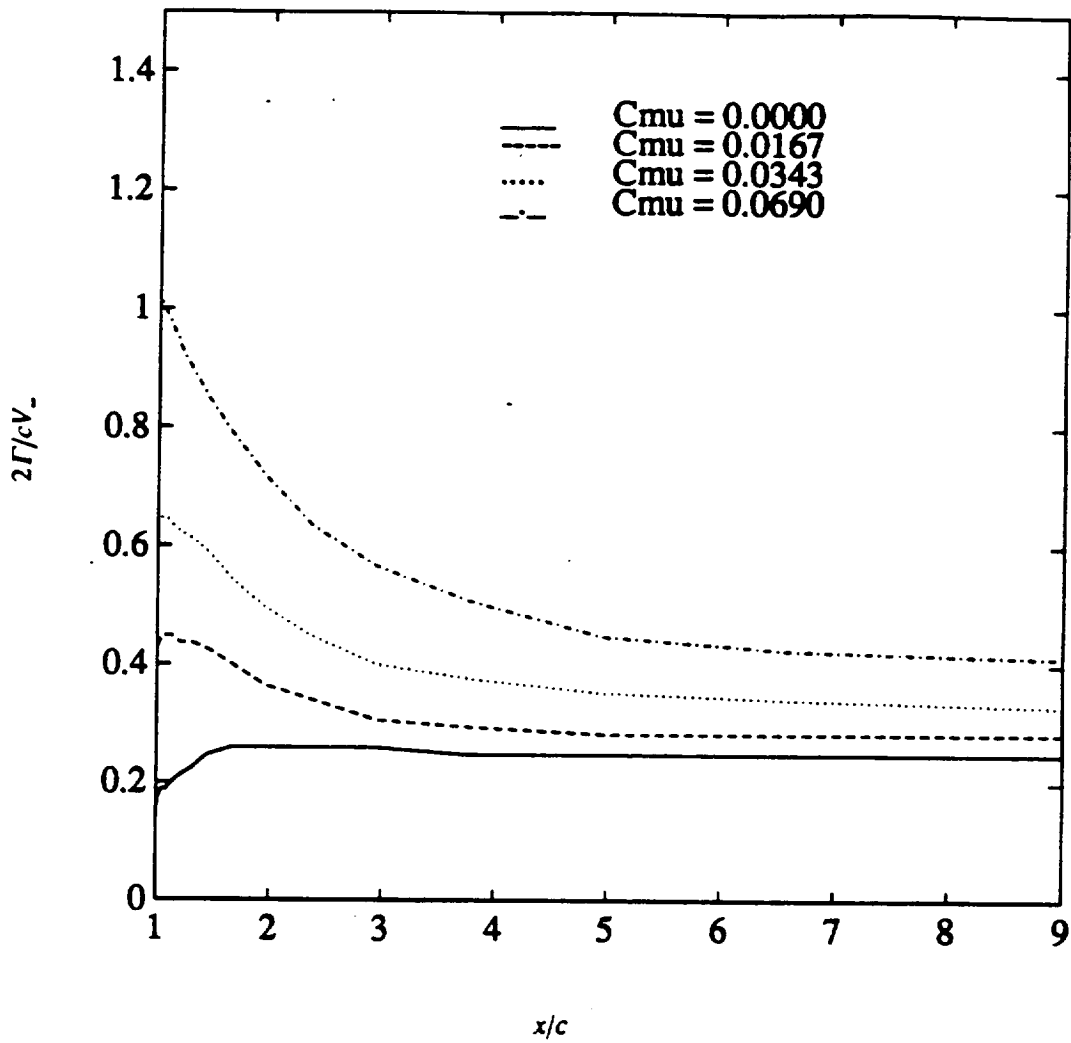


Figure 5.28: Variation of the streamwise distribution of the normalized total circulation with blowing momentum coefficient for the case of  $\alpha = 4^\circ$ .

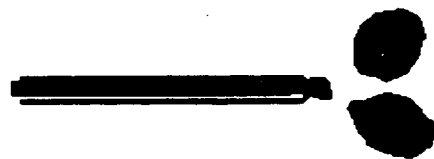
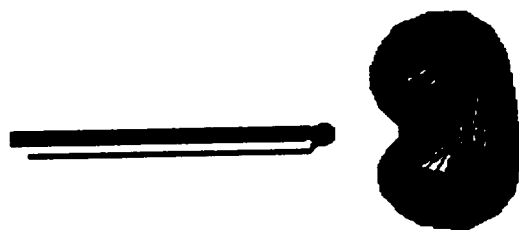
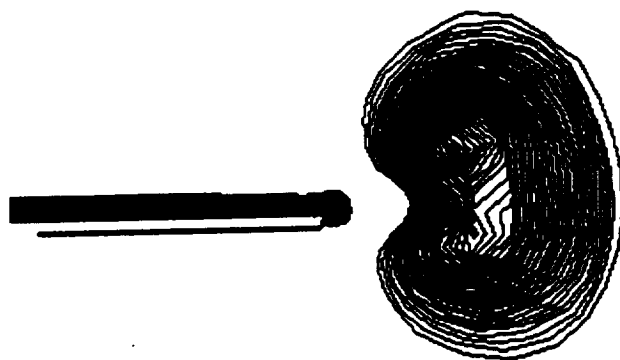
(a)  $x/c = 0.95$ .(b)  $x/c = 1.00$ .

Figure 5.29: Stagnation pressure contours showing the streamwise development of the primary and secondary vortices for the case  $\alpha = 2^\circ$  and  $C_\mu = 0.2067$ .

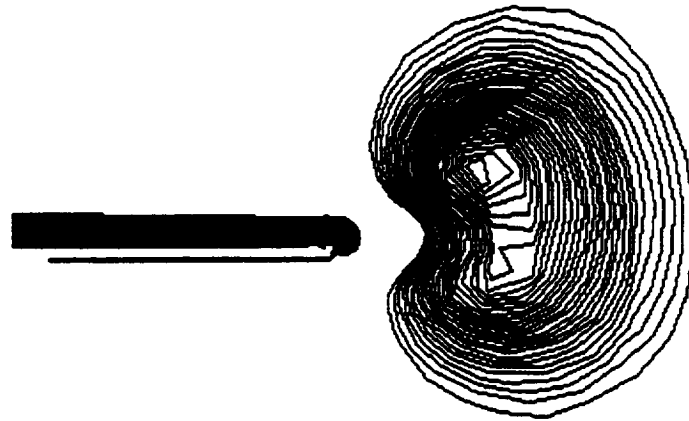


(c)  $x/c = 2.00$ .

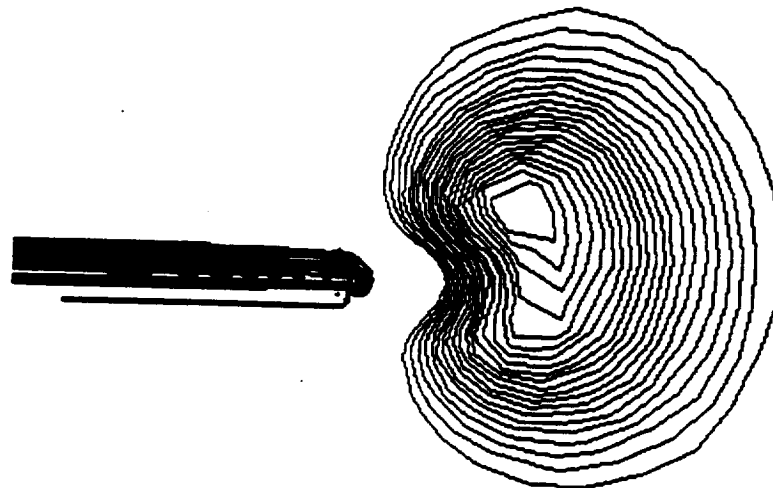


(d)  $x/c = 3.00$ .

Figure 5.29: Continued.

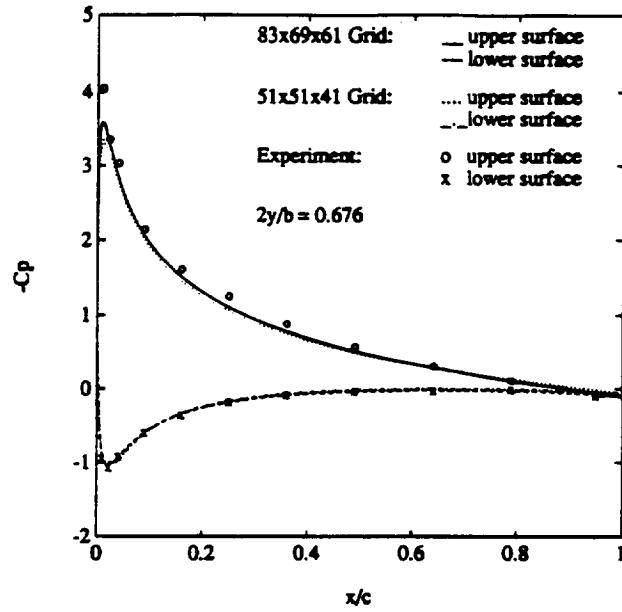


(e)  $x/c = 4.00$ .

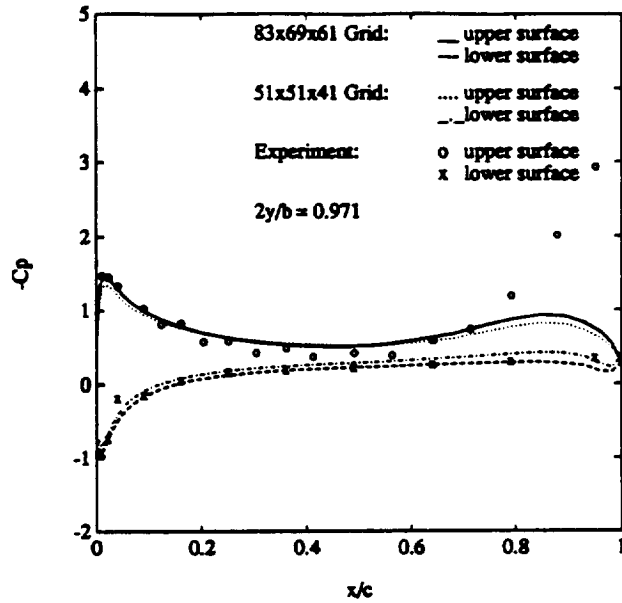


(f)  $x/c = 5.00$ .

Figure 5.29: Concluded.



(a) At  $2y/b = 0.676$ .



(b) At  $2y/b = 0.971$ .

Figure 5.30: Comparison of the computational results using coarse and fine grids with the experimental data for the case of  $\alpha = 12^\circ$ .



# Chapter 6

## Conclusions and Recommendations

### 6.1 Conclusions

Numerical simulations of the complex flowfield of the trailing vortex of a wing with axial and spanwise wing-tip blowing have been successfully performed using Computational Fluid Dynamics techniques. The unsteady, three-dimensional, thin-layer Navier-Stokes equations are solved using a time-accurate, implicit, finite difference numerical algorithm. The actuator plane concept and the solution blanking feature of the chimera scheme have been successfully incorporated to simulate wing-tip blowing. Computational results are generally in good agreement with experimental data. The main conclusions of the present study are summarized as follows:

- (1) The axial wing-tip blowing has the effect of modifying the flowfield behavior immediately downstream of the wing.

However, its effect diminishes farther downstream. Overall, the axial wing-tip blowing strengthens the circulation strength of the trailing vortex marginally due to the marginal increase in the wing lift.

- (2) At moderately low blowing intensity, the spanwise wing-tip blowing has the effect of displacing the tip vortex outboard and upwards and results in the augmentation of lift.
- (3) At higher blowing intensity, a secondary vortex rotating in the opposite direction to the primary vortex is formed by the spanwise wing-tip blowing.
- (4) The circulation strength of the vortex system increases as a result of lift augmentation on the wing due to the spanwise wing-tip blowing.
- (5) Spanwise wing-tip blowing can be an effective means of control to effect a change of vortex position on one wing-tip and thereby produce a rolling moment through asymmetric wing lift.

## 6.2 Recommendations

Some recommendations for future work are as follows:

- (1) Improve the solution accuracy by increasing the grid point density in the regions of the leading edge, trailing edge, tip of the wing and

the trajectory of the trailing vortex. Study the effect of grid refinement on solution accuracy.

- (2) Extend the outflow boundary to several wing spans to capture the far-field behavior of the trailing vortex.
- (3) Perform full Navier-Stokes simulations to investigate the limitations of the thin-layer approximation for the trailing vortex flow.
- (4) Model the complex flowfield of the trailing vortex with wing-tip blowing with better turbulence models.
- (5) Simulate the complex flowfield of the trailing vortex with wing-tip blowing for a rotorcraft by incorporating the rotating motion of the rotor blades. Fine grid points must be clustered to capture the trailing vortices from the rotor blades as they spiral downwards due to the rotor downwash.



# Bibliography

- Anderson, D.A., Tannehill, J.C., and Pletcher, R.H., *Computational Fluid Mechanics and Heat Transfer*, Hemisphere Publishing Corp., New York, 1984.
- Ayers, R.F. and Wilde, M.R., "An Experimental Investigation of the Aerodynamic Characteristics of a Low Aspect Ratio Swept Wing with Blowing in a Spanwise Direction from the Tips," The College of Aeronautics, Cranfield, UK, Note 57, 1956.
- Baldwin, B.S. and Lomax, H., "Thin Layer Approximation and Algebraic Model for Separated Turbulent Flows," AIAA Paper 78-0257, AIAA 16th Aerospace Sciences Meeting, Huntsville, Alabama, January 1978.
- Beam, R.M. and Warming, R.F., "An Implicit Finite-Difference Algorithm for Hyperbolic Systems in Conservation-Law Form," *Journal of Computational Physics*, Vol. 22, 1976, pp. 87-109.
- Beam, R.M. and Warming, R.F., "An Implicit Factored Scheme for the Compressible Navier-Stokes Equations," *AIAA Journal*, Vol. 16, No. 4, April 1978, pp. 393-402.
- Benek, J.A., Buning, P.G., and Steger, J.L., "A 3-D Chimera Grid Embedding Technique," AIAA Paper 85-1523, 1985.
- Betz, A., "Behavior of Vortex Systems," NACA TM-713, 1932.

- Childs, R.E., "Lift Augmentation via Spanwise Tip Blowing: A Numerical Study," AIAA Paper 86-0474, AIAA 24th Aerospace Sciences Meeting, Reno, Nevada, January 1986.
- Chow, J.S., Zilliac, G.G., and Bradshaw, P., "Measurements in the Near-Field of a Turbulent Wingtip Vortex," AIAA Paper 93-0551, AIAA 31st Aerospace Sciences Meeting and Exhibit, Reno, Nevada, January 1993.
- Corsiglia, V.R., Jacobsen, R.A., and Chigier, N.A., "An Experimental Investigation of Trailing Vortices Behind a Wing with a Vortex Dissipator," *Aircraft Wake Turbulence and its Detection*, Olsen, J.H., Goldberg, A., and Rogers, M. (Eds.), Plenum Press, New York, 1971, pp. 229-242.
- Craig, K.J., "Computational Study of Blowing on Delta Wings at High Alpha," *Journal of Aircraft*, Vol. 30, No. 6, November - December 1993, pp. 833-839.
- Dacles-Mariani, J., Rogers, S., Kwak, D., Zilliac, G.G., and Chow, J.S., "A Computational Study of Wingtip Vortex Flowfield," AIAA Paper 93-3010, AIAA 24th Fluid Dynamics Conference, Orlando, Florida, July 1993.
- Dunham, R.E., Jr, "Unsuccessful Concepts for Aircraft Wake Vortex Minimization," *Wake Vortex Minimization*, NASA SP-409, 1976, pp. 221-249.
- Fejtek, I. and Roberts, L., "Navier-Stokes Computation of Wing/Rotor Interaction for a Tilt Rotor in Hover," *AIAA Journal*, Vol. 30, No. 11, November 1992, pp. 2595-2603.
- Font, G.I. and Tavella, D.A., "High Alpha Aerodynamic Control by Tangential Fuselage Blowing," AIAA 91-0620, 29th Aerospace Sciences Meeting, Reno, Nevada, January 1991.
- Fujii, K. and Obayashi, S., "Practical Applications of New LU-ADI Scheme for the Three-Dimensional Navier-Stokes Computation of Transonic Viscous

- Flows," AIAA Paper 86-0513, AIAA 24th Aerospace Sciences Meeting, Reno, Nevada, January 1986.
- Fujii, K. and Obayashi, S., "Navier-Stokes Simulation of Transonic Flow Over Wing-Fuselage Combinations," AIAA Paper 86-1831, AIAA 4th Applied Aerodynamics Conference, San Diego, California, 1986.
- Gessow, A., "Introduction," Wake Vortex Minimization, NASA SP-409, 1976, pp. 1-7.
- Hackett, J.E. and Evans, M.R., "Vortex Wakes Behind High-Lift Wings," Journal of Aircraft, Vol. 8, No. 5, May 1971, pp. 334-340.
- Hallock, J.N. and Eberle, W.R., "Aircraft Wake Vortices: A State-of-the-Art Review of the United States R&D Program," FAA Report FAA-RD-77-23, February 1977.
- Hallock, J.N. (Ed.), "Proceedings of the Aircraft Wake Vortex Conference," DOT-VNTSC-FAA-92-7, U.S. Department of Transportation, John A. Volpe National Transportation Systems Center, Cambridge, MA, June 1992.
- Higuchi, H., Quadrell, J.C., and Farell, C., "Vortex Roll-Up for an Elliptically-Loaded Wing at Moderately Low Reynolds Numbers," AIAA Paper 86-0562, AIAA 24th Aerospace Sciences Meeting, Reno, Nevada, January 1986.
- Holst, T.L., "Numerical Computation of Transonic Flow Governed by the Full-Potential Equation," NASA TM-84310, 1983.
- Kuethe, A.M. and Chow, C.-Y., *Foundations of Aerodynamics: Bases of Aerodynamic Design*, 4th Edition, John Wiley, New York, 1986.
- Lanchester, F.W., *Aerodynamics*, Constable and Co., London, 1907.
- Lee, C.S., Tavella, D.A., Wood, N.J., and Roberts, L., "Flow Structure and Scaling Laws in Lateral Wing-Tip Blowing," AIAA Journal, Vol. 27, No. 8, August 1989, pp. 1002-1007.

- Lombard, C., Bardina, J., Venkatapathy, E., and Olinger, J., "Multi-Dimensional Formulation of CSCM - An Upwind Flux Difference Eigenvector Split Method for the Compressible Navier-Stokes Equations," AIAA Paper 83-1895, AIAA 6th CFD Conference, Danvers, Massachusetts, 1983.
- Mansour, N.N., "Computation of the Tip Vortex Off a Low-Aspect-Ratio Wing," AIAA Journal, Vol. 23, No. 8, August 1985, pp. 1143-1149.
- Mason, W.H. and Marchman III, J.F., "Far-Field Structure of Aircraft Wake Turbulence," Journal of Aircraft, Vol. 10, No. 2, February 1973, pp. 86-92.
- McAlister, K.W. and Takahashi, R.K., "NACA 0015 Wing Pressure and Trailing Vortex Measurements," NASA TP-3151, November 1991.
- McCormick, B.W., Tangler, J.L., and Sherrieb, H.E., "Structure of Trailing Vortices," Journal of Aircraft, Vol. 5, No. 3, May-June 1968, pp. 260-267.
- Middlecoff, J.F. and Thomas, P.D., "Direct Control of the Grid Point Distribution in Meshes Generated by Elliptic Equations," AIAA Paper 79-1462, July 1979.
- Obayashi, S., Fujii, K., and Gavali, S., "Navier-Stokes Simulation of Wind-Tunnel Flow Using LU-ADI Factorization Algorithm," NASA TM-100042, February, 1988.
- Obayashi, S. and Kuwahara, K., "An Approximate LU Factorization Method for the Compressible Navier-Stokes Equations," Journal of Computational Physics, Vol. 63, 1986, pp. 157-167.
- Olsen, J.H., Goldberg, A., and Rogers, M. (Eds.), *Aircraft Wake Turbulence and Its Detection*, Proceedings of a Symposium on Aircraft Wake Turbulence held in Seattle, Washington, September 1-3, 1970, Plenum Press, New York, 1971.
- Peyret, R. and Viviand, H., "Computation of Viscous Compressible Flows Based on the Navier-Stokes Equations," AGARD-AG-212, 1975.

- Phillips, W.R.C., "The Turbulent Trailing Vortex During Roll-Up," *Journal of Fluid Mechanics*, Vol. 105, 1981, pp. 451-467.
- Pulliam, T.H., "Euler and Thin Layer Navier-Stokes Codes: ARC2D, ARC3D," Notes for Computational Fluid Dynamics User's Workshop, The University of Tennessee Space Institute, Tullahoma, Tennessee, March 1984.
- Pulliam, T.H. and Chaussee, D.S., "A Diagonal Form of an Implicit Approximate-Factorization Algorithm," *Journal of Computational Physics*, Vol. 39, 1981, pp. 347-363.
- Pulliam, T.H. and Steger, J.L., "Implicit Finite-Difference Simulations of Three-Dimensional Compressible Flow," *AIAA Journal*, Vol. 18, No. 2, February 1980, pp. 159-167.
- Pulliam, T.H. and Steger, J.L., "Recent Improvements in Efficiency, Accuracy, and Convergence for Implicit Approximate Factorization Algorithms," AIAA Paper 85-0360, AIAA 23rd Aerospace Sciences Meeting, Reno, Nevada, 1985.
- Roberts, L., "Persistence and Decay of Wake Vorticity," *Flight/Ground Testing Facilities Correlation*, AGARD CP-187, 1975.
- Roberts, L., "On the Structure of the Turbulent Vortex," *Aerodynamics of Vortical Type Flows in Three Dimensions*, AGARD CP-342, 1984.
- Roberts, L., "A Theory for Turbulent Curved Wall Jets," AIAA Paper 87-0004, AIAA 25th Aerospace Sciences Meeting, Reno, Nevada, 1987.
- Schmitz, F.H. and Yu, Y.H., "Helicopter Impulsive Noise: Theoretical and Experimental Status," *International Symposium on Recent Advances in Aerodynamics and Aeroacoustics*, Stanford University, Stanford, California, August 1983, Vol. 2, pp. 150-243.
- Snedeker, R.S., "Effect of Air Injection on the Torque Produced by a Trailing Vortex," *Journal of Aircraft*, Vol. 9, No. 9, September 1972, pp. 682-684.

- Sorenson, R.L. and Steger, J.L., "Numerical Generation of Two-Dimensional Grids by the Use of Poisson Equations with Grid Control at Boundaries," Proceedings of the Numerical Grid Generation Techniques Workshop, NASA Langley Research Center, Hampton, Virginia, NASA CP-2166, 1980, pp. 449-461.
- Spivey, R.F., "Blade Tip Aerodynamics - Profile and Planform Effects," 24th Annual National Forum Proceedings of the American Helicopter Society, Washington D.C., 1968.
- Spreiter, J.R. and Sacks, A.H., "The Rolling Up of the Trailing Vortex Sheet and Its Effect on the Downwash Behind Wings," Journal of the Aeronautical Sciences, Vol. 18, No. 1, 1951, pp. 21-32.
- Srinivasan, G.R., Baeder, J.D., Obayashi, S., and McCroskey, W.J., "Flowfield of a Lifting Hovering Rotor - A Navier-Stokes Simulation," AIAA Journal, Vol. 30, No. 10, October 1992, pp. 2371-2378.
- Srinivasan, G.R., McCroskey, W.J., Baeder, J.D., and Edwards, T.A., "Numerical Simulation of Tip Vortices of Wings in Subsonic and Transonic Flows," AIAA Journal, Vol. 26, No. 10, October 1988, pp. 1153-1162.
- Steger, J.L., "Implicit Finite Difference Simulation of Flow About Arbitrary Geometries with Application to Airfoils," AIAA Paper 77-665, AIAA 10th Fluid & Plasmadynamics Conference, Albuquerque, New Mexico, 1977.
- Steger, J.L. and Sorenson, R.L., "Automatic Mesh-Point Clustering Near a Boundary in Grid Generation with Elliptic Partial Differential Equations," Journal of Computational Physics, Vol. 33, December 1979, pp. 405-410.
- Steger, J.L. and Warming, R.F., "Flux Vector Splitting of the Inviscid Gasdynamic Equations with Application to Finite-Difference Methods," Journal of Computational Physics, Vol. 40, 1981, pp. 263-293.

- Stepniewski, W.Z. and Keys, C.N., *Rotary-Wing Aerodynamics*, Dover Publications, Inc., New York, 1984.
- Strawn, R.C., "Wing Tip Vortex Calculations with an Unstructured Adaptive-Grid Euler Solver," presented at the 47th Annual Forum of the American Helicopter Society, Phoenix, Arizona, May 1991.
- Tavella, D.A., Schiff, L.B., and Cummings, R.M., "Pneumatic Vortical Control at High Angles of Attack," AIAA Paper 90-0098, 28th Aerospace Sciences Meeting, Reno, Nevada, 1990.
- Tavella, D.A., Wood, N.J., and Harrits, P., "Influence of Tip Blowing on Rectangular Wings," AIAA Paper 85-5001, AIAA 3rd Applied Aerodynamics Conference", Colorado Springs, Colorado, October 1985.
- Tavella, D.A., Wood, N.J., Lee, C.S., and Roberts, L., "Lift Modulation with Lateral Wing-Tip Blowing," *Journal of Aircraft*, Vol. 25, No. 4, April 1988, pp. 311-316.
- Thompson, J.F., Thames, F.C., and Mastin, C.W., "Automatic Numerical Generation of Body-Fitted Curvilinear Coordinate System for Field Containing Any Number of Arbitrary Two-Dimensional Bodies," *Journal of Computational Physics*, Vol. 15, 1974, pp. 299-319.
- Thompson, J.F., Thames, F.C., and Mastin, C.W., "TOMCAT - A Code for Numerical Generation of Boundary-Fitted Curvilinear Coordinate Systems on Fields Containing Any Number of Arbitrary Two-Dimensional Bodies," *Journal of Computational Physics*, Vol. 24, 1977, pp. 274-302.
- Thompson, J.F., Thames, F.C., and Mastin, C.W., "Boundary-Fitted Coordinate Systems for Solution of Partial Differential Equations on Fields Containing Any Number of Arbitrary Two-Dimensional Bodies," NASA CR-2729, 1977.

- Thompson, J., Thames, F., Mastin, C., and Shanks, S., "Use of Numerically Generated Body-Fitted Coordinate Systems for Solutions of the Navier-Stokes Equations," AIAA 2nd CFD Conference, Connecticut, 1975.
- Trevena, D.H., *Cavitation and Tension in Liquids*, IOP Publishing Ltd, Bristol, England, 1987.
- Tung, C., Pucci, S.L., Caradonna, F.X., and Morse, H.A., "The Structure of Trailing Vortices Generated by Model Rotor Blades," *Vertica*, Vol. 7, No. 1, 1983, pp. 33-43.
- Vinokur, M., "Conservation Equations of Gasdynamics in Curvilinear Coordinate Systems," *Journal of Computational Physics*, Vol. 14, 1974, pp. 105-125.
- Vinokur, M., "On One-Dimensional Stretching Functions for Finite-Difference Calculations," *Journal of Computational Physics*, Vol. 50, 1983, pp. 215-234.
- Viviand, H., "Formes Conservatives des Équations de la Dynamique des Gaz," *La Recherche Aérospatiale*, No. 1, 1974, pp. 65-68.
- Westwater, F.L., "Rolling Up of the Surface of Discontinuity Behind an Airfoil of Finite Span," *British A.R.C., R. & M.* 1692, 1935.
- White, R.P., Jr., "An Investigation of the Vibratory and Acoustic Benefits Obtainable by the Elimination of the Blade Tip Vortex," *Journal of the American Helicopter Society*, Vol. 18, No. 4, October 1973, pp. 35-44.
- Wong, T.-C. and Kandil, O.A., "Computation of Vortex Wake Flows and Control of Their Effects on Trailing Wings," AIAA Paper 92-4429-CP, 1992.
- Wu, J.M., Vakili, A.D., and Gilliam, F.T., "Aerodynamic Interactions of Wingtip Flow with Discrete Wingtip Jets," AIAA Paper 84-2206, AIAA 2nd Applied Aerodynamics Conference, Seattle, Washington, 1984.

- Yeh, D., Tavella, D.A., Roberts, L., and Fujii, K., "Numerical Study of the Effect of Tangential Leading-Edge Blowing on Delta Wing Vortical Flow," AIAA 89-0341, 27th Aerospace Sciences Meeting, Reno, Nevada, 1989.
- Yip, L.P. and Shubert, G.L., "Pressure Distributions on a 1-By-3 Meter Semispan Wing at Sweep Angles from  $0^\circ$  -  $40^\circ$  in Subsonic Flow," NASA TN D-8307, December 1976.

